

AD-A047 427

CIVIL ENGINEERING LAB (NAVY) PORT HUENEME CALIF
MIGHTY EPIC PRE-TEST ANALYSIS. (U)
MAR 77 J CRAWFORD, R MURTHA, J ROLLINS
CEL-TM-51-77-5

F/G 18/3

UNCLASSIFIED

NL

1 OF 2
AD
A047427



TM no. ¹⁴CEL-
TM-51-77-5

ADA 047427



TECHNICAL MEMORANDUM

⁶ title: ⁹ Technical
MIGHTY EPIC PRE-TEST ANALYSIS,

¹⁰ author: J. CRAWFORD,
R. MURTHA,
J. ROLLINS,
R. THOMPSON,
R. ODELLO

date: MAR 77

¹¹ sponsor: DEFENSE NUCLEAR AGENCY
WASHINGTON, DC

program nos: ¹⁶ F008-08-02-108

¹⁷ YF0080802

AD No. _____
DDC FILE COPY



CIVIL ENGINEERING

NAVAL CONSTRUCTION BATTALION
Port Hueneme, California 93043

DIS
A1

391 111

TABLE OF CONTENTS

	Page
ABSTRACT	1
OBJECTIVE AND SCOPE.	1
PROBLEM DESCRIPTION.	2
NONSAP Parameters	2
General Mesh Description.	3
Materials	3
Geostatic Effects	3
Forcing Function.	4
FREE FIELD VALIDATION AND DETERMINATION OF VARIOUS MESH PARAMETERS	4
Free Field Validation	4
Compatibility of 4-Node and Higher Quadrilateral Elements	5
Technique Employed for Removal of Reflection Waves.	5
Computation of Residual Response.	6
Use of Velocity as Forcing Function	6
ANALYSIS OF A CYLINDRICAL CAVITY WITHIN THE FREE FIELD	6
RESULTS OF ANALYSES OF MIGHTY EPIC STRUCTURES.	8
Homogeneous Sphere.	8
Composite Built-Up Liner.	9
Composite Integral Liner.	10
SUMMARY.	11
ACKNOWLEDGEMENTS	11
APPENDICES	49
A. Development of Material Parameters.	49
B. Element and Step Size Selection	62
C. Study of Compatibility of 4-Node and Higher Order Quadrilateral Elements	72
D. Restart Using Progressively Larger Δt	79
E. Use of Velocity as a Forcing Function	82

475	476	477	478
BY	DISTRIBUTION AVAILABILITY CODES	800L	AVAIL. STATE SPECIAL

TABLE OF CONTENTS (Cont.)

	Page
REFERENCES	87
LIST OF SYMBOLS.	89
LIST OF TABLES	92
LIST OF FIGURES.	93

ABSTRACT

Analytical response predictions (pre-shot) are made for three structures that are to be evaluated during the Mighty Epic tests. Also included in the report is a prediction of the response for the free field and for the free field containing a cavity, as well as a study of the effects that various idealization parameters have on the predicted results.

OBJECTIVE AND SCOPE

The objective of this study is to analytically predict (pre-shot) the response of three structures that are in place at the Mighty Epic test site. These structures, shown in Figures 1 and 2, consist of:

- 1) Homogeneous sphere,
- 2) Composite built-up liner, and
- 3) Composite integral liner.

These three structures are situated in a relatively weak rock (tuff) at the 0.5-Kbar range. Included in the study is a prediction of the response for the free field (i.e., tuff) and for the tuff containing a six-foot diameter cylindrical cavity. Also reported are the effects that the various parameters associated with the predictions have on the results.

The scope of the analyses is predicated on usage of NONSAP¹ computer code in its "as is" state. NONSAP is a finite element computer program designed primarily for the nonlinear analysis of three-dimensional structures subjected to either static or dynamic forces applied either separately or in combination. The program offers a variety of material models, two implicit time integration schemes (i.e., Wilson's θ or Newmark's β method), two finite deformation formulations (based on either an Eulerian or Lagrangian reference system), and several element types (including the truss, beam, 4-8 node isoparametric quadrilateral, 8-21 node isoparametric hexahedron, and several types of joint and boundary elements). An "in-core" version of NONSAP, operated on a CDC 7600, is used to develop the results presented in this report.

This report was prepared for use as an internal working document. Therefore, its distribution is limited, and disclosure of all or part of its contents outside the Government must have prior approval of the Civil Engineering Laboratory or the sponsor of the work reported.

PROBLEM DESCRIPTION

NONSAP Parameters

NONSAP is particularly designed to solve nonlinear problems. The basic algorithm uses an incremental tangent approximation for the nonlinear stiffness coupled with equilibrium iterations at the end of a step to correct for the errors which arise as a consequence of the tangent approximation. For the problems discussed in this report, the stiffness matrix is inverted at every step while equilibrium iteration is used only for problems where large deformations are included. The large deformation formulation is based on a Lagrangian reference system which is felt to be most compatible with the material data provided. However, the lack of large deformation-oriented material data debilitates the employment of this formulation. The time integration is accomplished using Wilson's θ method.

For the problems in this report, 16 steps are used in application of nonlinear static runs while 44 steps with a 0.4-msec time step are used for dynamic runs (providing 17.6 msec of response). Typical CDC 7600 central processing times and costs are:

- o For the nonlinear static cases with equilibrium iteration, 210 seconds and \$80.
- o For the linear static cases, 7 seconds and \$10.
- o For the nonlinear dynamic cases with equilibrium iteration, 470 seconds and \$160.
- o For the linear dynamic cases, 45 seconds and \$15.

The high cost of equilibrium iteration is caused by its inefficient implementation on the CDC 7600. Reprogramming this algorithm in accordance with the 7600 architecture would mitigate this problem.

The elements employed in all solutions are 4-8 node, isoparametric quadrilaterals. Integration orders from 2-4 may be specified; in general, orders of 3 are used for the computations in this report. Integration orders of 3 result in nine integration points being established within the element at the Gauss points. Separate stress histories and material properties are computed for each of these points.

Some additional relevant features of NONSAP are:

1. Its restart capability, whereby any solution may be stopped and restarted with different parameters. For example, the geostatic stress at the Mighty Epic site may be computed as a nonlinear statics problem; these results would be automatically stored and be available as initial boundary conditions for the dynamic NONSAP simulation of the Mighty Epic structures.

2. Birth and death of elements, whereby elements are assigned times of appearance and/or disappearance. This makes it possible to solve the Mighty Epic geostatic problem as an unlined cavity where prior to the

dynamic run, the structure and grout elements would be "born" into the structural system.

General Mesh Description

Five different structural problems are presented in this study:

1. Free field
2. Free field with cavity
3. Homogeneous sphere
4. Composite built-up liner
5. Composite integral liner

Each structure was analyzed in four basic configurations: (1) linear static, (2) nonlinear static, (3) linear dynamic, and (4) nonlinear dynamic. Within each of the four basic configurations, several parameters were varied (e.g., mesh size, time step, degree and type of nonlinearity) with the intent of determining their effect and developing confidence in the final prediction for the nonlinear dynamic response.

The general character of the finite element mesh used for the five structural problems is shown in Figure 3. The column idealization is used for the free field calculations, while the cavity idealization is used for the other four structures. The center of the cavity is set 252 inches (approximately 6 meters) below the surface of the mesh. The side boundaries of both meshes are constrained horizontally while the mesh bottom is fixed far enough from the region of interest to prevent any interference caused by reflecting waves. The pressure loads are applied uniformly across the top of the structure either statically or as functions of time (dynamic). Typically, a thousand degrees-of-freedom are used to model the cavity idealizations while fewer are needed for the free field modeling.

Materials

These structures are composed of five different types of materials:

- Tuff
- Steel
- Fiber reinforced concrete
- Reinforced concrete
- Cellular concrete

The material constants are listed in Table 1; their derivation is given in Appendix A. Two sets of properties are given for tuff: Tuff No. 2 is based on in-situ testing and Tuff No. 1 represents an earlier assessment of material behavior generated prior to the in-situ testing.

Geostatic Effects

The gravity effects are complicated by the employment of tunneling and grouting for structure emplacement. NONSAP could compute the geostatic stresses in tuff surrounding the tunnel. However, since the grout

surrounding the structures is in an unstressed condition (at least from gravity), and its dimensions uncertain (possibly 2-4 feet between structure and tunnel, and in the case of the sphere essentially unlimited along the tunnel axis), the inclusion of geostatic stresses seems unwarranted and somewhat specious. Also, since the estimated geostatic stress in the free field at the emplacement depth is only 70 bars², it does not appear the omission of gravitational forces will produce a serious degradation in predicted response.

Forcing Function

The forcing functions considered in this study are derived from the curves (supplied by Weidlinger and Associates³) shown in Figures 4 and 5. They consist of uniaxial velocity and stress at various locations with respect to the structure (where, for example, -6m denotes a point that is six meters upstream from the structure's center). These curves are derived analytically based on a CAP model⁴ characterization of the tuff. From these curves and through a study of the free field calculations (next section), the forcing function for the dynamic configurations was chosen. Two forms of this function are shown in Figure 6: one is a detailed description of the curve which was applied to all five structural problems while the other is a simplified version developed to aid in studying the effects of various parameters on the free field response. For the static analyses, a peak pressure of 7250 psi was used.

FREE FIELD VALIDATION AND DETERMINATION OF VARIOUS MESH PARAMETERS

Free Field Validation

This section presents the studies conducted to validate the accuracy of the free field responses computed by NONSAP. The basic premise is that the free field response which occurs in the tuff/structure meshes (presented in next section) is similar to what occurs in a columnar mesh (Figure 7) made of tuff only. The element and step size selected for the columnar mesh are based on the results presented in Appendix B. The elements are 20 inches in height, 4-node quadrilaterals, constrained laterally, and subjected at the mesh surface to the -6m stress wave shown in Figure 4. A time step of 0.4 msec is used to compute the results shown in Figures 8 and 9. Figure 8 shows stress versus time at element 24 for the linear elastic and the Drucker-Prager approximations of Tuff No. 1. Figure 9 shows velocity versus time for node 49. The +6 meter CAP model results, which correspond in depth to element 24 and node 49, are also shown in the figures, as well as the stress wave applied to the mesh.

The results of these free field runs indicate:

1. Comparisons of the vertical stress/velocity is not an appropriate method for checking the validity of the tuff material characterization. More germane would be the comparison of horizontal stresses or material stiffness predictions at the springline/crown of a lined cavity. These stresses are much more sensitive to variations between the various material models.

2. Velocity output does not compare as well as stress output.

3. No appreciable decrease in the peak stress with travel distance occurs for either the linear or Drucker-Prager models. Moreover, these two models yield similar results for the columnar idealization.

Compatibility of 4-Node and Higher Order Quadrilateral Elements

In certain regions of a mesh it is advantageous to join two 4 node quadrilateral elements to the side of an element of higher order (i.e., one with 5 to 8 nodes). Figure 10a shows such a case. Because the midside node of a higher order element is 4 times stiffer than its corner node, some anomaly is expected as a stress wave passes through the transition region. To investigate this phenomenon, the top surfaces of the three free field meshes shown in Figure 10 were subjected to a ramp loading of infinite duration. The results of this study are given in Appendix C. These results indicate that while a local anomaly in the displacement/stress field transpires, the effect at a point some distance from this region is negligible. Therefore, these transition zones will not be located near regions of interest.

Technique Employed for Removal of Reflection Waves

A significant aspect of predicting the transient response is insuring that the fictitious boundaries within the free field imposed by the finite element idealization do not become sources for spurious reflection waves. Because the forcing functions are uniaxial, the location and type of side boundaries employed appears to have little effect on the computations (see results for Mesh 3.0 and 3.1 of next section). Reflections caused by the bottom boundary can most simply be dealt with by establishing its location far enough from the region of interest. The depth of the region of interest is denoted as D_I while D_B is the additional depth of mesh necessary to avoid reflection waves, Figure 3. D_B is computed from the wave speed in tuff ($C = 57.5$ in/msec, from Appendix B) and the amount of time needed to capture the response (estimated to be no more than 35 msec). Therefore, the depth of mesh needed beyond the region of interest is:

$$D_B = (57.5) (35)/2 = 1000 \text{ inches}$$

Selecting the depth of the region of interest (D_I) to be 500 inches, yields the total depth of mesh:

$$D = D_B + D_I = 1500 \text{ inches}$$

Since the element size needed in this region is 40 inches (see Appendix B) the total number of degrees of freedom needed to model this space is:

$$\text{DOF (for 4-node quads)} = 1000/40 (2) = 50$$

$$\text{DOF (for 8-node quads)} = 1000/40 (5) = 125$$

where one element is presumed to cover the whole space laterally. Whichever element type is employed, the number of degrees-of-freedom used to model this space is inconsequential compared to the total degrees-of-freedom for the whole model (i.e., more than 1000). Using more complicated schemes, such as nodal dampers, does not seem warranted in these circumstances.

Computation of Residual Response

A possible scheme for computing residual response consists of a deep mesh of successively larger element sizes used in conjunction with the NONSAP restart option, whereby a small time step is used until the peak response of the structure occurs. Then gradually larger time steps are employed until the structure is in static equilibrium. An example of this technique is shown in Appendix D. In general, for these types of problems, this technique appears to provide a way to reduce computer costs for large runs and to be a feasible means of computing response over a long period of time.

Use of Velocity as Forcing Function

NONSAP does not allow direct input of velocity as a forcing function. To use velocity data, it must be integrated to provide a displacement-time history. Then using the "stiff spring trick" (described in Appendix E), these displacements are used to drive the problem. Since both pressure and velocity data were provided, there was no need to perform these operations for any of the analyses reported. However, for comparative purposes, a free field calculation based on these techniques is included in Appendix E.

ANALYSIS OF A CYLINDRICAL CAVITY WITHIN THE FREE FIELD

Four meshes were made to model a cylindrical cavity (72 inches in diameter) within a homogeneous tuff. Such parameters as mesh boundaries; element sizes, types, and shapes; and linear versus nonlinear materials and deformation were studied. These studies were carried out for both an unlined cavity and one lined with a thin steel shell (0.78 inches thick). The steel-lined cavity results are included to make the parametric studies relevant to the Mighty Epic structures.

For this analysis, seven static and seven dynamic problem configurations were deemed to be of interest. These are:

1. An elastic tuff with an unlined cavity (denoted SC1 and DC1).
2. A Drucker-Prager tuff with an unlined cavity (denoted SC2 and DC2).
3. An elastic tuff with an unlined cavity using the large deformation formulation and equilibrium iteration (denoted SC3 and DC3).
4. A Drucker-Prager tuff with an unlined cavity using the large deformation formulation and equilibrium iteration (denoted SC4 and DC4).
5. An elastic tuff with an elastic steel-lined cavity (denoted SC5 and DC5).

6. A Drucker-Prager tuff with an elastic steel-lined cavity (denoted SC6 and DC6).

7. A Drucker-Prager tuff with an elastic steel-lined cavity using the large deformation formulation and equilibrium iteration (denoted SC7 and DC7).

The following four meshes were used:

Mesh 3.0: Conventional 4-node quadrilateral mesh where the right boundary is set at $Y = 288$ inches. The thin liner consists of thirty-two 8-node quadrilaterals connected by 5-node quadrilaterals to the rest of the mesh, Figure 11a.

Mesh 3.1: Identical to Mesh 3.0 except that additional elements have been added to the right side moving the right boundary to $Y = 435$ inches, Figure 11b.

Mesh 3.2: Similar to Mesh 3.0 except that 8-node quadrilaterals have (approximately) replaced groups of four 4-node quadrilaterals. The thin liner consists of only sixteen 8-node quadrilaterals, Figure 11c.

Mesh 3.3: Provides a rectangular mesh for contrast with the previous radial meshes. The thin liner consists of eighteen 8-node quadrilaterals which are connected by 5-node quadrilaterals to the rest of the 4-node quadrilateral mesh.

Only the upper region of each mesh is shown in Figure 11. The lower regions are similar in depth to Figure 3b.

These four meshes are presumed to provide sufficient data for evaluation of right boundary selection; element sizing, layout and type; and the effect of mesh selection on response predictions. Both static and dynamic responses were obtained at the mesh locations shown in Figure 12. The static responses were included in Table 2-5, while the peak dynamic responses were included in Tables 6-9. A typical dynamic response for the four meshes is shown in Figure 13. The seven problem configurations were not run for every mesh, owing to expected similarities of results.

The response of each mesh for a particular problem configuration is essentially the same. Comparison of Mesh 3.3 to the other meshes indicates that the easily generated radial meshes can satisfactorily be employed in the structural meshes. Comparison of Meshes 3.0 and 3.1 indicates that a right boundary of 288 inches is satisfactory. Comparison of Meshes 3.0 and 3.2 indicates that sixteen 8-node quadrilaterals are adequate to handle the bending present in a thin liner, and 8-node quadrilaterals can replace groups of four 4-node quadrilaterals in the medium. Comparison of Runs SC6 and SC7 indicates that when the steel liners are employed, deflections are so small that large deformation theory is not necessary.

RESULTS OF ANALYSES OF MIGHTY EPIC STRUCTURES

Based on the results of the previous section and various finite element analyses of the structures alone, the following three structural meshes were generated:

Mesh 4.0: Homogeneous Sphere - Conventional 4-node quadrilateral mesh where the right boundary is set at $Y = 288$ inches. The concrete sphere consists of six layers of 4-node quadrilaterals.

Mesh 5.0: Composite Built-Up Liner - Conventional 8-node quadrilateral mesh. The steel liner and cellular concrete consists of 1 and 2 element layers, respectively.

Mesh 6.0: Composite Integral Liner - Identical in topology to Mesh 5.0.

The upper region of each mesh is shown in Figures 14, 15 and 16. For each mesh, four different runs were made:

1. Linear static.
2. Nonlinear static, where the nonlinear material properties of Table 1 were employed and small deformation theory was assumed valid.
3. Linear dynamic, where $\Delta t = 0.4$ msec and 44 steps were employed.
4. Nonlinear dynamic, where the material characterizations of Run 2 and the time parameters of Run 3 were employed.

Homogeneous Sphere (Figure 1)

Since the designers of the homogeneous sphere based their design on the stress distribution within a thick-walled sphere subjected to a uniform external pressure, the elastic thick-wall theory in its general form is given below:

$$S_t = \frac{p_o r_o^3}{2r^3} \left(\frac{r_i^3 + 2r^3}{r_o^3 - r_i^3} \right)$$
$$S_r = \frac{p_o r_o^3}{r^3} \left(\frac{r^3 - r_i^3}{r_o^3 - r_i^3} \right)$$

where:

- S_t = wall stress in tangential direction (psi)
- S_r = wall stress in radial direction (psi)
- p_o = external pressure (psi)
- r_o = external radius (in)
- r_i = interior radius (in)
- r = radius to location in wall under consideration (in)

Using these equations, an external pressure of 7250 psi acting on the sphere shown in Figure 1 would produce tangential and radial stresses of -15,450 psi and 0 psi at the inner surface and -11,820 psi and -7250 psi at the outer surface. The diameter change of the sphere with the elastic properties shown in Table 1 would equal -0.17 in.

The static and dynamic peak responses computed by the finite element model for the sphere are listed in Table 10 (see Figure 12 for mesh locations). The diameter change for the nonlinear dynamic run is shown in Figure 17. Because the dynamic peak response is similar to the static peak response, only the static results will be discussed.

The employment of the nonlinear models for the tuff and the fiber reinforced concrete did affect the structural response. All of the relatively weak Tuff No. 1 elements became plastic, while all of the concrete elements stayed elastic. Thus, the difference between the linear and the nonlinear runs is entirely caused by the yielding of the tuff elements. The interior vertical diameter change for the linear (-0.32 in) and the nonlinear (-0.24 in) runs both exceeded the theoretical change (-0.17 in). The respective interior horizontal changes (+0.02 and -0.02 in) were negligible. Thus, the displaced shape of the sphere at peak static load is oval. This lack of hydrostatic behavior is also evident in the radial stresses of the tuff elements adjacent to the sphere. For the elastic run, the peak radial stress is -10,500 psi at the crown and -3300 psi at the springline. For both runs, the greatest concrete stresses occur at the springline interior in the tangential direction. The Drucker-Prager tuff reduces this tangential stress from -31,250 psi to -24,210 psi. However, this is still greater than the theoretical value (15,450 psi). This indicates a negative arching behavior for the structure. This behavior is also evident by observing the vertical tuff stresses at the crown and the springline. The stress at the crown (-9150 psi) is greater than the incident peak (-7250 psi), while the stress at the springline (-5400 psi) is less. The non-hydrostatic loading produces both thrust and moment in the sphere. Positive bending (exterior fibers in compression) occurs at the crown and invert, while negative bending occurs at the springline. The amount of positive bending at the crown is enough to cause the highest compressive tangential stresses to occur at the exterior rather than the interior surface. For the nonlinear run, the tangential stress is -13,200 psi at the exterior and -7350 psi at the interior.

Composite Built-Up Liner (Figure 1)

The static and dynamic peak responses are listed in Table 11. The diameter change for the nonlinear dynamic run is shown in Figure 18. Like the homogeneous sphere, the dynamic peak response is similar to the static peak response. For brevity, only the static results will be discussed.

Positive arching is indicated because the vertical tuff stress at the crown is less than at the springline. For the nonlinear run, the stress at the crown (-3200 psi) is less than the incident peak (-7250 psi), while the stress at the springline (-9360 psi) is greater. Thus, the Elastic and the Curve Description models which were derived for the cellular concrete, act as a well-designed back-packing material. The displaced shape for both runs is oval. The inside diameter changes in the vertical direction are -0.65 in and -0.86 in, and in the horizontal direction are +0.65 in and +.82 in, for the linear and nonlinear runs, respectively.

Unlike the Tuff No. 1 in the homogeneous sphere mesh, only the tuff elements adjacent to the liner yield. This is primarily because of the increased strength of the Tuff No. 2 model. This yielding plus the yielding in the steel liner are the principal reasons for the difference between the linear and nonlinear structural response. At the maximum load, yielding of the outer fibers in the steel elements near the springline occurred. Yielding is sufficient to cast doubt on the validity of the linear run. Positive bending occurs at the crown while negative bending occurs at the springline of the steel liner. For the nonlinear run, the hoop stress at the crown varies from +6800 psi at the inner surface to -44,120 psi at the outer surface. At the springline it varies from -46,220 psi at the inner surface to -11,430 at the outer surface.

Composite Integral Liner (Figure 2)

The static and dynamic peak responses are listed in Table 12. The diameter change for the nonlinear dynamic run is shown in Figure 19. Because the dynamic peak response is similar to the static peak response, only the static results will be discussed. The displaced shape of the liner is oval. The inside diameter changes for the linear and nonlinear runs in the vertical direction are -0.62 in and -0.84 in, and in the horizontal direction are +0.26 in and +0.28 in, respectively. The vertical tuff stresses at the crown are -6410 psi (linear) and -5560 psi (nonlinear), respectively. This indicates positive arching behavior. The high strength of the Tuff No. 2 model combined with the structure-media interaction produces no yielding of the tuff elements in the nonlinear run. Thus, the difference between the linear and nonlinear results is caused only by the nonlinear behavior of the steel and concrete. For the nonlinear run, the steel hoop stress at the crown varies from -18,170 psi at the inner surface to -34,420 psi at the outer surface. At the springline it varies from -46,660 psi to -47,860 psi. Compression yielding of the steel liner occurs throughout the entire thickness from $\pm 45^\circ$ about the springline. This extensive yielding casts doubt on the validity of the linear run as is verified by the pre-posterous steel centroidal hoop stress of -214,410 psi at the springline. Examination of the concrete hoop and radial stresses indicates a thick-wall cylinder behavior for the concrete shell. The radial stress at any location varies throughout the thickness, while the much larger hoop stresses transmit the load around the cavity. At the maximum load, the concrete is plastic to $\pm 45^\circ$ from the springline throughout its entire thickness. The concrete hoop stress at the crown varies from -5510 psi at the inner surface to -17,840 psi at the outer surface, and at the springline it varies from -45,570 psi to -28,870 psi. This maximum hoop stress at the springline is approximately eight times the unconfined compressive strength ($f'_c = 5500$ psi). References presented in Appendix A indicate that plain concrete subjected to multi-axial loading exhibits more ductility and higher strength than concrete subjected to uniaxial or biaxial loading. The extremely high concrete stresses seem in line with experimental data.

SUMMARY

Based on these response calculations, the three Mighty Epic structures seem adequate for the 0.5 Kbar load level. However, this conclusion is predicated on the appropriateness of the material models. This is of particular concern for the concrete models, which were derived from little more than estimated values of f'_c . Significant confidence in calculations can not be established until better material data is gathered and its validity checked against prototype structures.

ACKNOWLEDGMENTS

This study was sponsored by the Defense Nuclear Agency under Subtask Y99QAXSC318. Dr. Kent Goering monitored the work and provided valuable assistance and information necessary for the calculations.

The authors gratefully acknowledge the assistance provided by Mr. V. J. Gerwe, structural engineering technician (CEL) in preparing the figures.

Table 1. Material Properties

Material	Structure					Linear Model		Drucker-Prager Model		von-Mises Model		Curve Description Model
	Free Field	Cavity	Homogeneous Sphere	Composite Built-Up Lining	Composite Integral Lining	Young's Modulus E (psi)	Poisson's Ratio	Cohesion c (psi)	Friction Angle ϕ (Degrees)	Yield Stress σ_y (psi)	Post Yield Modulus E_T (psi)	
Tuff No. 1	X	X	X			448,173	0.286	435	9.23			
Tuff No. 2				X	X	600,000	0.286	1100	18			
Steel		X				30,000,000	0.30					
Steel				X		30,000,000	0.30			36,000	30,000	
Steel					X	30,000,000	0.30			40,000	30,000	
Fiber Reinforced Concrete			X			5,700,000	0.24	3600	35			
Reinforced Concrete					X	4,264,000	0.17	1980	35			
Cellular Concrete				X								See Appendix A

Table 2. Static Results for Mesh 3.0

Prob ID	Description	Material Model For		Large Deform. (# of Steps)	Tuff Response: $\delta_x, \delta_y, \delta_z, \sigma_x, \sigma_y, \sigma_z, \tau_{xy}, \tau_{yz}, \tau_{zx}$ Order in Columns													Liner Response: $\sigma_x, \sigma_y, \sigma_z, \tau_{xy}, \tau_{yz}, \tau_{zx}$								
		*Tuff	Cavity Liner		A ^a	B	C	D	E	F	G	H	I	J	K	L										
SC1	Linear elastic unlined cavity	Linear elastic	Linear elastic tuff	No (1)	57	33	113	57	10	129	234	144	233	128	228	124	225	121	458	144	1	16	32			
					-19.25	-19.11	-19.00	-17.22	0.0	0.0	-15.86	-15.84	-15.86	-15.84	-14.51	-100	-18160	-100	-1940							
					0.0	-0.08	0.0	0.0	-0.09	-0.01	-0.02	0.0	0.0	0.0	0.0	-1880	-190	-1940								
					-7200	-7280	-7260	-800	-14830	-10890	-7670	-7390	-790	100	870	100	870	-110								
					-3340	-2800	-2620	-2960	-1910	-3210	-3150	-3050	-3000													
SC2	Nonlinear unlined cavity	Drucker-Prager	Drucker-Prager tuff	No (16)	40	90	40	280	280	470	470	130	30	10	280											
					-22.3	-22.1	-21.6	-20.9	-18.2	-18.2	-18.2	-18.2	-15.62	-3320	-8100	-3290										
					0.0	-0.35	0.0	0.0	-1.62	-0.90	-0.16	0.0	0.0	0.0	-6230	-6190										
					-7220	-7270	-7465	-3300	-8500	-8700	-8100	-7520	-3260	143	170	-140										
					-5160	-4460	-4520	-6200	-4850	-6000	-5040	-5900	-6148													
SC3	Linear elastic unlined cavity, incl. large deformation	Linear elastic	Linear elastic tuff	Yes (16)	30	165	284	143	160	160	165	165	96	20	142											
					-19.30	-19.1	-19.0	-17.2	-15.86	-15.86	-15.84	-15.83	-14.51	-98	-18160	-98										
					0.0	-0.08	0.0	0.0	-0.094	-0.094	0.025	0.0	0.0	0.0	-1878	-191	-1942									
					-7200	-7280	-7250	-795	-14830	-10890	-7670	-7400	-790	104	870	104	870	-106								
					-3340	-2800	-2620	-2960	-1910	-3200	-3150	-3050	-2998													
SC4	Nonlinear unlined cavity, incl. large deformation	Drucker-Prager	Drucker-Prager tuff	Yes (16)	38	87	35	283	470	470	128	25	8	280												
SC5	Linear elastic tuff with steel lined cavity	Linear elastic	Linear elastic steel	No (1)	-18.9	-18.9	-18.9	-16.5	-15.7	-15.7	-15.7	-15.7	-15.7	-15.7	-15.7	-15.7	-15.7	-15.0	-15.0	-1747	-325000	-1744				
					0.0	0.026	0.0	0.0	0.279	0.217	0.051	0.0	0.0	0.0	0.0	0.0	0.0	0.0	0.0	0.0	-125000	-3480	-124500			
					-7225	-7250	-7250	-4030	-7150	-7250	-7260	-7238	-4035	-3556								6144	78191	-6145		
					-2999	-2890	-2860	-3500	-5900	-4650	-3210	-3064	-3556													
					20	40	20	400	-250	-191	-16	-19	-74													
SC6	Nonlinear tuff with steel lined cavity	Drucker-Prager	Linear elastic steel	No (16)	-21.5	-21.4	-21.3	-18.8	-17.83	-17.83	-17.83	-17.83	-17.81	-17.81	-17.81	-17.81	-17.81	-16.86	-16.86	-2600	-317700	-2600				
					0.0	-0.089	0.0	0.0	0.412	0.346	0.117	0.0	0.0	0.0	0.0	0.0	0.0	0.0	0.0	0.0	-208500	-3516	-208500			
					-7220	-7250	-7280	-5500	-7100	-7250	-7250	-7230	-5500	-5280								10200	15400	-10200		
					-4570	-4500	-4480	-5200	-6000	-5230	-4650	-4580	-5280													
					6.0	-50	-30	-25	-240	-90	-10	5.0	-18													
SC7	Nonlinear tuff with steel lined cavity, incl. large deformation	Drucker-Prager	Linear elastic steel	Yes (16)																						

^aLocation of response, see Figure 12. All values of stress/strain taken from element centroid.
^bNode number associated with displacement (inches) (δ_x vertical, and δ_y horizontal).
^cElement number associated with stress/strain (σ_x and τ_{xy} vertical, σ_y and τ_{yz} horizontal, and σ_z and τ_{zx} shear) (psi/ μ in per in).

Table 3. Static Results for Mesh 3.1

Prob. ID.	Description	Material Model Use		Large Factor (# of Steps)	Tuff Response: $\delta_x, \delta_y, \delta_z, \sigma_x, \sigma_y, \sigma_z, \epsilon_x, \epsilon_y, \epsilon_z$ Order in Columns																Liner Response: $\sigma_x, \sigma_y, \sigma_z, \epsilon_x, \epsilon_y, \epsilon_z$					
		Tuff	Cavity Liner		A ^a	B	C	D	E	F	G	H	I	J	K	L										
SC1	Linear elastic unlined cavity	Linear elastic	Linear elastic tuff	No (1)	85	56	113	2	10	129	-23.1	-20.0	252	144	251	128	244	124	241	16	492	144	1	16	32	
SC2	Nonlinear unlined cavity	Drucker-Prager	Drucker-Prager tuff	No (16)	-24.5		-22.7					-20.0	-20.0	-19.6	-19.4	-17.0	-17.0	-17.0	-17.0	-17.0	-17.0	-17.0	-17.0	-17.0	-17.0	-17.0
		Linear elastic	Linear elastic tuff		0.0		0.0		0.0	0.0	0.0	1.78	-0.92	0.40	0.0	0.0	0.0	0.0	0.0	0.0	0.0	0.0	0.0	0.0	0.0	0.0
		Drucker-Prager	Drucker-Prager tuff		-7250		-7400		-3700	-9600	-9720	-5660	-5660	-8760	-3580	-7870	-5450	-5250	-6630	-6630	-6630	-6630	-6630	-6630	-6630	-6630
		Linear elastic	Linear elastic tuff		-5680		-4500		-6800	-5600	-5660	-5660	-5660	-5450	-6630	-5250	-5250	-5250	-6630	-6630	-6630	-6630	-6630	-6630	-6630	-6630
SC3	Linear elastic unlined cavity, incl. large deformation	Linear elastic	Linear elastic tuff	Yes (16)	22		-19.9		-18.4	-16.96	-16.96	-16.96	-16.96	-16.82	-16.7	-15.5	-104	-20630	-102	-102	-102	-102	-102	-102	-102	-102
		Linear elastic	Linear elastic tuff		0.0		0.0		0.0	0.0	0.0	-0.07	-0.02	0.068	0.0	0.0	0.0	0.0	0.0	0.0	0.0	0.0	0.0	0.0	0.0	0.0
		Drucker-Prager	Drucker-Prager tuff		-7245		-7250		-830	-16560	-12000	-12000	-12000	-8500	-7540	-825	-104	-20630	-102	-102	-102	-102	-102	-102	-102	-102
		Linear elastic	Linear elastic tuff		-3430		-2520		-3140	-2280	-3660	-3660	-3660	-3360	-3260	-3050	-1890	-230	-1815	-1815	-1815	-1815	-1815	-1815	-1815	-1815
SC4	Nonlinear unlined cavity, incl. large deformation	Drucker-Prager	Drucker-Prager tuff	Yes (16)	22		2		300	510	110	110	110	100	60	-295										
		Linear elastic	Linear elastic tuff		-20.5		20.1		-18.0	-17.2	-17.2	-17.2	-17.2	-17.1	-16.9	-16.3	-1900	-357900	-1850	-1850	-1850	-1850	-1850	-1850	-1850	-1850
		Linear elastic	Linear elastic tuff		0.0		0.0		0.0	0.32	0.25	0.25	0.25	0.08	0.0	0.0	-134000	-3800	-132800	-132800	-132800	-132800	-132800	-132800	-132800	-132800
		Drucker-Prager	Drucker-Prager tuff		-7280		-7250		-4200	-8150	-8100	-8100	-8100	-8050	-7570	-4180	6620	-17400	-6500	-6500	-6500	-6500	-6500	-6500	-6500	-6500
		Linear elastic	Linear elastic tuff		-3020		-2650		-3390	-6600	-5130	-5130	-5130	-3400	-3300	-3333										
SC6	Nonlinear tuff with steel lined cavity	Drucker-Prager	Linear elastic steel	No (16)	-9		1		370	-340	-210	-210	460	55	-376											
		Drucker-Prager	Linear elastic steel																							
SC7	Nonlinear tuff with steel lined cavity, incl. large deformation	Drucker-Prager	Linear elastic steel	Yes (16)																						

^aLocation of response, see Figure 12. All values of stress/strain taken from element centroid.
^bNode number associated with displacements (inches) δ_x , vertical, and δ_y horizontal.
^cElement number associated with stress/strain (σ_x and σ_z vertical, σ_y and ϵ_y horizontal, and σ_{xy} and ϵ_{xy} shear) (psi/ μ in per in).

Table 4. Static Results for Mesh 3.2

Prob. ID.	Description	Material Model For		Large Deform. (# of Steps)	Tuff Response: $\delta_x, \delta_y, \delta_z, \sigma_x, \sigma_y, \sigma_z, \epsilon_x, \epsilon_y, \epsilon_z$ - Dynamic Order of Columns																Steel Liner Response: $\sigma_x, \sigma_y, \sigma_z, \epsilon_x, \epsilon_y, \epsilon_z$				
		Tuff	Cavity Liner		A ^a	B	C	D	E	F	G	H	I	J	K	L	M	N	O	P					
SC1	Linear elastic unlined cavity	Linear elastic	Linear elastic tuff	No (1)	41	11	81	16	11	5	171	40	170	39	166	38	161	36	331	80	1	8	16		
					-19.38	-19.23	-19.14	-17.36	-15.98	-15.98	-15.98	-15.98	-15.97	-15.95	-14.62	-69	-18171	-69	-1890	-244	-1999	-212			
					0.0	-0.09	0.0	0.0	-0.09	-11093	-8509	-7804	-7804	-3162	-3049	-3721									
SC2	Nonlinear unlined cavity	Drucker-Prager	Drucker-Prager tuff	No (16)	83	+121	+58	+748	+413	+15	-27.65	-25.62	-23.14	-32.16	-21.45	-17.67	-12.77	-0.49	0.0	0.0	-1651	+361	-1646		
					-7164	-7287	-7279	-2022	-11093	-8509	-7804	-7804	-3162	-3049	-3721										
					-3207	-2825	-2710	-3687	-2348	-3295	-3162	-3049	-3721												
SC3	Linear elastic unlined cavity, incl. large deformation	Linear elastic	Linear elastic tuff	Yes (16)	+328	+1036	+308	+527	+152	+224	-19.06	-18.91	-18.81	-17.07	-15.72	-15.72	-15.70	-15.68	-14.38	65	-18653	-66			
					0.0	-0.09	0.0	0.0	-0.08	+6399	-2376	-6798	-8832	+9053	+379	+101	+517								
					-7170	-7285	-7273	-1989	-11038	-8484	-7789	-7377	-1954	-3672											
SC4	Nonlinear unlined cavity incl. large deformation	Drucker-Prager	Drucker-Prager tuff	Yes (16)	85	119	56	740	393	7															
					-19.07	-19.01	-18.98	-16.63	-15.86	-15.86	-15.85	-15.85	-15.85	-15.09	-2090	-322047	-2080								
					0.0	-0.03	0.0	0.0	0.29	-7220	-7265	-7259	-4738	-7478	-7356	-7300	-7238	-4713	12279	-31791	-12238				
SC5	Linear elastic tuff with steel lined cavity	Linear elastic	Linear elastic steel	No (1)	-2991	-2877	-2852	-2849	-5137	-3724	-3281	-3066	-2865	-2865	-2865	-2865	-2865	-2865	-2865	-2865	-2865	-2865			
					29	33	12	527	-397	-133	-46	-518	-518	-518	-518	-518	-518	-518	-518	-518	-518	-518	-518	-518	
					-21.81	-21.71	-21.53	-19.16	-18.12	-18.12	-18.12	-18.12	-18.12	-18.12	-18.12	-18.12	-18.12	-18.12	-18.12	-18.12	-18.12	-18.12	-18.12	-18.12	-18.12
SC6	Nonlinear tuff with steel lined cavity	Drucker-Prager	Linear elastic steel	No (16)	0.0	-0.14	0.0	0.0	0.51	0.42	0.21	0.21	0.21	0.21	0.21	0.21	0.21	0.21	0.21	0.21	0.21	0.21			
					-7225	-7280	-7294	-5808	-7557	-7431	-7312	-7253	-5795	20887	-30675	-20737									
					-4614	-4474	-4470	-4378	-5709	-5004	-4782	-4631	-4388												
SC7	Nonlinear tuff with steel lined cavity, incl. Large deformation	Drucker-Prager	Linear elastic steel	Yes (16)	17	55	8	318	246	-66	-21.40	-21.26	-21.02	-18.85	-17.74	-17.74	-17.73	-17.69	-16.64	-3308	-307537	-3271			
					-7225	-7280	-7294	-5808	-7557	-7431	-7312	-7253	-5795	20887	-30675	-20737									
					-4614	-4474	-4470	-4378	-5709	-5004	-4782	-4631	-4388												

^aLocation of Response, see Figure 12. All values of stress/strain taken from element centroid.
^bNode number associated with displacements (δ_x , vertical, and δ_y , horizontal).
^cElement number associated with stress/strain (σ_x , vertical, and σ_y , horizontal, and ϵ_x and ϵ_y , shear).

Table 6 Dynamic Results for Mesh 3.0

Prob. ID.	Description	Material Model For		Large Deform. (# of Steps)	Tuff Response ^d $\delta_x, \delta_y, \delta_z, \sigma_x, \sigma_y, \sigma_z, \dots$ (Time of Peak Stress) Order in Columns													Liner Response $\sigma_x, \sigma_y, \sigma_z, \tau_{xy}, \tau_{yz}, \tau_{xy}, \tau_{yz}$						
		Tuff	Cavity Liner		A ^a	B	C	D	E	F	G	H	I	J	K	L								
DC1	Linear elastic unlined cavity	Linear elastic	Linear elastic tuff	No (44)	57	33	113	57	10	129	234	144	233	128	228	124	225	121	458	144	1	16	32	
DC2	Nonlinear unlined cavity	Drucker-Prager	Drucker-Prager tuff	No (44)																				
DC3	Linear elastic unlined cavity, incl. large deformation	Linear elastic	Linear elastic tuff	Yes (44)																				
DC4	Nonlinear unlined cavity, incl. large deformation	Drucker-Prager	Drucker-Prager tuff	Yes (44)																				
DC5	Linear elastic tuff with steel lined cavity	Linear elastic	Linear elastic steel	No (44)	-6.99	-6.93	-6.84	-5.20	-4.55	-4.55	-4.55	-4.55	-4.55	-4.55	-4.59	-4.55	-4.55	-3.89	-1680	-320980	-1650			
					0.0	-0.06	0.0	0.0	0.25	0.20	0.07	0.0	0.0	0.0	0.0	0.0	0.0	0.0	-121210	-3400	-117910			
					-7.260	-7.280	-7.210	-3.670	-7.217	-7.150	-6.990	-7.090	-7.150	-6.990	-7.090	-3.640	-7.090	-2.930	5990	15570	-5830			
					-2920	-2920	-2870	-2970	-5940	-4.650	-3.170	-2.940	-4.650	-3.170	-2.940	-3.40	-3.40	-3.40						
					5	9	-1	310	-330	-170	-7													
					(10.4)	(10.4)	(10.4)	(13.6)	(15.2)	(15.2)	(14.4)	(14.4)	(15.2)	(15.2)	(14.4)	(15.2)	(15.2)	(14.4)	(14.4)	(15.2)	(15.2)	(15.2)	(15.2)	
					-7.44	-7.36	-7.24	-5.43	-4.63	-4.63	-4.59	-4.57	-4.63	-4.59	-4.57	-3.74	-3.74	-3.74	-2428	-298613	-2475			
					0.0	-0.07	0.0	0.0	+0.40	+0.34	+0.10	0.0	0.0	0.0	0.0	0.0	0.0	0.0	-198393	-3325	-204448			
					-7.231	-7.226	-7.173	-4.881	-7.055	-7.171	-7.047	-6.994	-7.055	-7.171	-7.047	-5.058	-5.058	-5.058	-4555	+9729	+14511	-10024		
					-4.498	-4.492	-4.454	-4.504	-5.891	-5.246	-4.570	-4.369	-5.246	-4.570	-4.369	-4.555	-4.555	-4.555						
					+3	-2	-3	194	-210	-101	-52	-30	-203	-203	-203	-203	-203	-203						
					(10.4)	(10.4)	(10.4)	(14.4)	(15.2)	(15.2)	(15.2)	(15.2)	(15.2)	(15.2)	(15.2)	(16.0)	(16.0)	(15.2)	(14.4)	(15.2)	(15.2)	(15.2)	(15.2)	
					-7.40	-7.31	-7.18	-5.44	-4.62	-4.62	-4.59	-4.56	-4.62	-4.59	-4.59	-3.70	-3.70	-3.70	-2467	-295135	-2532			
					0.0	-0.08	0.0	0.0	+0.45	-0.39	+0.12	0.0	0.0	0.0	0.0	0.0	0.0	0.0	-199611	-3528	-207253			
					-7.262	-7.258	-7.200	-4.810	-7.147	-7.275	-7.070	-7.028	-7.275	-7.070	-7.147	-7.028	-7.147	-7.028	+9603	+15373	-9979			
					-4.521	-4.517	-4.471	-4.504	-6.066	-5.456	-4.636	-4.353	-6.066	-5.456	-4.636	-4.353	-4.353	-4.353						
					+3	-2	-6	+181	-276	-137	-56	-48	-276	-137	-56	-48	-48	-276						
					(10.4)	(10.4)	(10.4)	(14.4)	(15.2)	(15.2)	(15.2)	(14.4)	(15.2)	(15.2)	(15.2)	(14.4)	(14.4)	(15.2)	(14.4)	(15.2)	(15.2)	(15.2)	(15.2)	

^aLocation of response, see Figure 12. All values of stress/strain taken from element centroid.

^bNode number associated with displacements (δ_x , vertical, and δ_y , horizontal).

^cElement number associated with stress/strain (σ_x and σ_y , vertical, and τ_{xy} and τ_{yz} , horizontal, and σ_x, σ_y and τ_{xy} , shear).

^dOnly the peak responses are shown. The peak displacements occur at the end of the run at 17.6 msec while the peak stresses and strains occur at the times indicated in parentheses.

Table 8. Dynamic Results for Mesh 3.2

Prob ID	Description	Material Model For		Large Deform. = of Steps	Tuff Response: $\delta_v, \delta_H, \sigma_x, \sigma_y, \sigma_z, \epsilon_x, \epsilon_y, \epsilon_z$ (Time of Peak Stress) Order in Columns																Liner Response: $\sigma_x, \sigma_y, \sigma_z, \epsilon_x, \epsilon_y, \epsilon_z$							
		Tuff	Cavity Liner		A ^a	B	C	D	E	F	G	H	I	J	K	L												
DC1	Linear elastic unlined cavity	Linear elastic	Linear elastic tuff	No (44)	1 ^b	41	81	16	11	5	171	40	170	39	166	38	161	36	331	80	1	8	16					
DC2	Nonlinear unlined cavity	Drucker-Prager	Drucker-Prager tuff	No (44)																								
DC3	Linear elastic unlined cavity, incl. large deformation	Linear elastic	Linear elastic tuff	Yes (44)																								
DC4	Linear elastic tuff with steel lined cavity	Drucker-Prager	Drucker-Prager tuff	Yes (44)																								
DC5	Linear elastic tuff with steel lined cavity	Linear elastic	Linear elastic steel	No (44)	-6.98	-6.91	-6.83	-5.19	-4.54	-4.55	-4.58	-3.86	-1988	-315684	-1910	0.0	-0.01	-7029	-6976	-4483	-7253	-7048	-7019	-6903	-4445	11651	-31156	-11322
DC6	Nonlinear tuff with steel lined cavity	Drucker-Prager	Linear elastic steel	No (44)	-7.34	-7.34	-7.14	-5.39	-4.59	-4.60	-4.66	-3.70	-3178	-297236	-3327	0.0	0.04	-6940	-6977	-3267	-7142	-7072	-7009	-6872	-5468	19248	-29061	-19744
DC7	Nonlinear tuff with steel lined cavity, incl. large deformation	Drucker-Prager	Linear elastic steel	Yes (44)	-7.30	-7.29	-7.09	-5.40	-4.58	-4.59	-4.65	-3.65	-3137	-283866	-3213	0.0	0.04	-6963	-6988	-5140	-7246	-7102	-7036	-6929	-5392	19048	-4397	-204062
					-4.339	-4.244	-4.348	-4.243	-5.674	-5.017	-4.685	-4.283	-4.244	19048	28704	-19483	18	-5	114	306	-257	-37	-71	-67	-283	19048	28704	-19483
					(10.4)	(10.4)	(11.2)	(14.4)	(15.2)	(15.2)	(15.2)	(16.0)	(14.4)	(14.4)	(15.2)	(15.2)	(10.4)	(10.4)	(11.2)	(14.4)	(15.2)	(15.2)	(14.4)	(14.4)	(16.0)	(14.4)	(14.4)	(15.2)

^aLocation of response, see Figure 12. All values of stress/strain taken from element centroid.
^bNode number associated with displacements (δ_v , vertical, and δ_H , horizontal).
^cElement number associated with stress/strain (σ_x and ϵ_x , vertical, σ_y and ϵ_y , horizontal, and σ_z and ϵ_z , shear).
^dOnly the peak responses are shown. The peak displacements occur at the end of the run at 17.6 msec while the peak stresses and strains occur at the times indicated in parentheses.

Table 10. Results for Homogeneous, Fiber Reinforced, Concrete Sphere (Mesh 4.0) - Static at Full Load; Dynamic at Peak

Prob ID	Description	Material Model For		Large Deform. (= of Steps)	Tuff Response: $\delta_v, \delta_H, \sigma_x, \sigma_y, \sigma_z, \tau_{xy}, \tau_{yz}, \tau_{zx}$ - Static - (Order in Columns)													Concrete Response: $\sigma_x, \sigma_y, \sigma_z, \tau_{xy}, \tau_{yz}, \tau_{zx}$ - Dynamic					
		Tuff	Cavity Liner		A	B	C	D	E	F	G	H	I	J	K	L	M	N	O				
SHS1	Linear elastic material STATIC	Linear elastic	Fiber concrete E = 5700000 ν = 0.24	No (1)	1	65.28	129.64	10.9	266.144	265.143	262.140	257.136	522.144	6	96	96							
					-18.83	-18.84	-18.85	-15.88	-15.72	-15.72	-15.72	-15.71	-15.56	-380	-31250	-380							
					0.0	0.005	0.0	0.0	0.017	-0.02	-0.01	0.0	0.0	0.0	0.0	-4000	-1550	-4000					
					-7260			-10500	-4630	-6400	-7180	-7250				720	1380	-715					
					-2860			-4050	-3300	-2700	-2830	-2880											
SHS2	Nonlinear material STATIC	Drucker-Prager	Drucker-Prager φ = 35° c = 3600	No (15)	-5	-21.4	-21.4	-17.94	-17.83	-17.83	-17.84	-17.85	-17.71	-650	-24210	-650							
					0.0	0.013	0.0	0.0	-0.005	-0.05	-0.04	0.00	0.0	-7350	-1400	-7420							
					-7250			-9150	-5400	-6700	-7240	-7246			700	1140	-710						
					-4500			-5900	-4380	-4000	-4450	-4500											
					1			-12	-240	6	7	2											
DHS1	Linear material DYNAMIC	Linear elastic	Same as SHS1	No (44)	-6.51	-6.61	-6.60	-4.47	-4.35	-4.36	-4.37	-4.38	-4.22	-370	-29200	-370							
					-7060	-7080	-7010	-9970	-4370	-6050	-6700	-6730	-9900	-3750	-1450	-3800							
					-2800	-2850	-2830	-3850	-3100	-2500	-2670	-2700	-3800	680	1300	-680							
					-47	-19	-25	-28	-260	-50	-49	-8	26										
					(10.4)	(10.4)	(10.4)	(14.4)	(15.2)	(15.2)	(15.2)	(15.2)	(15.2)	(14.4)	(14.4)	(15.2)	(15.2)	(15.2)	(15.2)	(15.2)	(15.2)		
DHS2	Nonlinear material DYNAMIC	Drucker-Prager	Same as SHS2	No (44)	-6.93	-7.03	-7.03	-4.46	-4.38	-4.37	-4.37	-4.43	-620	-22000	-620								
					-7050	-7050	-7000	-8550	-5000	-6300	-6800	-6730	-8260	-7000	-1300	-7000							
					-4360	-4370	-4350	-5440	-4100	-3700	-4130	-4130	-5250	654	1000	-630							
					-50	-15	-16	-18	-190	1.0	-40	-28	20										
					(10.4)	(10.4)	(10.4)	(14.4)	(15.2)	(15.2)	(15.2)	(15.2)	(15.2)	(10.4)	(10.4)	(16.0)	(16.0)	(16.0)	(16.0)	(16.0)	(16.0)		

Stresses (psi)

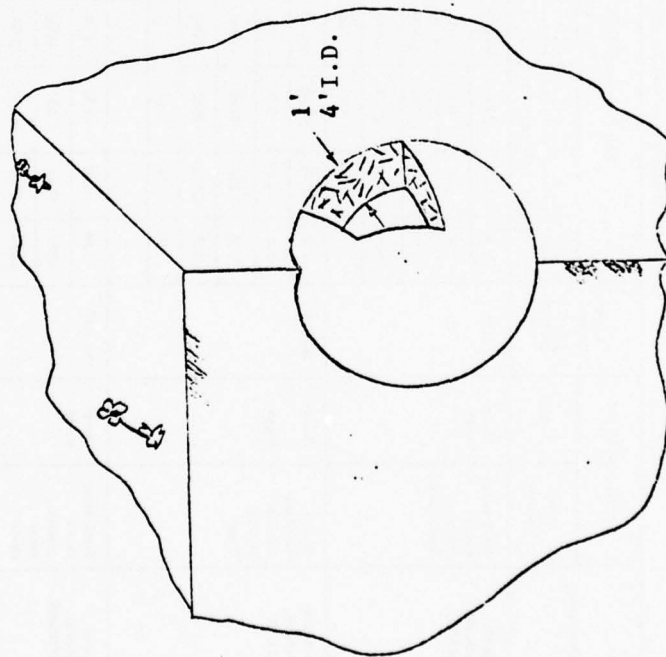
(t*) = Time of peak stress

Table 11. Results for Composite Built-Up Liner (Mesh 5.0) - Static at Full Load; Dynamic at Peak

Prob. ID	Description	Material Model For		Large Determ. (# of Steps)	Tuff Response: $\delta_v, \delta_H, \sigma_x, \sigma_y, \sigma_z, \tau_{xy}, \tau_{yz}, \tau_{zx}$ - Static - Dynamic												Order of Columns						Steel Liner Response: $\sigma_x, \sigma_y, \sigma_z, \tau_{xy}, \tau_{yz}, \tau_{zx}$ - (t*)						Concrete Liner Response: $\sigma_x, \sigma_y, \sigma_z, \tau_{xy}, \tau_{yz}, \tau_{zx}$ - (t*)																																																																																																																																																																																																																																																																																																																																																																																																																																																																																																																																																																																																																																																																																																																																																																																																																																																																																																																																																																																																																																																																																																																																																																																																																																																																																																																																																																																																																																																																																																																																																																																																																																																																																																																																																																																																																																																																																																																																																																																																																																														
		Steel/Concrete	Tuff		A	B	C	D	E	F	G	H	I	J	K	L	M	N	O	P	Q	R	S	T	U	V	W	X	Y	Z	AA	AB	AC	AD	AE	AF	AG	AH	AI	AJ	AK	AL	AM	AN	AO	AP	AQ	AR	AS	AT	AU	AV	AW	AX	AY	AZ	BA	BB	BC	BD	BE	BF	BG	BH	BI	BJ	BK	BL	BM	BN	BO	BP	BQ	BR	BS	BT	BU	BV	BW	BX	BY	BZ	CA	CB	CC	CD	CE	CF	CG	CH	CI	CJ	CK	CL	CM	CN	CO	CP	CQ	CR	CS	CT	CU	CV	CW	CX	CY	CZ	DA	DB	DC	DD	DE	DF	DG	DH	DI	DJ	DK	DL	DM	DN	DO	DP	DQ	DR	DS	DT	DU	DV	DW	DX	DY	DZ	EA	EB	EC	ED	EE	EF	EG	EH	EI	EJ	EK	EL	EM	EN	EO	EP	EQ	ER	ES	ET	EU	EV	EW	EX	EY	EZ	FA	FB	FC	FD	FE	FF	FG	FH	FI	FJ	FK	FL	FM	FN	FO	FP	FQ	FR	FS	FT	FU	FV	FW	FX	FY	FZ	GA	GB	GC	GD	GE	GF	GG	GH	GI	GJ	GK	GL	GM	GN	GO	GP	GQ	GR	GS	GT	GU	GV	GW	GX	GY	GZ	HA	HB	HC	HD	HE	HF	HG	HH	HI	HJ	HK	HL	HM	HN	HO	HP	HQ	HR	HS	HT	HU	HV	HW	HX	HY	HZ	IA	IB	IC	ID	IE	IF	IG	IH	II	IJ	IK	IL	IM	IN	IO	IP	IQ	IR	IS	IT	IU	IV	IW	IX	IY	IZ	JA	JB	JC	JD	JE	JF	JG	JH	JI	IJ	JK	KL	LM	LN	LO	LP	LQ	LR	LS	LT	LU	LV	LW	LX	LY	LZ	MA	MB	MC	MD	ME	MF	MG	MH	MI	MJ	MK	ML	MM	MN	MO	MP	MQ	MR	MS	MT	MU	MV	MW	MX	MY	MZ	NA	NB	NC	ND	NE	NF	NG	NH	NI	NJ	NK	NL	NM	NN	NO	NP	NQ	NR	NS	NT	NU	NV	NW	NX	NY	NZ	OA	OB	OC	OD	OE	OF	OG	OH	OI	OJ	OK	OL	OM	ON	OO	OP	OQ	OR	OS	OT	OU	OV	OW	OX	OY	OZ	PA	PB	PC	PD	PE	PF	PG	PH	PI	PJ	PK	PL	PM	PN	PO	PP	PQ	PR	PS	PT	PU	PV	PW	PX	PY	PZ	QA	QB	QC	QD	QE	QF	QG	QH	QI	QJ	QK	QL	QM	QN	QO	QP	QQ	QR	QS	QT	QU	QV	QW	QX	QY	QZ	RA	RB	RC	RD	RE	RF	RG	RH	RI	RJ	RK	RL	RM	RN	RO	RP	RQ	RR	RS	RT	RU	RV	RW	RX	RY	RZ	SA	SB	SC	SD	SE	SF	SG	SH	SI	SJ	SK	SL	SM	SN	SO	SP	SQ	SR	SS	ST	SU	SV	SW	SX	SY	SZ	TA	TB	TC	TD	TE	TF	TG	TH	TI	TJ	TK	TL	TM	TN	TO	TP	TQ	TR	TS	TT	TU	TV	TW	TX	TY	TZ	UA	UB	UC	UD	UE	UF	UG	UH	UI	UJ	UK	UL	UM	UN	UO	UP	UQ	UR	US	UT	UU	UV	UW	UX	UY	UZ	VA	VB	VC	VD	VE	VF	VG	VH	VI	VJ	VK	VL	VM	VN	VO	VP	VQ	VR	VS	VT	VU	VV	VW	VX	VY	VZ	WA	WB	WC	WD	WE	WF	WG	WH	WI	WJ	WK	WL	WM	WN	WO	WP	WQ	WR	WS	WT	WU	WV	WW	WX	WY	WZ	XA	XB	XC	XD	XE	XF	XG	XH	XI	XJ	XK	XL	XM	XN	XO	XP	XQ	XR	XS	XT	XU	XV	XW	XX	XY	XZ	YA	YB	YC	YD	YE	YF	YG	YH	YI	YJ	YK	YL	YM	YN	YO	YP	YQ	YR	YS	YT	YU	YV	YW	YX	YY	YZ	ZA	ZB	ZC	ZD	ZE	ZF	ZG	ZH	ZI	ZJ	ZK	ZL	ZM	ZN	ZO	ZP	ZQ	ZR	ZS	ZT	ZU	ZV	ZW	ZX	ZY	ZZ	AA	AB	AC	AD	AE	AF	AG	AH	AI	AJ	AK	AL	AM	AN	AO	AP	AQ	AR	AS	AT	AU	AV	AW	AX	AY	AZ	BA	BB	BC	BD	BE	BF	BG	BH	BI	BJ	BK	BL	BM	BN	BO	BP	BQ	BR	BS	BT	BU	BV	BW	BX	BY	BZ	CA	CB	CC	CD	CE	CF	CG	CH	CI	CJ	CK	CL	CM	CN	CO	CP	CQ	CR	CS	CT	CU	CV	CW	CX	CY	CZ	DA	DB	DC	DD	DE	DF	DG	DH	DI	DJ	DK	DL	DM	DN	DO	DP	DQ	DR	DS	DT	DU	DV	DW	DX	DY	DZ	EA	EB	EC	ED	EE	EF	EG	EH	EI	EJ	EK	EL	EM	EN	EO	EP	EQ	ER	ES	ET	EU	EV	EW	EX	EY	EZ	FA	FB	FC	FD	FE	FF	FG	FH	FI	FJ	FK	FL	FM	FN	FO	FP	FQ	FR	FS	FT	FU	FV	FW	FX	FY	FZ	GA	GB	GC	GD	GE	GF	GG	GH	GI	GJ	GK	GL	GM	GN	GO	GP	GQ	GR	GS	GT	GU	GV	GW	GX	GY	GZ	HA	HB	HC	HD	HE	HF	HG	HH	HI	HJ	HK	HL	HM	HN	HO	HP	HQ	HR	HS	HT	HU	HV	HW	HX	HY	HZ	IA	IB	IC	ID	IE	IF	IG	IH	II	IJ	IK	IL	IM	IN	IO	IP	IQ	IR	IS	IT	IU	IV	IW	IX	IY	IZ	JA	JB	JC	JD	JE	JF	JG	JH	JI	IJ	JK	KL	LM	LN	LO	LP	LQ	LR	LS	LT	LU	LV	LW	LX	LY	LZ	MA	MB	MC	MD	ME	MF	MG	MH	MI	MJ	MK	ML	MM	MN	MO	MP	MQ	MR	MS	MT	MU	MV	MW	MX	MY	MZ	NA	NB	NC	ND	NE	NF	NG	NH	NI	NJ	NK	NL	NM	NN	NO	NP	NQ	NR	NS	NT	NU	NV	NW	NX	NY	NZ	OA	OB	OC	OD	OE	OF	OG	OH	OI	OJ	OK	OL	OM	ON	OO	OP	OQ	OR	OS	OT	OU	OV	OW	OX	OY	OZ	PA	PB	PC	PD	PE	PF	PG	PH	PI	PJ	PK	PL	PM	PN	PO	PP	PQ	PR	PS	PT	PU	PV	PW	PX	PY	PZ	QA	QB	QC	QD	QE	QF	QG	QH	QI	QJ	QK	QL	QM	QN	QO	QP	QQ	QR	QS	QT	QU	QV	QW	QX	QY	QZ	RA	RB	RC	RD	RE	RF	RG	RH	RI	RJ	RK	RL	RM	RN	RO	RP	RQ	RR	RS	RT	RU	RV	RW	RX	RY	RZ	SA	SB	SC	SD	SE	SF	SG	SH	SI	SJ	SK	SL	SM	SN	SO	SP	SQ	SR	SS	ST	SU	SV	SW	SX	SY	SZ	TA	TB	TC	TD	TE	TF	TG	TH	TI	TJ	TK	TL	TM	TN	TO	TP	TQ	TR	TS	TT	TU	TV	TW	TX	TY	TZ	UA	UB	UC	UD	UE	UF	UG	UH	UI	UJ	UK	UL	UM	UN	UO	UP	UQ	UR	US	UT	UU	UV	UW	UX	UY	UZ	VA	VB	VC	VD	VE	VF	VG	VH	VI	VJ	VK	VL	VM	VN	VO	VP	VQ	VR	VS	VT	VU	VV	VW	VX	VY	VZ	WA	WB	WC	WD	WE	WF	WG	WH	WI	WJ	WK	WL	WM	WN	WO	WP	WQ	WR	WS	WT	WU	WV	WW	WX	WY	WZ	XA	XB	XC	XD	XE	XF	XG	XH	XI	XJ	XK	XL	XM	XN	XO	XP	XQ	XR	XS	XT	XU	XV	XW	XX	XY	XZ	YA	YB	YC	YD	YE	YF	YG	YH	YI	YJ	YK	YL	YM	YN	YO	YP	YQ	YR	YS	YT	YU	YV	YW	YX	YY	YZ	ZA	ZB	ZC	ZD	ZE	ZF	ZG	ZH	ZI	ZJ	ZK	ZL	ZM	ZN	ZO	ZP	ZQ	ZR	ZS	ZT	ZU	ZV	ZW	ZX	ZY	ZZ	AA	AB	AC	AD	AE	AF	AG	AH	AI	AJ	AK	AL	AM	AN	AO	AP	AQ	AR	AS	AT	AU	AV	AW	AX	AY	AZ	BA	BB	BC	BD	BE	BF	BG	BH	BI	BJ	BK	BL	BM	BN	BO	BP	BQ	BR	BS	BT	BU	BV	BW	BX	BY	BZ	CA	CB	CC	CD	CE	CF	CG	CH	CI	CJ	CK	CL	CM	CN	CO	CP	CQ	CR	CS	CT	CU	CV	CW	CX	CY	CZ	DA	DB	DC	DD	DE	DF	DG	DH	DI	DJ	DK	DL	DM	DN	DO	DP	DQ	DR	DS	DT	DU	DV	DW	DX	DY	DZ	EA	EB	EC	ED	EE	EF	EG	EH	EI	EJ	EK	EL	EM	EN	EO	EP	EQ	ER	ES	ET	EU	EV	EW	EX	EY	EZ	FA	FB	FC	FD	FE	FF	FG	FH	FI	FJ	FK	FL	FM	FN	FO	FP	FQ	FR	FS	FT	FU	FV	FW	FX	FY	FZ	GA	GB	GC	GD	GE	GF	GG	GH	GI	GJ	GK	GL	GM	GN	GO	GP	GQ	GR	GS	GT	GU	GV	GW	GX	GY	GZ	HA	HB	HC	HD	HE	HF	HG	HH	HI	HJ	HK	HL	HM	HN	HO	HP	HQ	HR	HS	HT	HU	HV	HW	HX	HY	HZ	IA	IB	IC	ID	IE	IF	IG	IH	II	IJ	IK	IL	IM	IN	IO	IP	IQ	IR	IS	IT	IU	IV	IW	IX	IY	IZ	JA	JB	JC	JD	JE	JF	JG	JH	JI	IJ	JK	KL	LM	LN	LO	LP	LQ	LR	LS	LT	LU	LV	LW	LX	LY	LZ	MA	MB	MC	MD	ME	MF	MG	MH	MI	MJ	MK	ML	MM	MN	MO	MP	MQ	MR	MS	MT	MU	MV	MW	MX	MY	MZ	NA	NB	NC	ND	NE	NF	NG	NH	NI	NJ	NK	NL	NM	NN	NO	NP	NQ	NR	NS	NT	NU	NV	NW	NX	NY	NZ	OA	OB	OC	OD	OE	OF	OG	OH	OI	OJ	OK	OL	OM	ON	OO	OP	OQ	OR	OS	OT	OU	OV	OW	OX	OY	OZ	PA	PB	PC	PD	PE	PF	PG	PH	PI	PJ	PK	PL	PM	PN	PO	PP	PQ	PR	PS	PT	PU	PV	PW	PX	PY	PZ	QA	QB	QC	QD	QE	QF	QG	QH	QI	QJ	QK	QL	QM	QN	QO	QP	QQ	QR	QS	QT	QU	QV	QW	QX	QY	QZ	RA	RB	RC	RD	RE	RF	RG	RH	RI	RJ	RK	RL	RM	RN	RO	RP	RQ	RR	RS	RT	RU	RV	RW	RX	RY	RZ	SA	SB	SC	SD	SE	SF	SG	SH	SI	SJ	SK	SL	SM	SN	SO	SP	SQ	SR	SS	ST	SU	SV	SW	SX	SY	SZ	TA	TB	TC	TD	TE	TF	TG	TH	TI	TJ	TK	TL	TM	TN	TO	TP	TQ	TR	TS	TT	TU	TV	TW	TX	TY	TZ	UA	UB	UC	UD	UE	UF	UG	UH	UI	UJ	UK	UL	UM	UN	UO	UP	UQ	UR	US	UT	UU	UV	UW	UX	UY	UZ	VA	VB	VC	VD	VE	VF	VG	VH	VI	VJ	VK	VL	VM	VN	VO	VP	VQ	VR	VS	VT	VU	VV	VW	VX	VY	VZ	WA	WB	WC	WD	WE	WF	WG	WH	WI	WJ	WK	WL	WM	WN	WO	WP	WQ	WR	WS	WT	WU	WV	WW	WX	WY	WZ	XA	XB	XC	XD	XE	XF	XG	XH	XI	XJ	XK	XL	XM	XN	XO	XP	XQ	XR	XS	XT	XU	XV	XW	XX	XY	XZ	YA	YB	YC	YD	YE	YF	YG	YH	YI	YJ	YK	YL	YM	YN	YO	YP	YQ	YR	YS	YT	YU	YV	YW	YX	YY	YZ	ZA	ZB	ZC	ZD	ZE	ZF	ZG	ZH	ZI	ZJ	ZK	ZL	ZM	ZN	ZO	ZP	ZQ	ZR	ZS	ZT	ZU	ZV	ZW	ZX	ZY	ZZ	AA	AB	AC	AD	AE	AF	AG	AH	AI	AJ	AK	AL	AM	AN	AO	AP	AQ	AR	AS	AT	AU	AV	AW	AX	AY	AZ	BA	BB	BC	BD	BE	BF	BG	BH	BI	BJ	BK	BL	BM	BN	BO	BP	BQ	BR	BS	BT	BU	BV	BW	BX	BY	BZ	CA	CB	CC	CD	CE	CF	CG	CH	CI	CJ	CK	CL	CM	CN	CO	CP	CQ	CR	CS	CT	CU	CV	CW	CX	CY	CZ	DA	DB	DC	DD	DE	DF	DG	DH	DI	DJ	DK	DL	DM	DN	DO

HOMOGENEOUS LINING

- Idealized as axisymmetric solid
- Constructed of fibrous reinforced concrete



COMPOSITE BUILT-UP LINING

- Idealized as plane strain slice
- Constructed of steel liner and cellular concrete

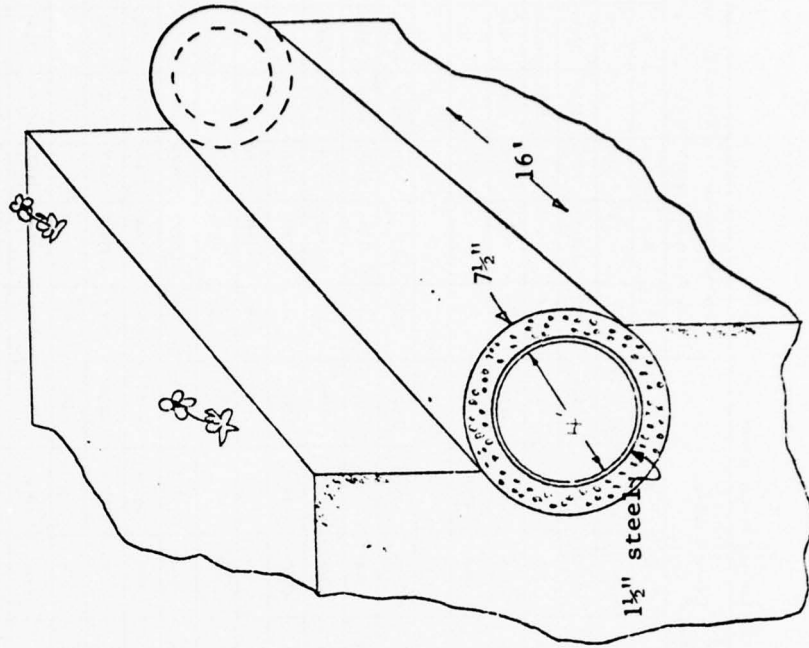
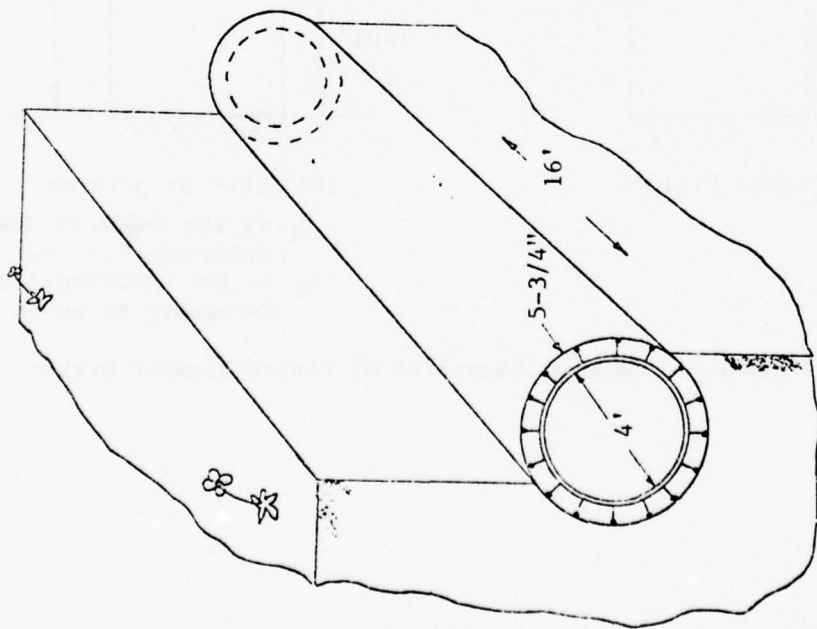
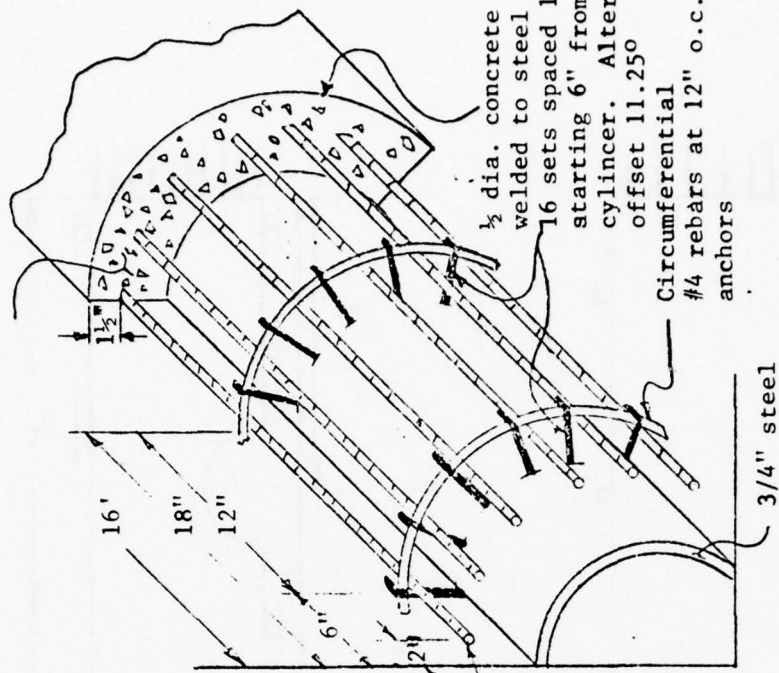


Figure 1. Homogeneous Sphere and Composite Built-up Liner

Idealized as plane strain slice
 Constructed of steel liner and
 reinforced concrete



concrete 5" thick



16 longitudinal
 #4 rebar,
 15'8" long,
 2" from end of
 concrete

1/2 dia. concrete anchors
 welded to steel plate,
 16 sets spaced 12' apart
 starting 6" from end of
 cylinder. Alternate sets
 offset 11.25°

Circumferential
 #4 rebar at 12" o.c. wired to
 anchors

3/4" steel

Figure 2. Composite Integral Liner

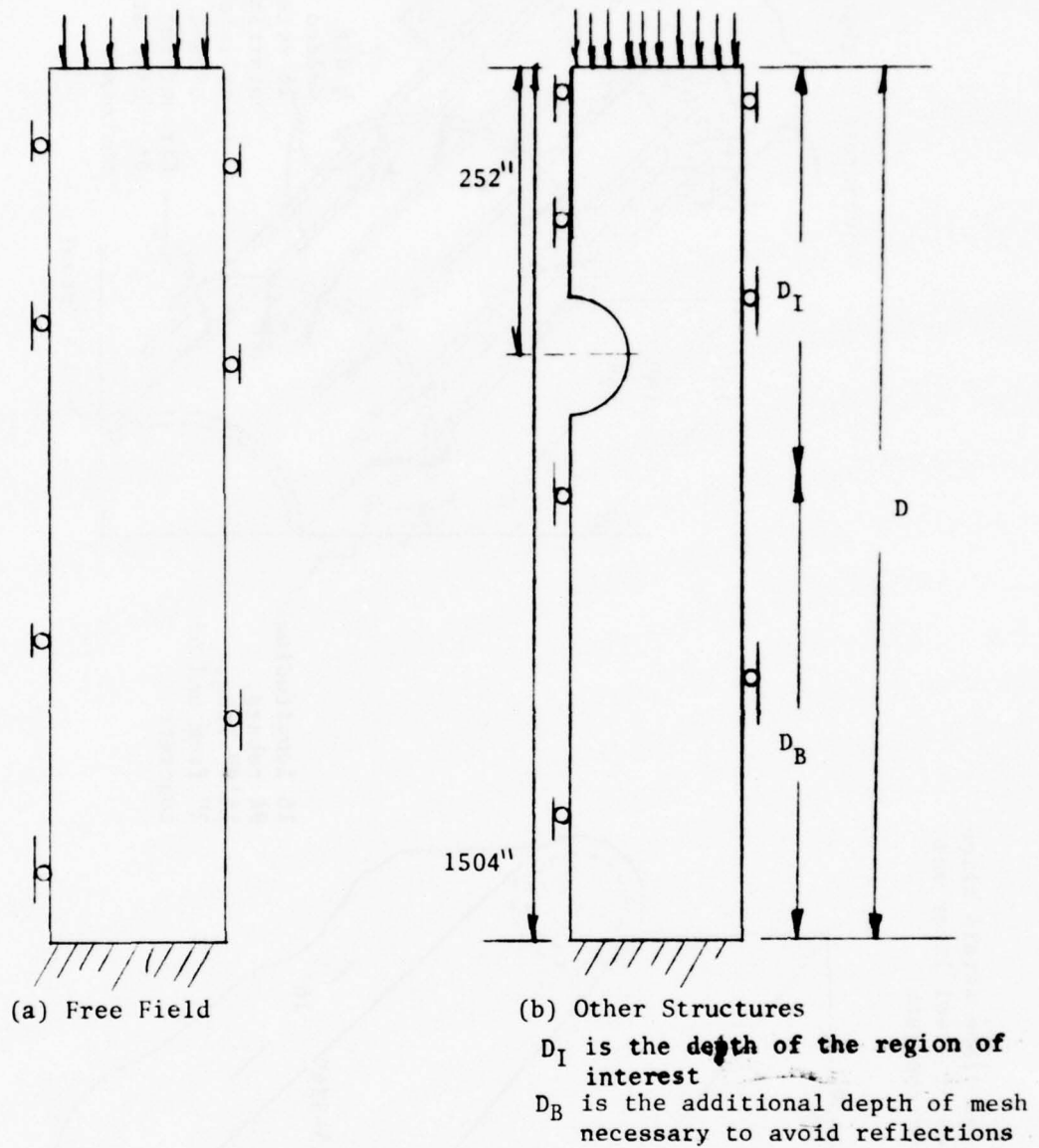


Figure 3. General Character of Finite Element Meshes

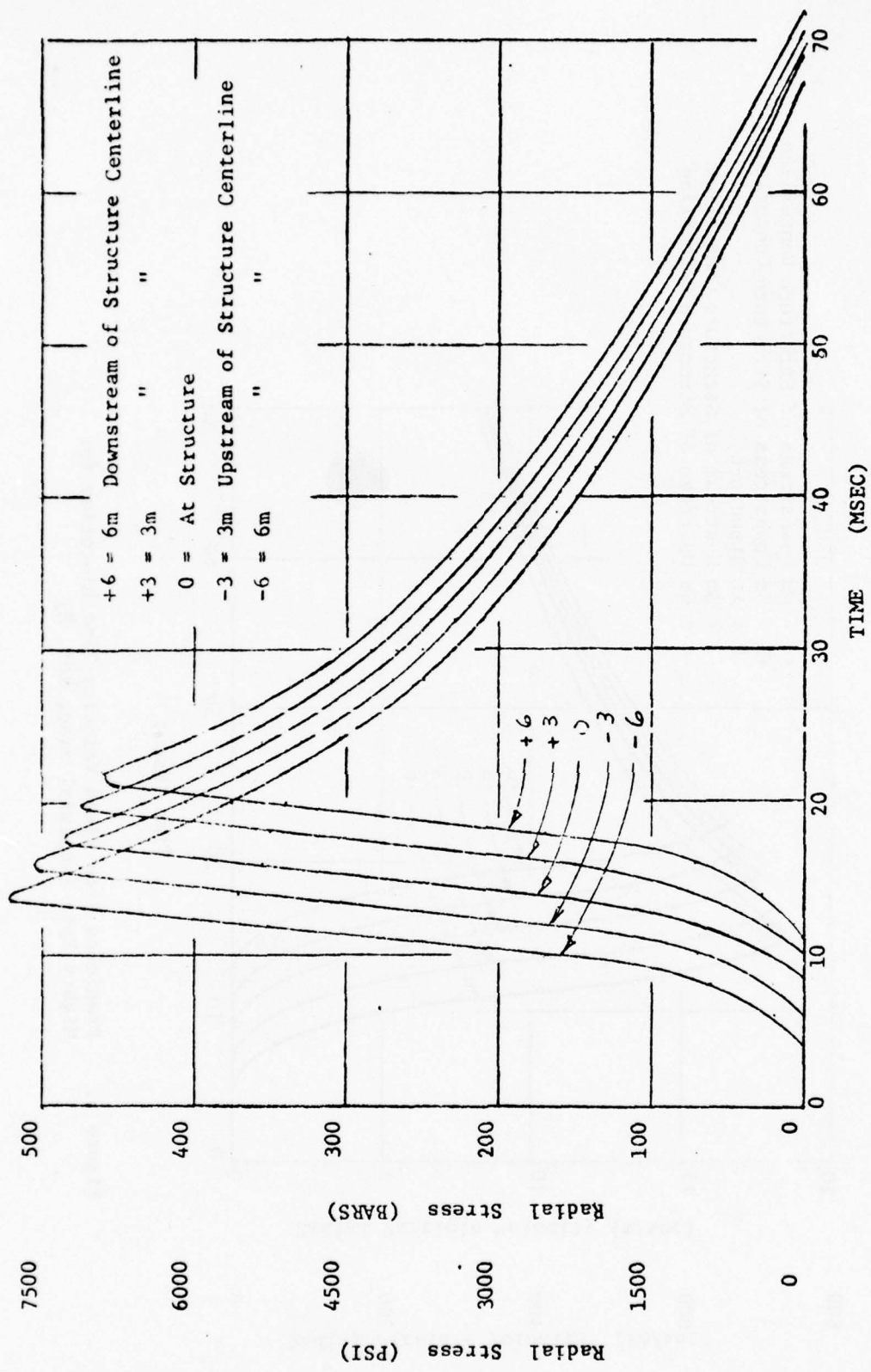


Figure 4. Predicted Free Field Radial Stress Time Histories for Mighty Epic (Uniaxial Case, Ref. 3)

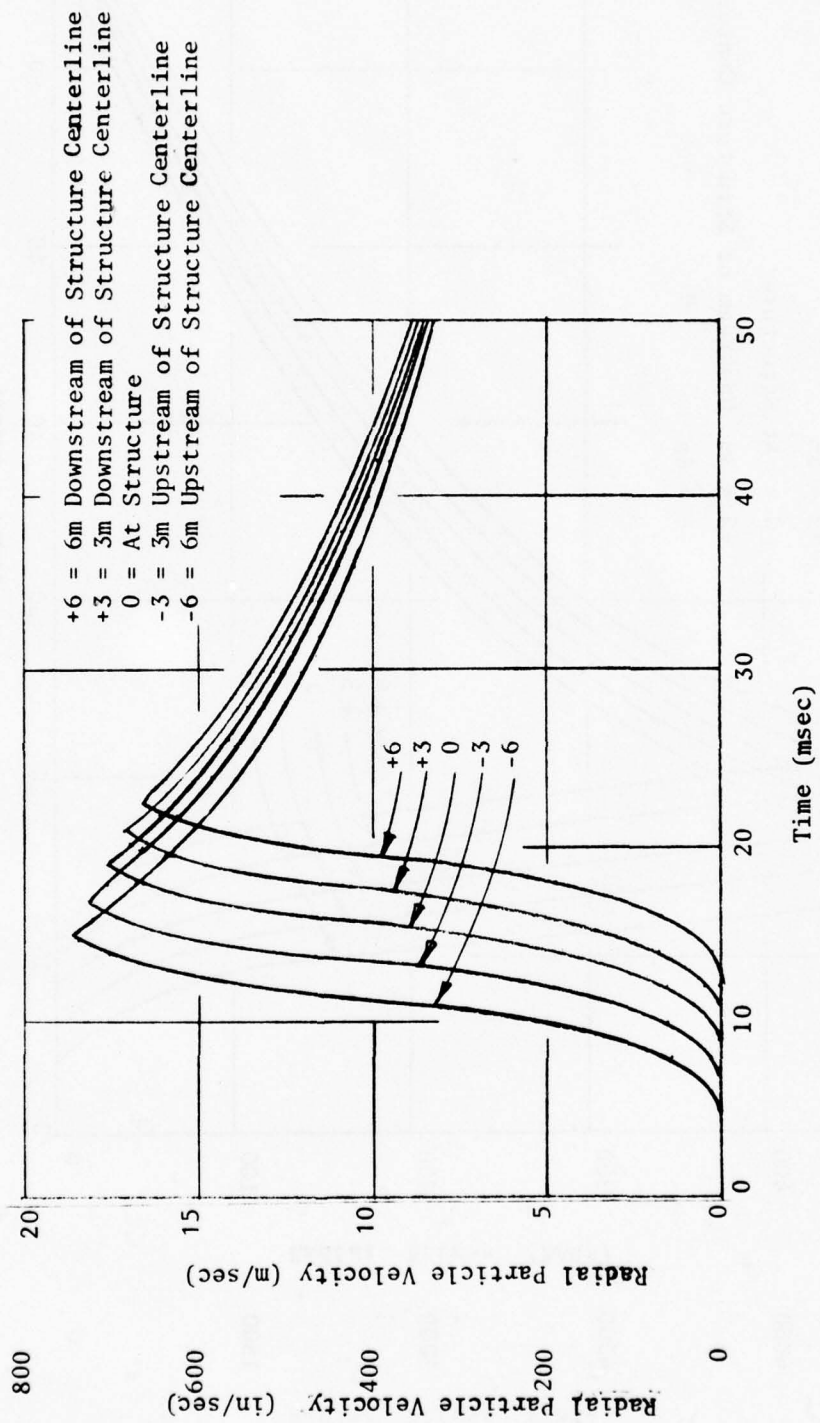
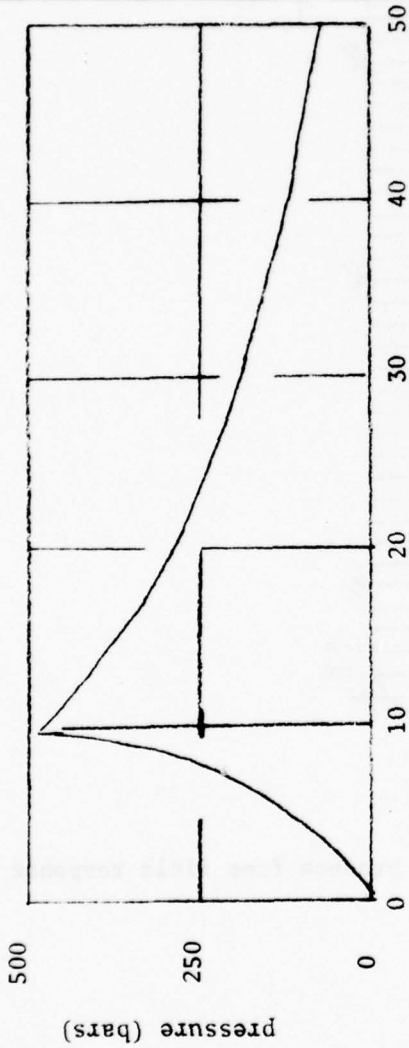
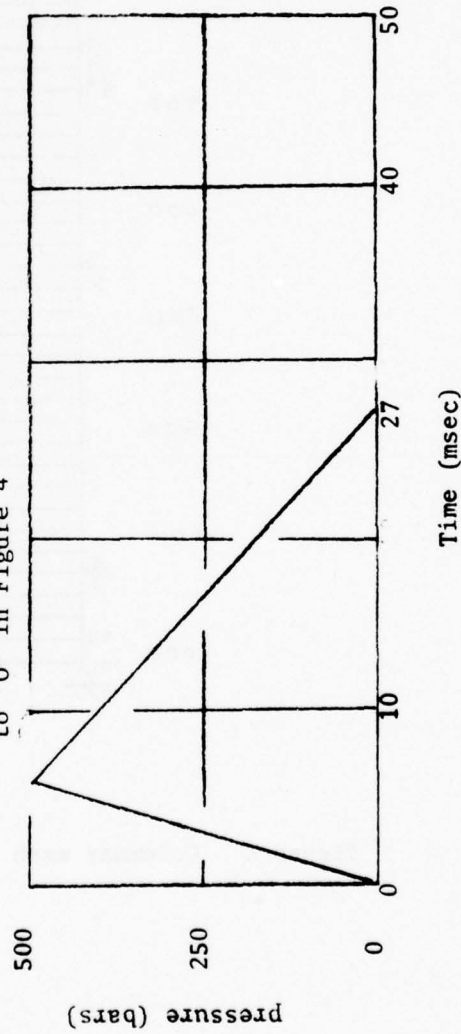


Figure 5. Predicted Free Field Velocity Time Histories for Mighty Epic (uniaxial case, Ref. 3)



(a) Wave form applied to all structures corresponds to "0" in Figure 4



(b) Idealized form of wave shown in Figure 6a

Digitized form of curves			
Time Scale for Figure 4 (sec)	Time Scale for Figure 6a (sec)	Pressure (bars)	
.008	.0	0	
.0095	.0015	10	
.0105	.0025	30	
.012	.004	70	
.01375	.00575	140	
.014	.006	180	
.0175	.0095	480	
.01775	.00975	485	
.018	.01	485	
.0215	.0135	400	
.0255	.0175	330	
.029	.021	280	
.0325	.0245	240	
.03625	.02825	205	
.04075	.03275	170	
.05	.042	115	
.055	.047	80	
.06	.052	50	
.065	.057	35	
.0695	.0615	0	

Figure 6. Forcing functions used to generate the responses for the Mighty Epic Structures

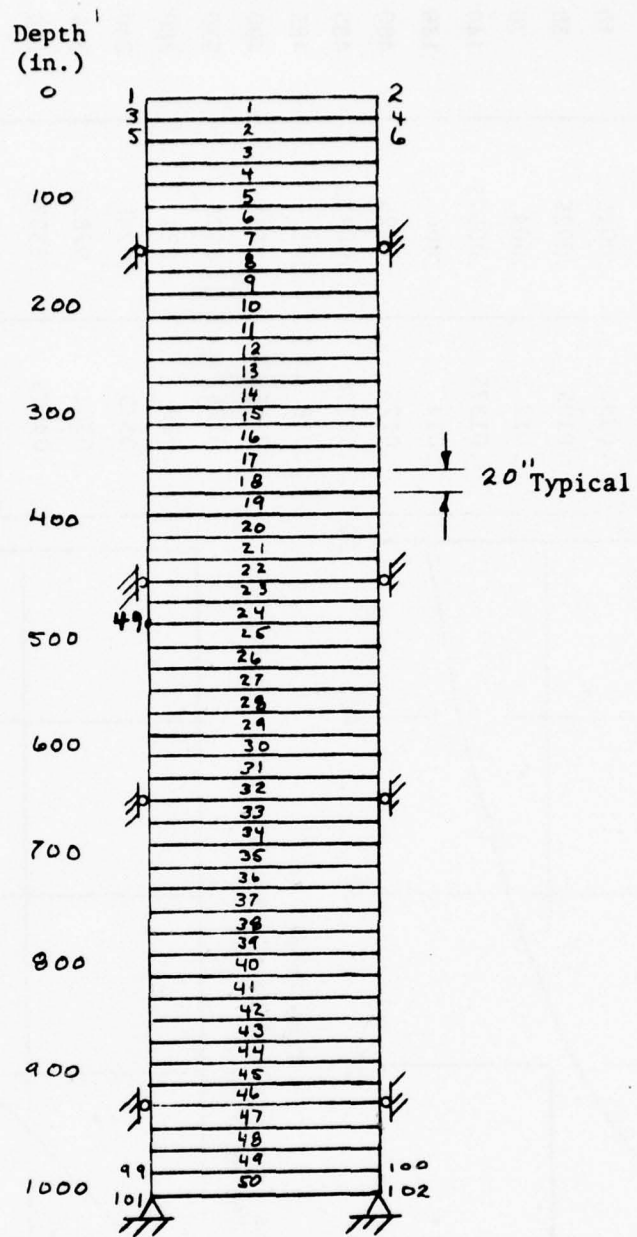


Figure 7. Columnar mesh used to produce free field response

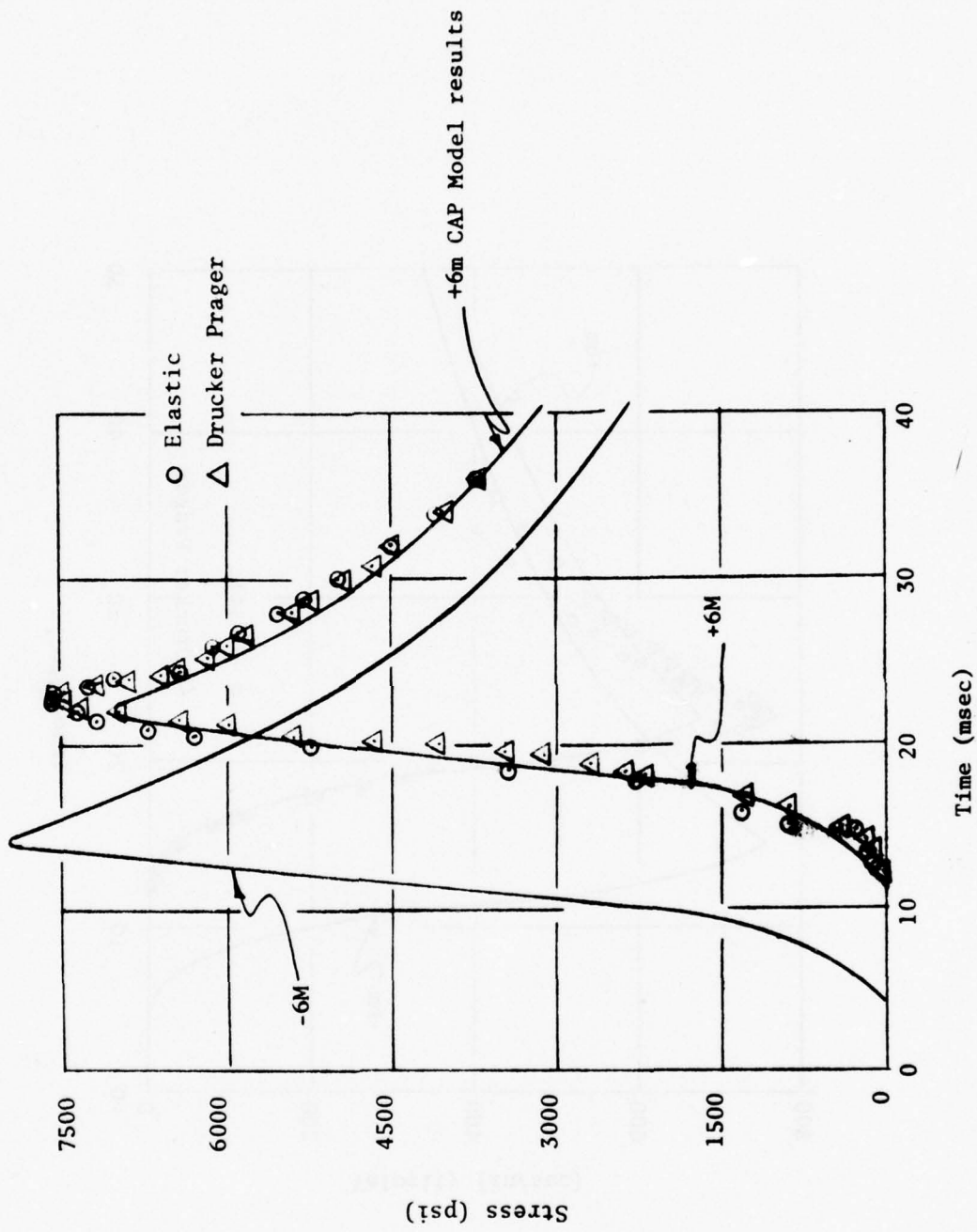


Figure 8. Free Field Response Stress vs. Time (Element 24)

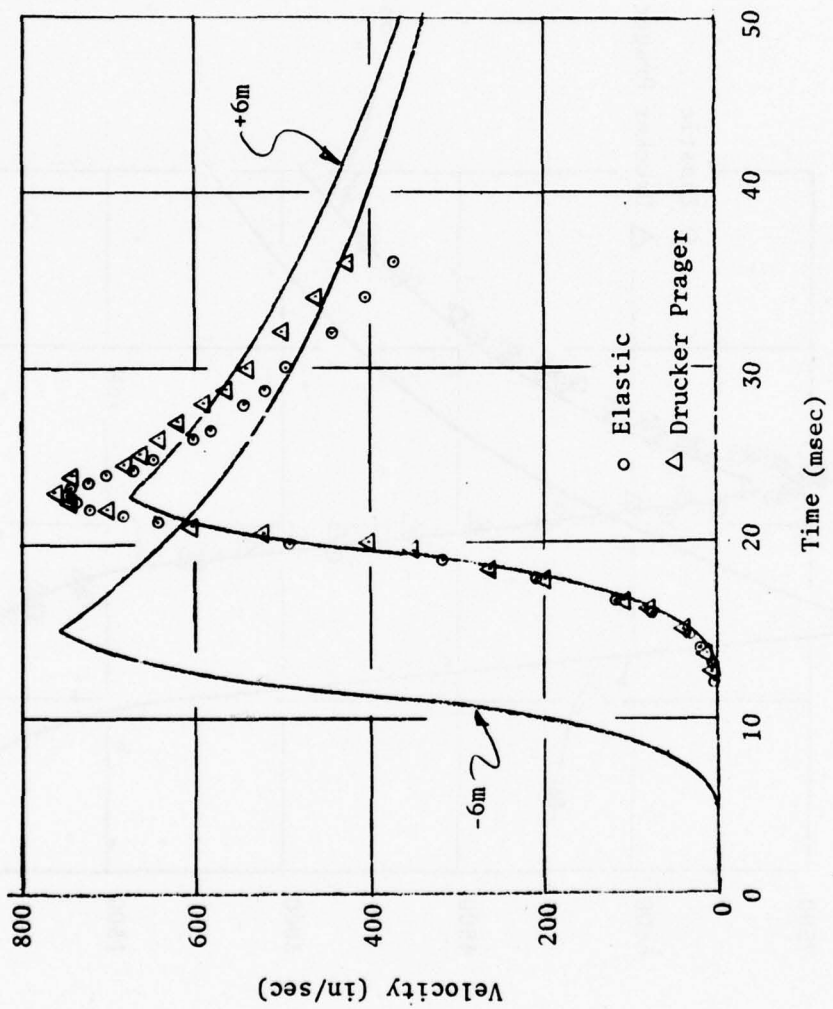
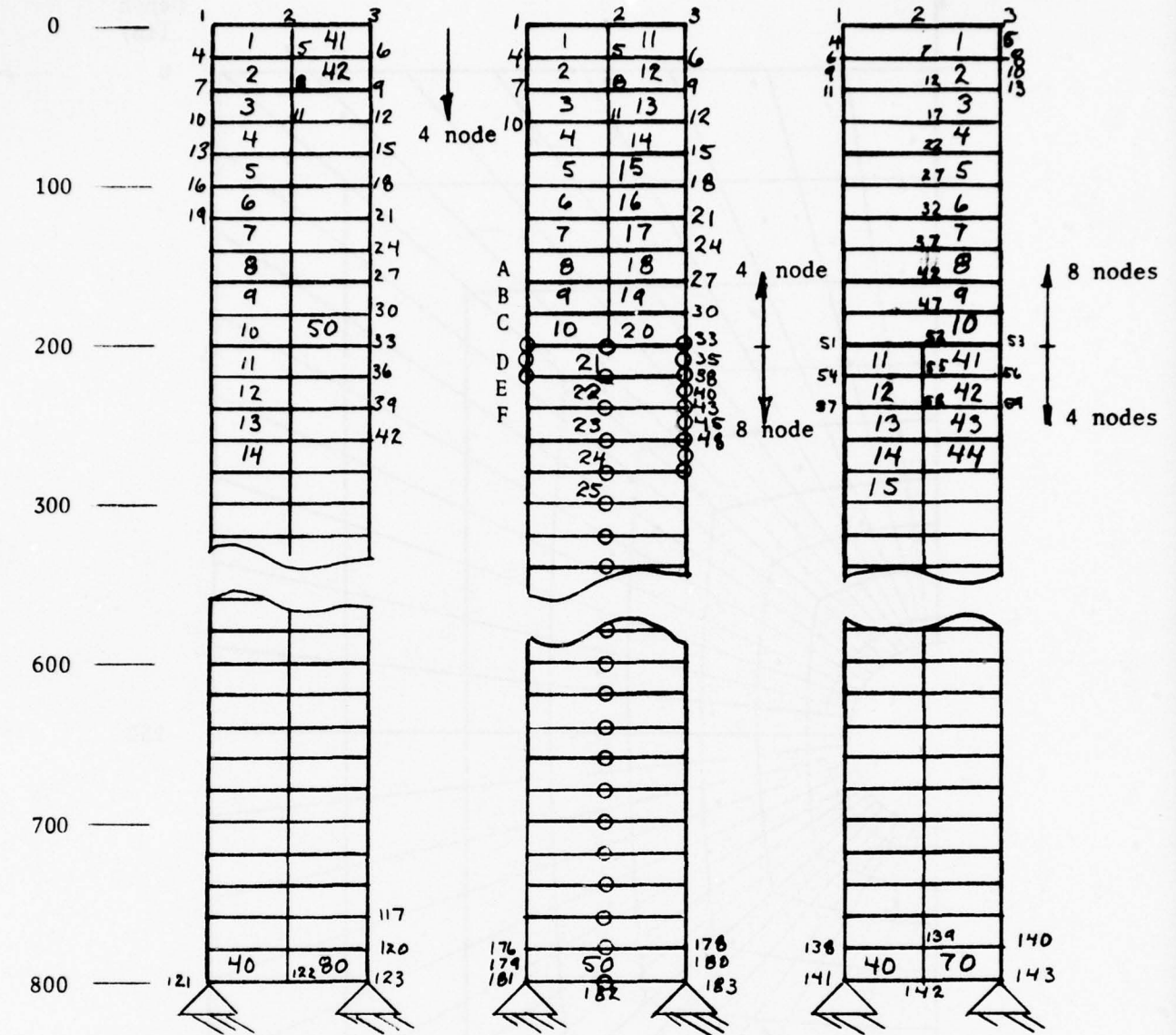


Figure 9. Free Field Response Velocity vs. Time (at node 49)

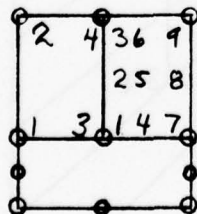
Depth (in)



(b) CASE 1, control case made of all 4 node elements

(c) CASE 2, transition of 4 node to 8 node elements

(d) CASE 3, transition of 8 node to 4 node elements

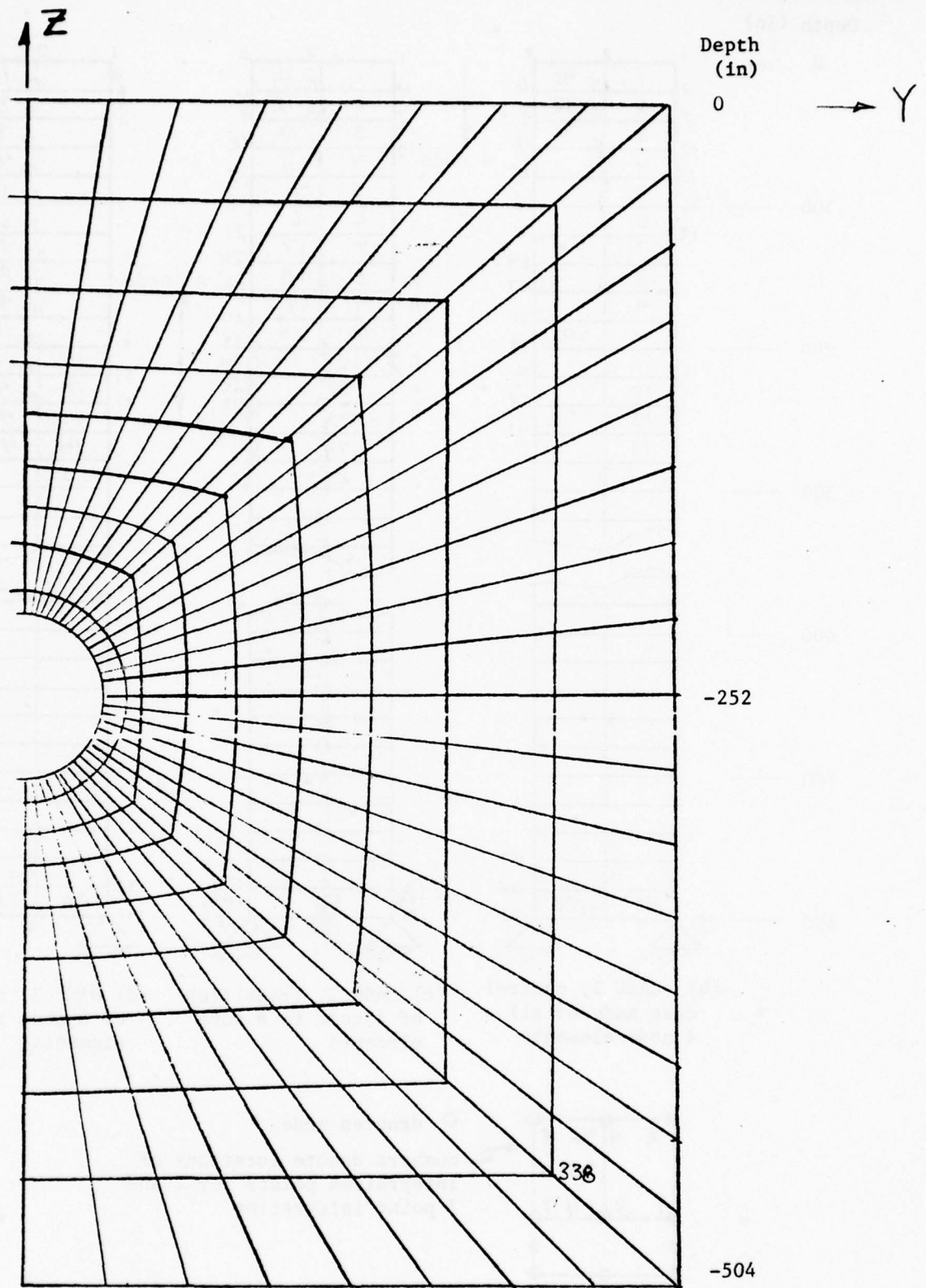


○ denotes node

numbers denote locations of integration points for 2 and 3 point integration

(a) 4 to 8 node transition

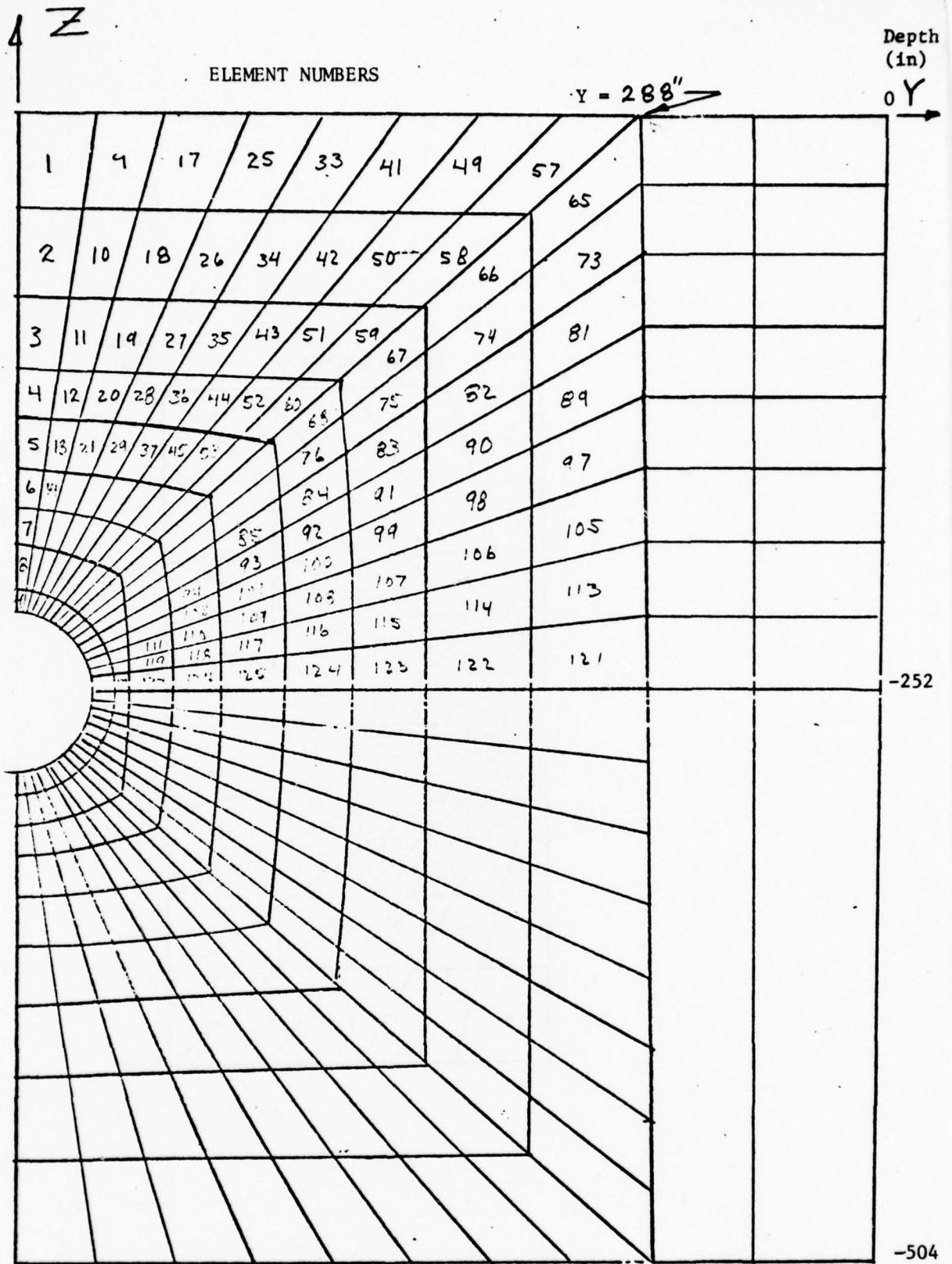
Figure 10. Meshes used to check element compatibility



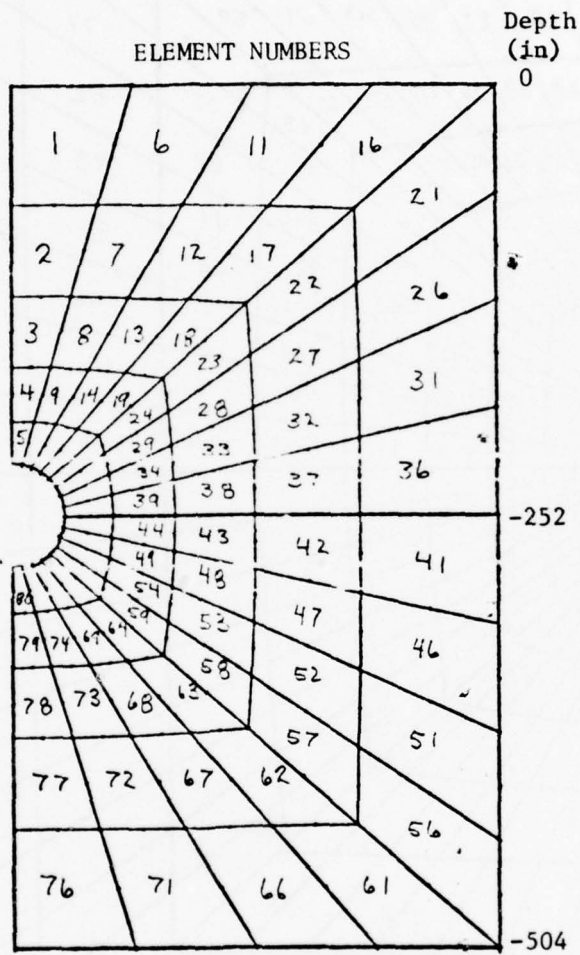
(a) Mesh 3.0

Figure 11. Meshes for Free Field with Cylindrical Cavity

(Note: thin cylindrical cavity liner too small to be seen on figures)



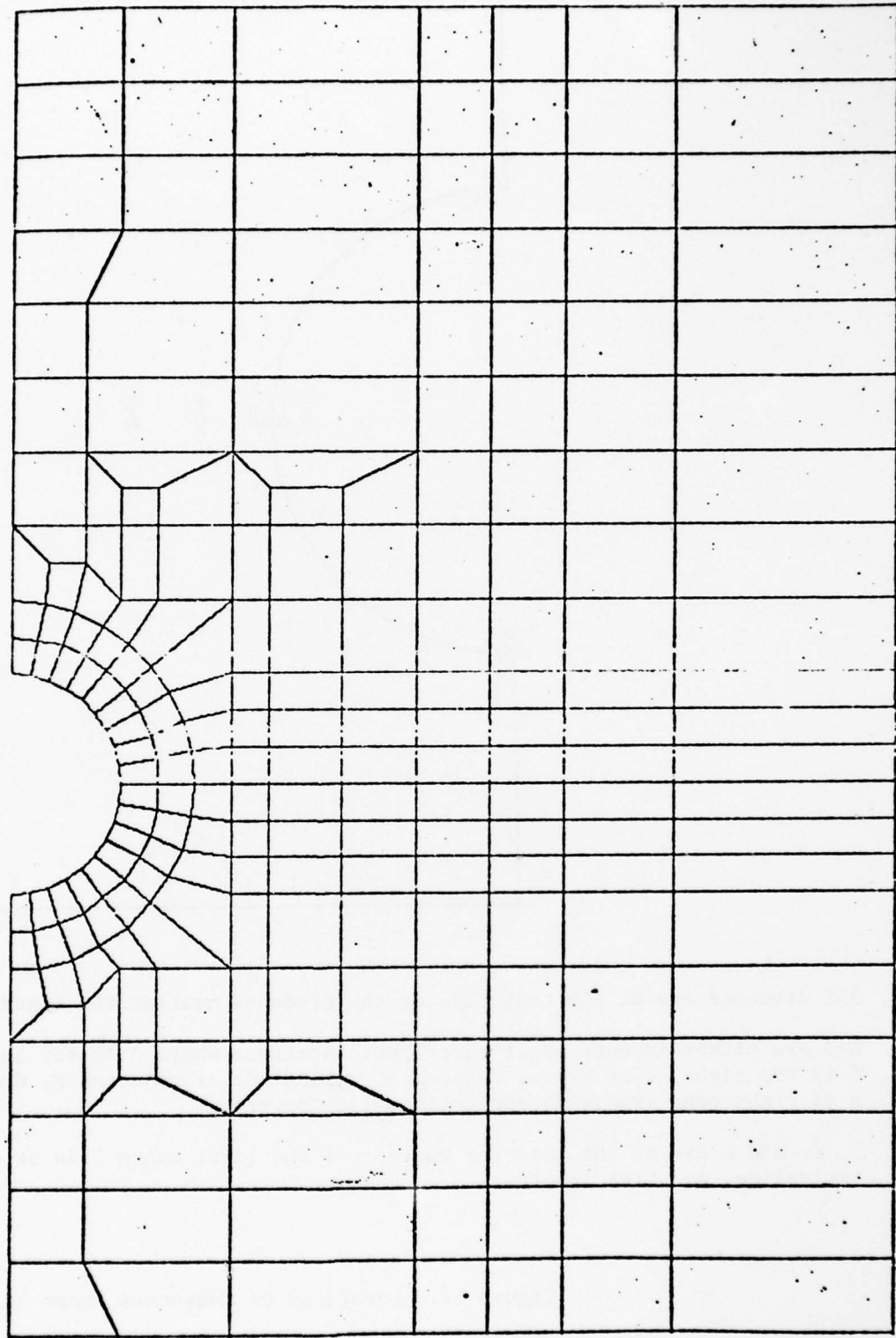
(b) Mesh 3.1



(c) Mesh 3.2

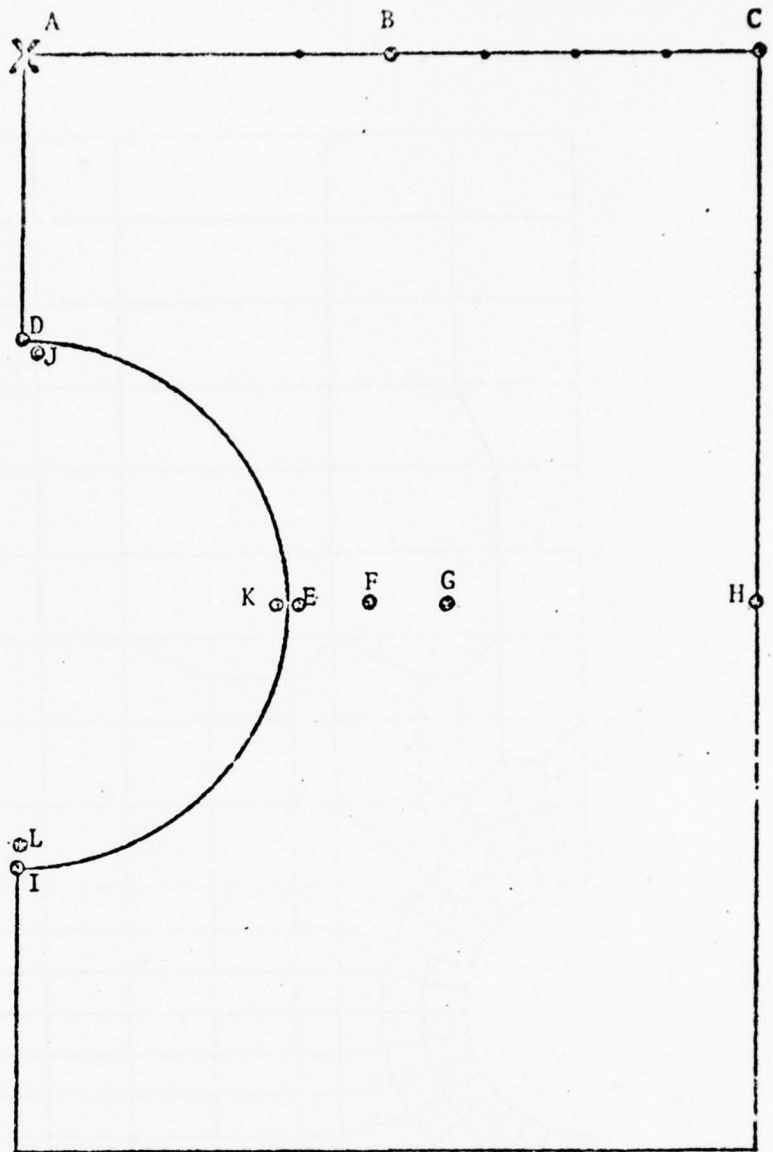
Depth
(in)

0



-252

(d) Mesh 3.3



1. All stresses are at the centroids of the elements nearest the locations shown.
2. A-I are either in tuff or at tuff/liner interface where A is top left, B top mid, C is top right, D at crown, E adjacent springline, F adjacent E, G at mid mesh, H at right edge even with springline, I at invert.
3. J, K, and L are at the interior surface of the liner where J is at crown, K at springline, and L at invert.

Figure 12. Locations of Responses shown in Tables 2-12

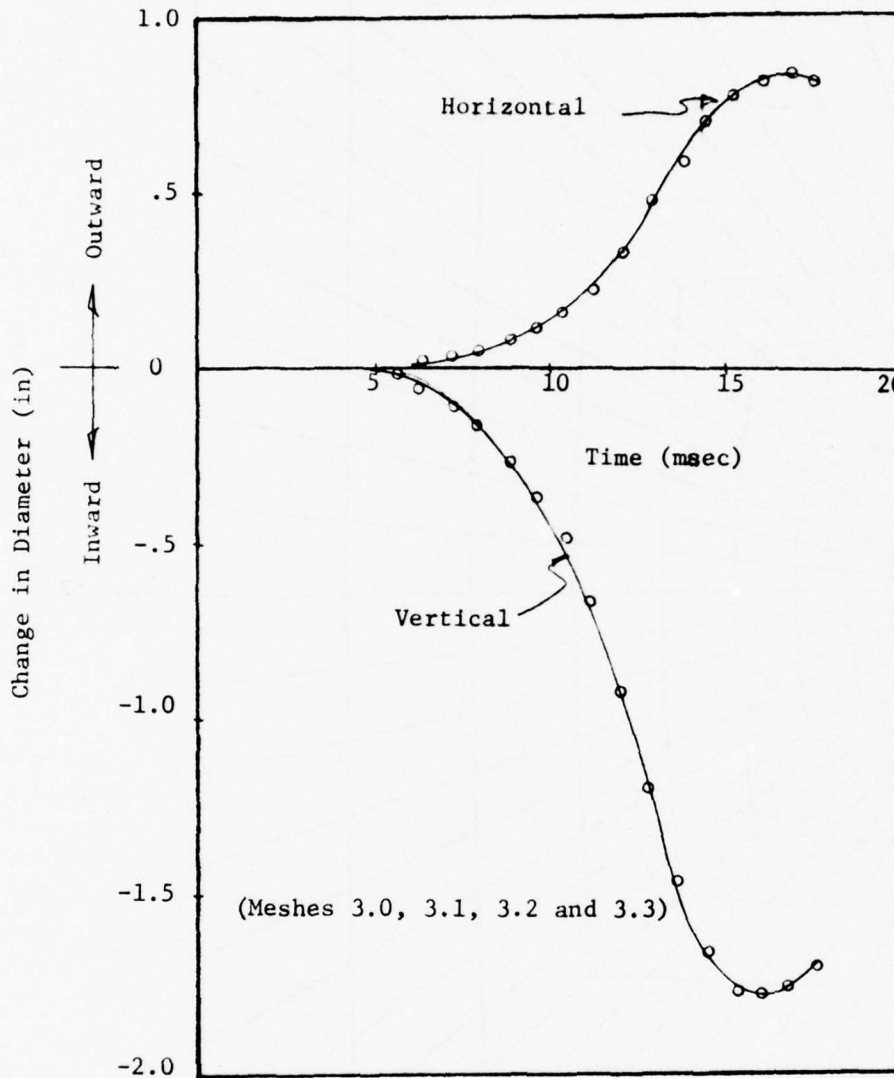
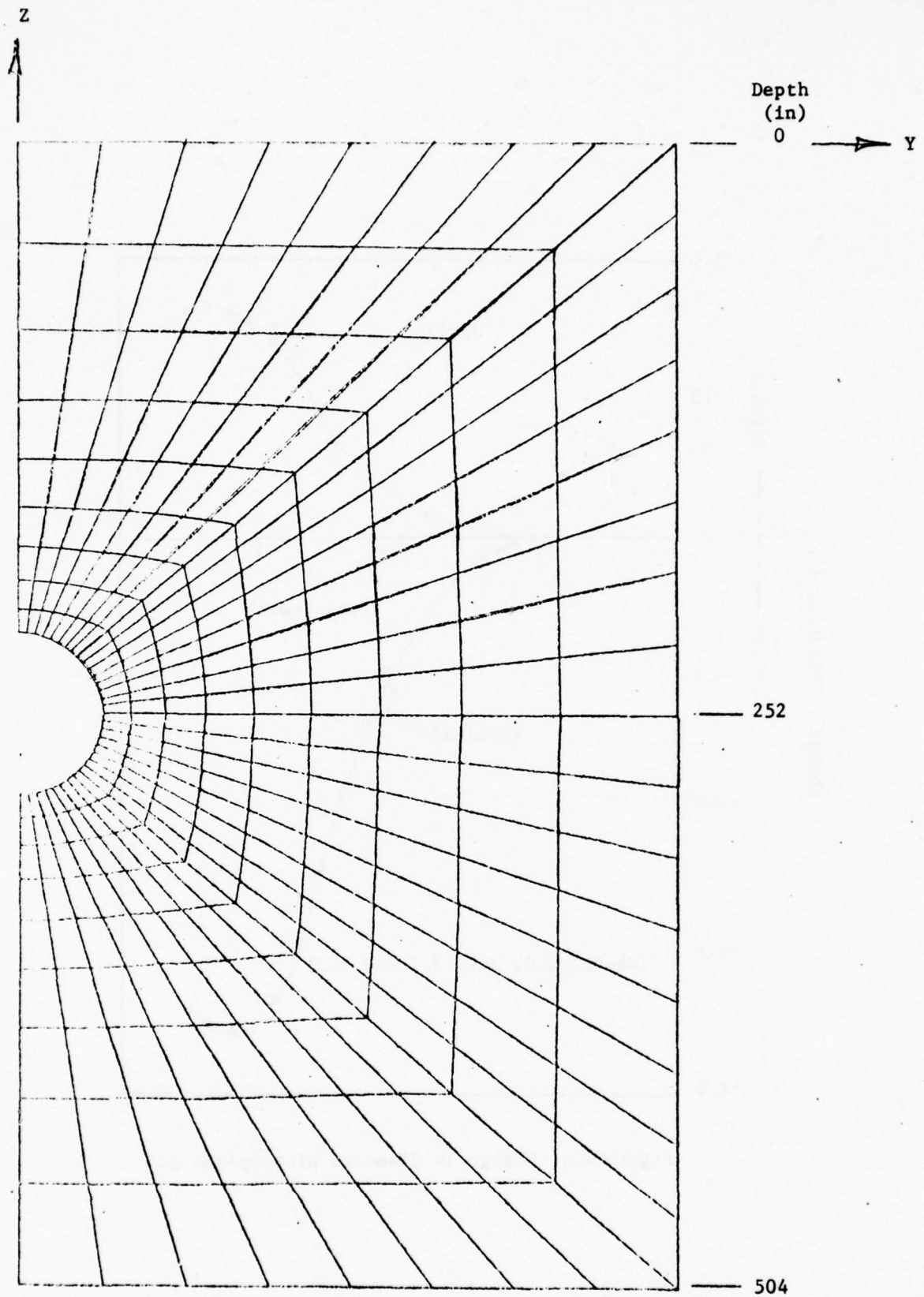


Figure 13. Change in diameter history-Run DC5



a. Tuff Elements (0" - 504")

Figure 14. Homogeneous Sphere Mesh (Mesh 4.0)

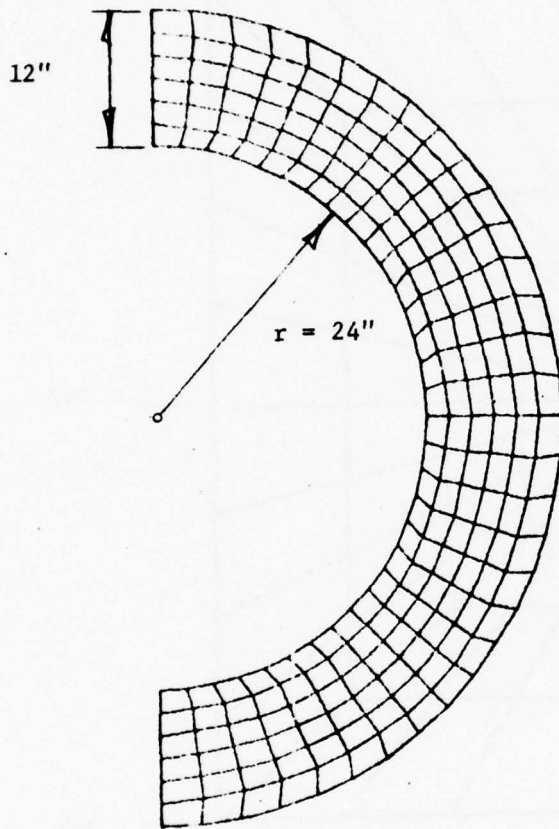
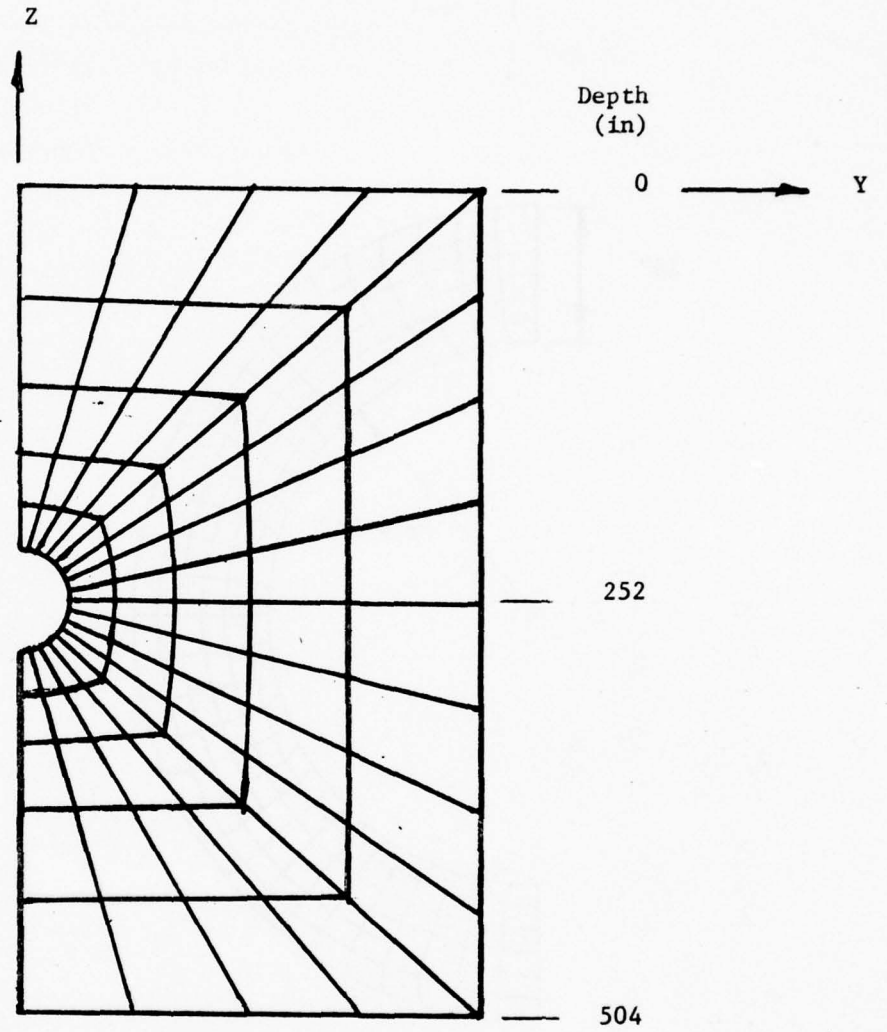


Figure 14b. Fiber Reinforced Concrete Elements



a. Tuff Elements (0" - 504")

Figure 15. Composite Built-Up Liner (Mesh 5.0)

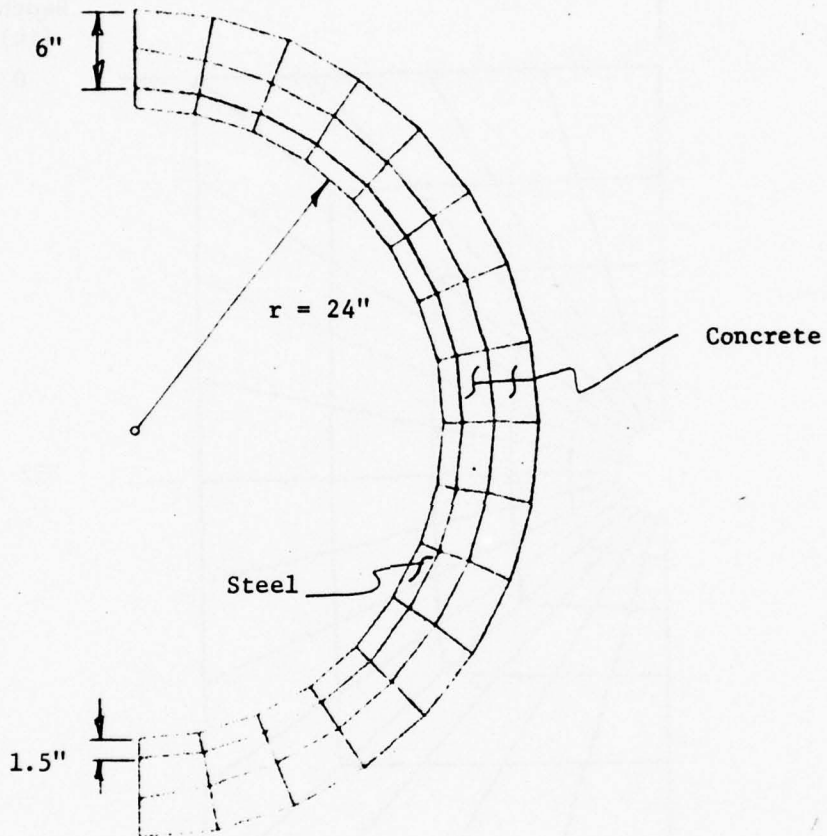
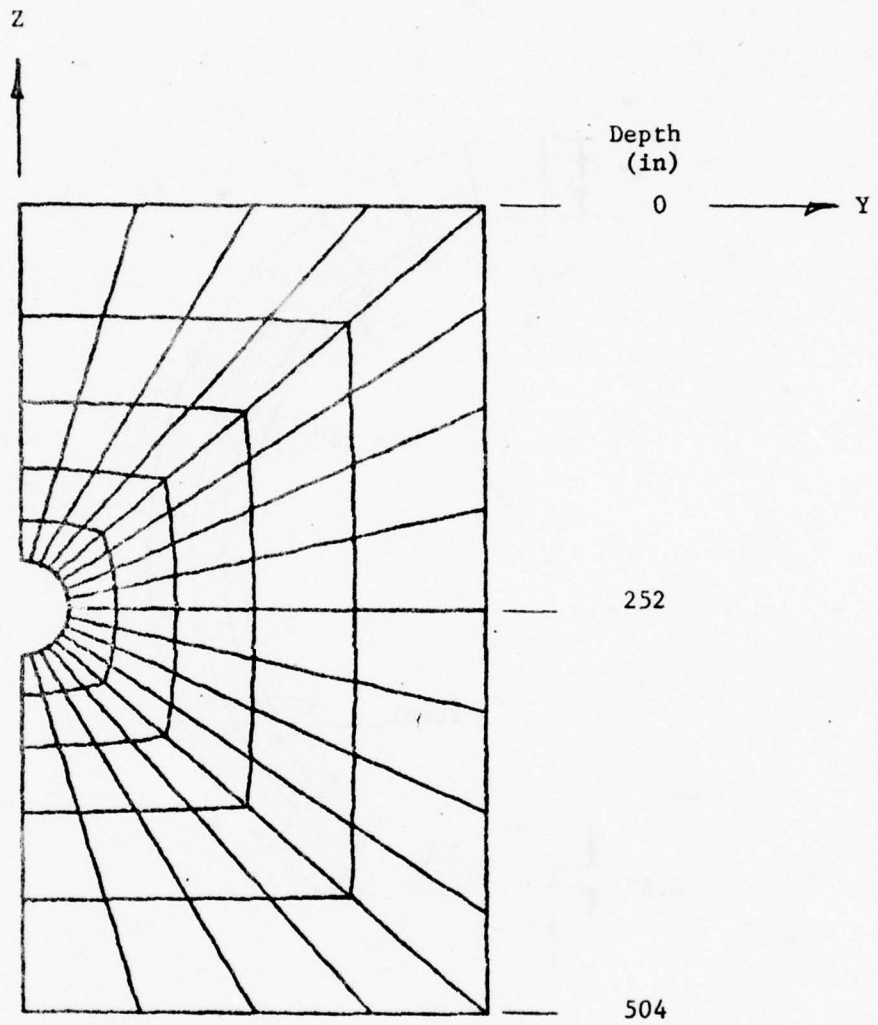


Figure 15b. Steel and Cellular Concrete Elements



a. Tuff Elements (0" - 504")

Figure 16. Composite Integral Liner (Mesh 6.0)

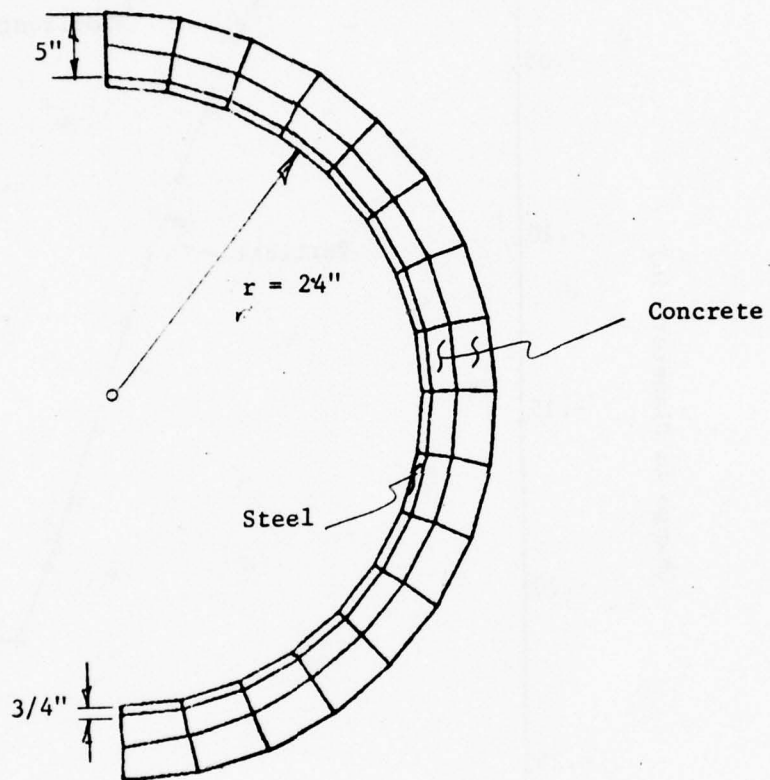


Figure 16b. Steel and Concrete Elements

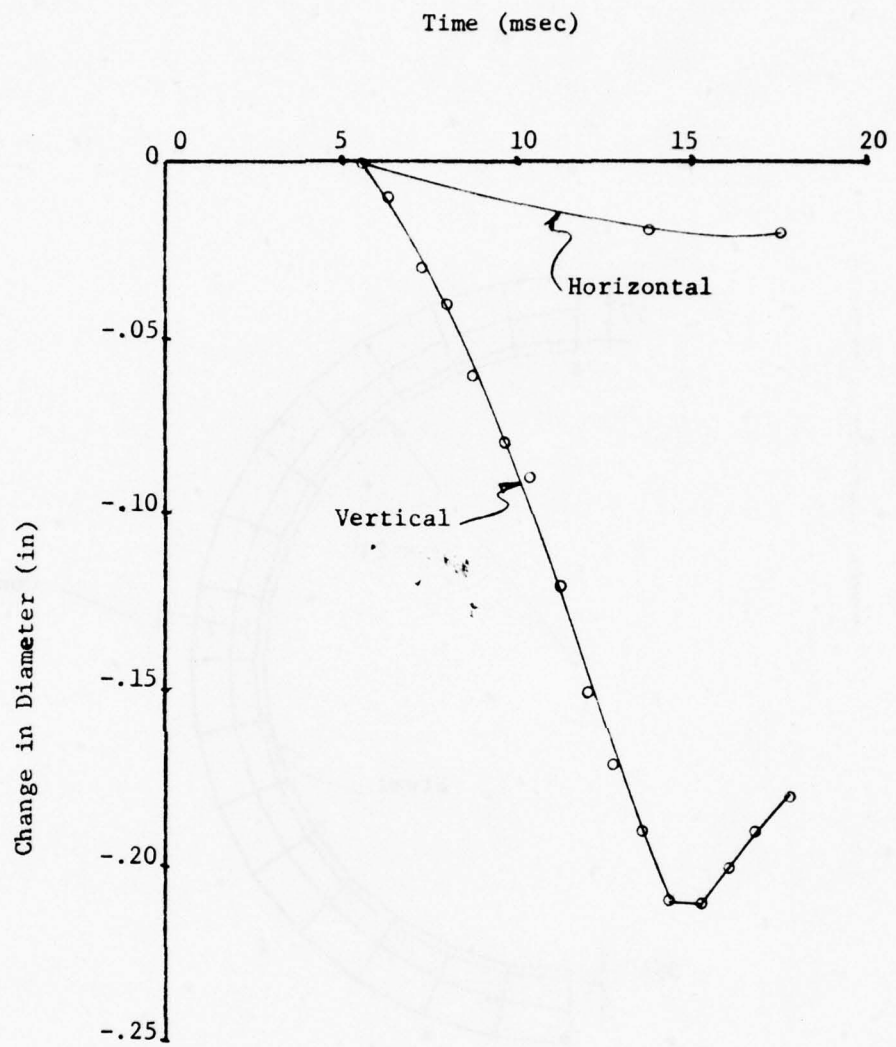


Figure 17. Change in diameter history; Mesh 4.0-Run DHS2

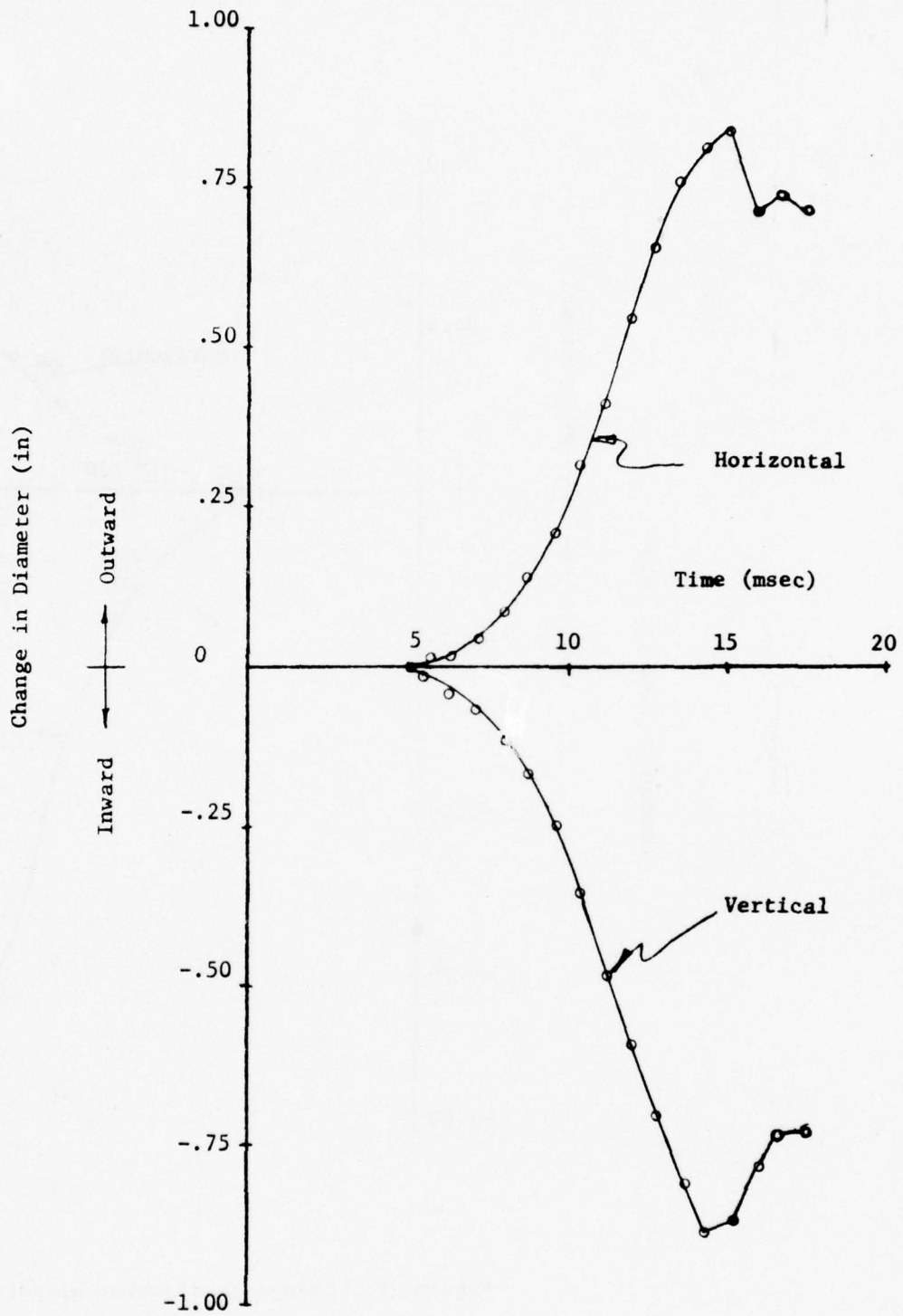


Figure 18. Change in diameter history; Mesh 5.0-Run DBL2

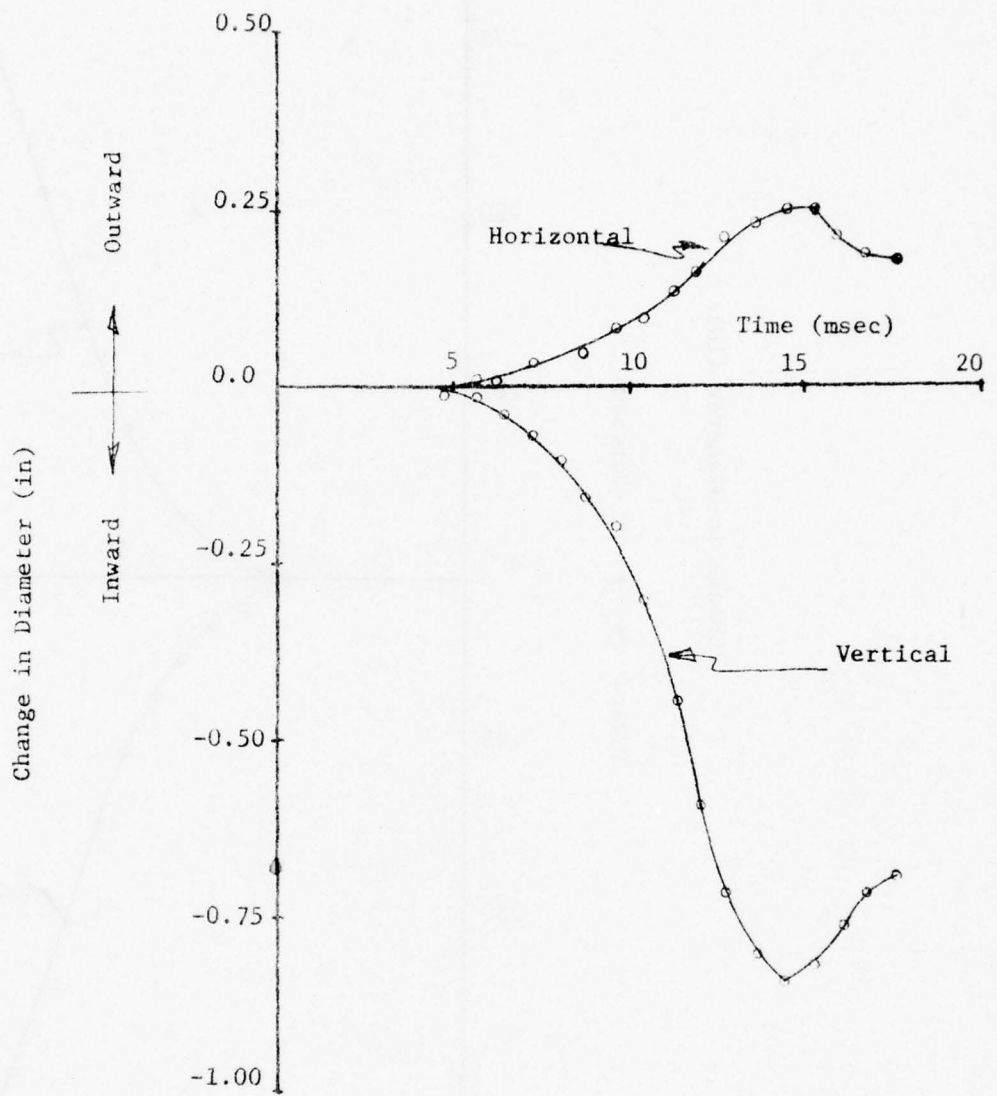


Figure 19. Change in diameter history; Mesh 6.0-Run DIL2

APPENDIX A
DEVELOPMENT OF MATERIAL PARAMETERS

INTRODUCTION

The material models employed should accurately represent the actual materials under field conditions. That is, the constitutive relationships must be valid throughout the expected loading range. Several linear and nonlinear models are available in NONSAP to describe material behavior: the linear elastic isotropic model, the von Mises model, the Drucker-Prager model and a curve description model with tension weakening. The von Mises and Drucker-Prager models have explicit yield functions which specify the state of multiaxial stress corresponding to the start of plastic flow. The von Mises yield surface is parallel to the hydrostat, and the Drucker-Prager yield surface is at an angle to it. Both models may incorporate flow rules and hardening rules. Currently in NONSAP the von Mises condition can be used for either perfectly plastic conditions or isotropic hardening; and the Drucker-Prager yield condition is limited to elastic, perfectly plastic analysis. In both cases an initially elastic material is assumed. The curve description model is an incremental stress-strain law which describes tangent bulk moduli in loading (K_L) and unloading (K_U) and the loading shear modulus (G_L) as piecewise linear functions of volumetric strain (e_V). This model has no explicit yield function, and it allows the material to weaken abruptly (crack) if the tensile stress resulting from applied loads exceeds the allowable tensile strength. Model selection for the analysis was based on laboratory material test data supplied by Defense Nuclear Agency (DNA) contractors and supplemented with material behavior information from the technical literature.

TUFF

The experimental test data supplied by Paul Weidlinger Associates^{A1} was initially used to derive a tuff model. Results from one-dimensional, hydrostatic, and triaxial tests are shown in Figures A1, A2 and A3, respectively. These figures indicate that the material does not behave linear elastically at the stress levels of interest and that some form of yielding must be incorporated into the constitutive relationships. The Drucker-Prager yield model was selected to model this inelastic behavior. The free field, the cavity, and the homogeneous sphere used this model (Tuff No. 1). The composite built-up liner and the composite integral liner used a different tuff model (Tuff No. 2) based on more recent experimental data from Terra Tek^{A2}. The derivation of Tuff No. 1 is outlined below. A similar technique, which is not shown, was also used for Tuff No. 2.

Mohr circles are shown in Figure A4 for the unconfined compression test and the 0.5-Kbar confining stress test. A failure envelope was then constructed which has a cohesive intercept, $c = 0.3$ Kbar and a friction angle, $\phi = 9.23^\circ$. Values of E and ν were chosen to best describe the behavior of the tuff at the 0.5-Kbar stress level. A trial and error technique is used to determine these values from the given data and from the following elastic equations:

$$K = \frac{E}{3(1 - 2\nu)} \quad (1)$$

$$G = \frac{E}{2(1 + \nu)} \quad (2)$$

$$M = \frac{E(1 - \nu)}{(1 + \nu)(1 - 2\nu)} \quad (3)$$

$$K_o = \frac{\nu}{1 - \nu} \quad (4)$$

where:

- G = Modulus of Elasticity in shear (psi)
- K = Bulk Modulus (psi)
- M = One-dimensional confined modulus (psi)
- K_o = At-rest coefficient of lateral earth pressure

Because 1-D strain tests are more difficult to perform on rock than soil, the data from the hydrostatic and triaxial tests are used to determine E and ν . The 1-D test data are used to check results. Values for the shear modulus, G, at each level of confining stress are calculated from Figure A3 (G = one-half the slope of stress difference versus strain difference). These values were then plotted against the confining stress in Figure A5. The trial and error procedure is as follows:

1. Assume a value for K_o.
2. Determine the hydrostatic stress state equivalent to the 0.5 Kbar 1-D confined stress state.

$$p_H = \frac{1 + 2K_o}{3} \sigma_v$$

where: σ_v = Vertical 1-D stress

p_H = Equivalent hydrostatic stress

3. Determine the secant bulk modulus, K, at this stress level from Figure A2.
4. Determine the confining stress, p_T , in the triaxial test equivalent to the 0.5-Kbar 1-D confined stress state.

$$p_T = K_o \sigma_v$$

5. Determine G at this stress level from Figure A5.
6. Determine E and ν by solving Equations 1 and 2 simultaneously.

7. Determine K_0 from Equation 4 and compare it to the assumed value.

Iterate these 7 steps until the results converge. Assuming an initial value of $K_0 = 0.30$, the following results are obtained after three iterations:

$$K_0 = 0.40$$

$$G = 12 \text{ Kbar} = 174,000 \text{ psi}$$

$$K = 24 \text{ Kbar} = 348,000 \text{ psi}$$

$$E = 30.9 \text{ Kbar} = 448,000 \text{ psi}$$

$$\nu = 0.286$$

$$M = 40 \text{ Kbar} = 581,000 \text{ psi}$$

The dotted straight lines in Figures A1, A2 and A3 are drawn to represent these moduli. The value of M obtained directly from Figure A1 at the 0.5-Kbar stress level is 32 Kbar. This compares reasonably well with the value calculated above.

These derived values for Tuff No. 1, as well as the Tuff No. 2 values, are shown in Table 1.

STEEL

The cavity, the composite built-up liner, and the composite integral liner contain a steel cylindrical liner. The cavity liner is assumed to behave elastically while the von Mises model is selected to describe the nonlinear behavior of the other two. The material parameters are shown in Table 1.

FIBER REINFORCED CONCRETE

The homogeneous spherical shell is constructed of steel fiber reinforced concrete. In addition to increased tensile strength, concrete containing steel fibers has slightly increased compressive strengths, greater strain capacity, toughness, post-peak strength, and post-peak integrity than conventional concretes.^{A3} These characteristics are further enhanced under biaxial and triaxial compression.^{A4} Thus, the material definitely possesses elasto-plastic characteristics.

The designers of the structure have indicated that a shot day strength of 17,000 psi is probable. However, concrete experts at CEL feel that the interaction and compounding of the various factors contributing to such a high strength are not well understood. A more reasonable assumption for the shot day dynamic unconfined compressive strength is 10,000 psi*. This value is used in the analysis.

* Six months after shot day, CEL tested concrete cores from an unused sphere. The average static compressive strength was 12,450 psi.

A technical literature search dealing with triaxial testing of concrete was carried out to select the appropriate plasticity model for the fiber reinforced concrete. Literature indicates that concrete behavior is similar to tuff. That is, the Mohr failure envelope has both a cohesion intercept and a friction angle. Thus, the Drucker-Prager model is used. Since triaxial test data for the fiber reinforced concrete was not available, c and ϕ were estimated from the data available in the literature. Triaxial test data from References A5 and A6 are used to derive values of c and ϕ . That is, Mohr's circles were plotted using principal stress differences normalized with respect to f'_c and the average failure envelope is drawn. The results indicate that the cohesion is approximately $0.36 f'_c$ and the friction angle approximately 35° . Thus, for 10,000 psi fiber reinforced concrete, the cohesion is 3600 psi. According to Reference A3, the addition of steel fibers to concrete does not significantly affect Young's modulus or Poisson's ratio. An average value for Poisson's ratio of 0.24 was selected from Reference A3. The following equation was used to determine Young's modulus:

$$E = 33 w^{1.5} \sqrt{f'_c} \quad (5)$$

where, w = weight density of concrete (lb/ft^3). For $144 \text{ lb}/\text{ft}^3$ concrete, the calculated E is $5,700,000 \text{ psi}$.

REINFORCED CONCRETE

The cylindrical composite integral liner consists of a thin steel liner surrounded by reinforced concrete. The presence of the various rebars in the plain concrete shell changes the outer shell from a relatively simple homogeneous structure to a complicated "matrix" of interacting materials. The effect of the rebar on the structural behavior must therefore be considered in the analysis.

A special finite element study of a concentrated load acting on the end of a cantilever beam was undertaken to evaluate the interaction between the concrete and rebar. The three meshes shown in Figure A6 were used to model the beam, which was similar in thickness (5 in) to the reinforced concrete shell. Meshes 1 and 2 represent a plain concrete beam; Mesh 3 represents a reinforced beam. The concrete elements are all 8-node quadrilaterals; the steel rebar is modeled by truss elements. The area of the truss members was adjusted to match the steel area of the actual reinforced concrete shell. The primary objective is to determine the influence of the rebar on structural response. A concentrated load ($P = 1,000 \text{ lb}$) was applied to the beam tip. The theoretical end deflections of the plain concrete and the reinforced concrete beams were 0.117 inch. The deflections computed by NONSAP were 0.120 inch for all three meshes. This indicates that a plain concrete mesh can be used to model the stiffness of a reinforced concrete shell.

Under the postulated loading conditions, a triaxial compressive stress state should exist throughout the reinforced concrete. Recent experiments A5, A6, A7 indicate that plain concrete subjected to multiaxial loading, exhibits more ductility and higher strength than concrete subjected to uniaxial or biaxial loading. This behavior suggests that a Drucker-Prager plasticity model is applicable.

The only material property data supplied to CEL was the unconfined compressive strength (f'_c) of the plain concrete, 5500 psi. The previous approach of determining the friction angle and cohesion for the fiber reinforced concrete is also used for the plain concrete. The friction angle equals 35° and the cohesion is $0.36 f'_c$ (1980 psi). The value of E calculated from Equation 5 is 4,264,000 psi, while the value of Poisson's ratio is 0.17.

CELLULAR CONCRETE

Cellular concrete is a lightweight, low modulus backpacking material surrounding the steel liner in the composite built-up liner. Its function is to reduce the stresses acting on the structure through positive arching action.

Laboratory test data on cellular concrete performed by Waterways Experimental Station was used to determine which NONSAP material model is applicable. The idealized results from a hydrostatic test on 60 pcf cellular concrete are shown in Figure A7. Three distinct regions of behavior are present. Initially, the material deforms linearly up to a yield stress (σ_{yL}) of about 1500 psi. At this stress level the material begins to crush, reducing the amount of initial air space. This ideal plastic behavior stops at a hardening strain (e_{hL}) of about 20 to 30 percent. At this strain value, the void space has essentially been reduced to zero. The material is now capable of resisting subsequent loading. The modulus in this region is approximately one-half the initial modulus. This material behavior can best be approximated in NONSAP by the Curve Description Model. Neither the Drucker-Prager nor the von Mises model is capable of simulating this unique elastic-plastic behavior. To obtain the input for the Curve Description Model, the following trial and error procedure is used:

1. Determine approximate values for the model based on Figure A7.
2. Hydrostatically load an axisymmetric element using NONSAP.
3. Plot a $p-e_v$ curve and compare with Figure A7.
4. Modify the model and repeat steps 2 and 3 until satisfactory convergence is obtained.

The final values for the model are outlined in Table A1. The NONSAP $p-e_v$ curve for this model is shown in Figure A7.

The Elastic Model shown in Table 1 was obtained by assuming a Poisson's Ratio of 0.48 and a Bulk Modulus of 7500 psi (see Figure A7). Like the actual cellular concrete behavior, this linear approximation is very soft and has little shear resistance.

Table A1. Curve Description Model for Cellular Concrete

Volume Strain ϵ_v (Percent)	Loading Bulk Modulus K_L (psi)	Unloading Bulk Modulus K_U (psi)	Loading Shear Modulus G_L (psi)	Poisson's Ratio ν
0	90,000	90,000	67,500	0.20
0.008	16,000	90,000	650	0.48
0.050	5,000	90,000	200	0.48
0.20	5,000	90,000	200	0.48
0.30	14,000	90,000	570	0.48
10.0	37,500	90,000	1,520	0.48

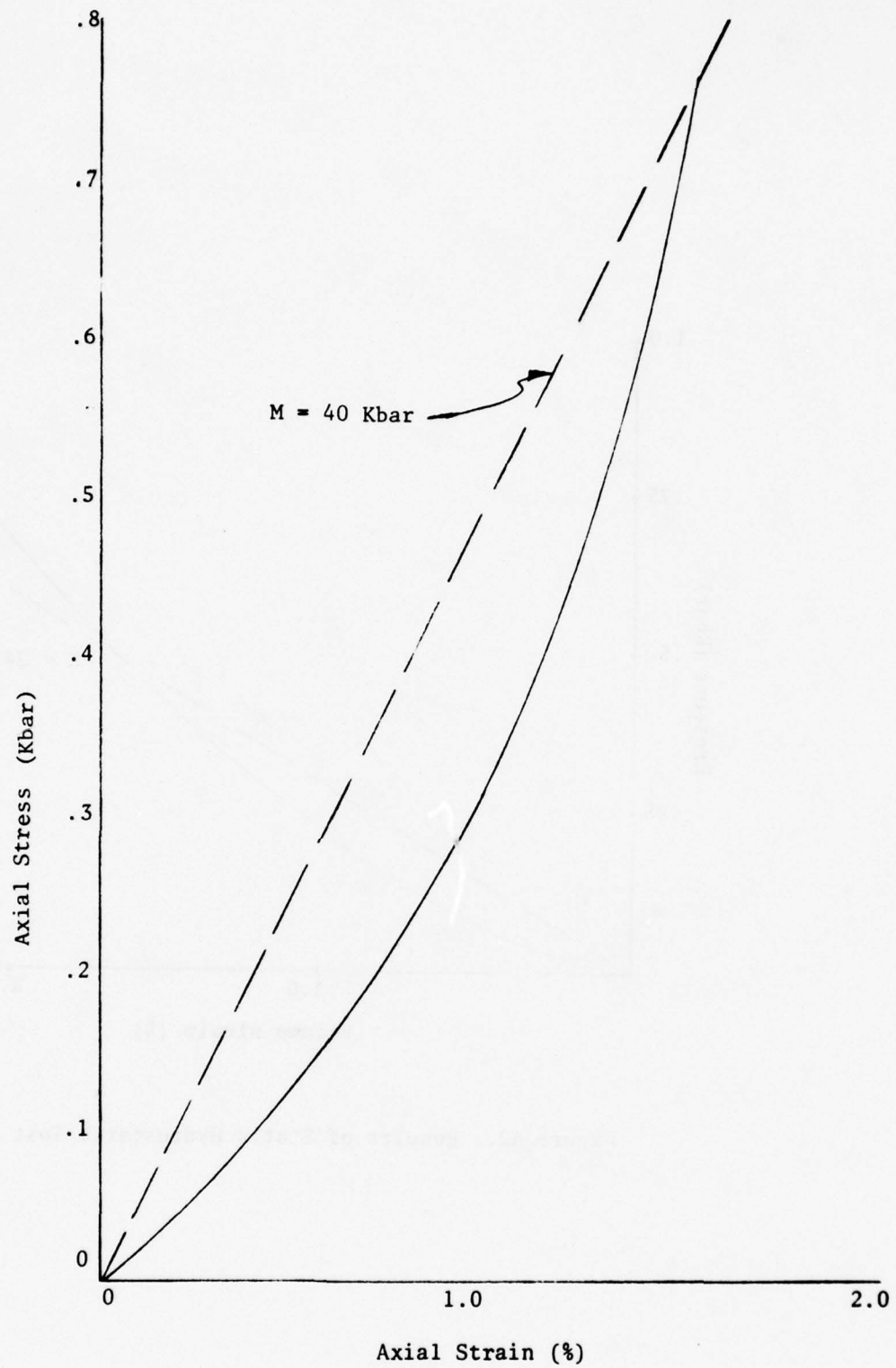


Figure A1. Results of static one-dimensional compression test on tuff

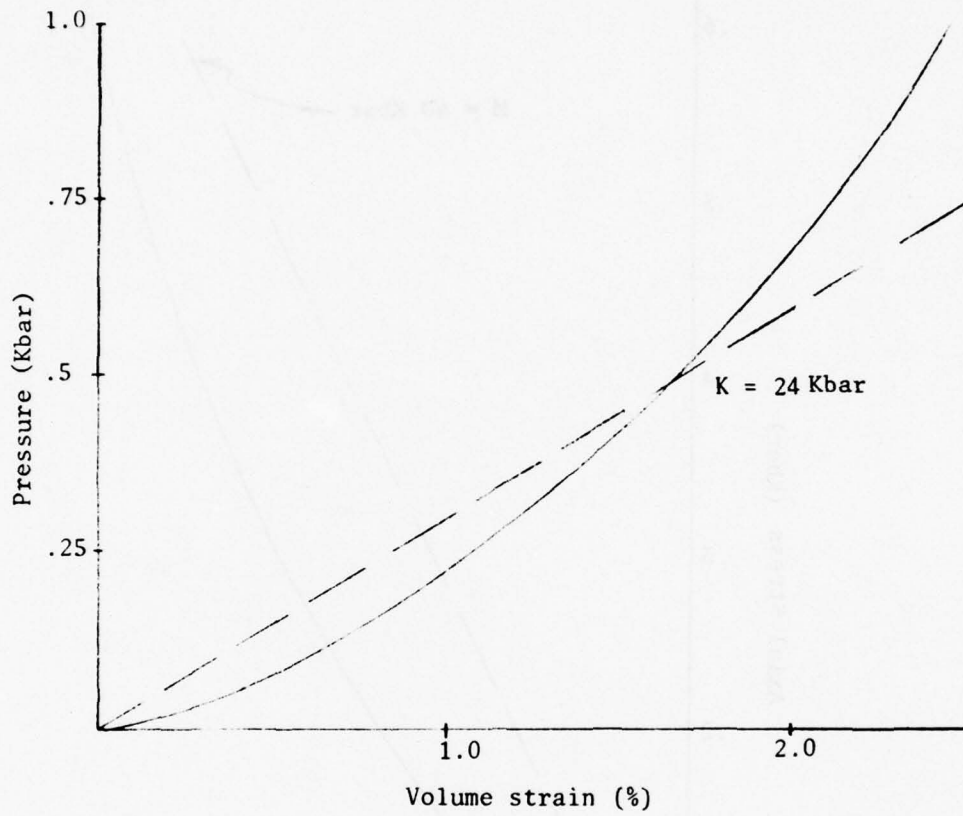


Figure A2. Results of Static Hydrostatic Test on Tuff

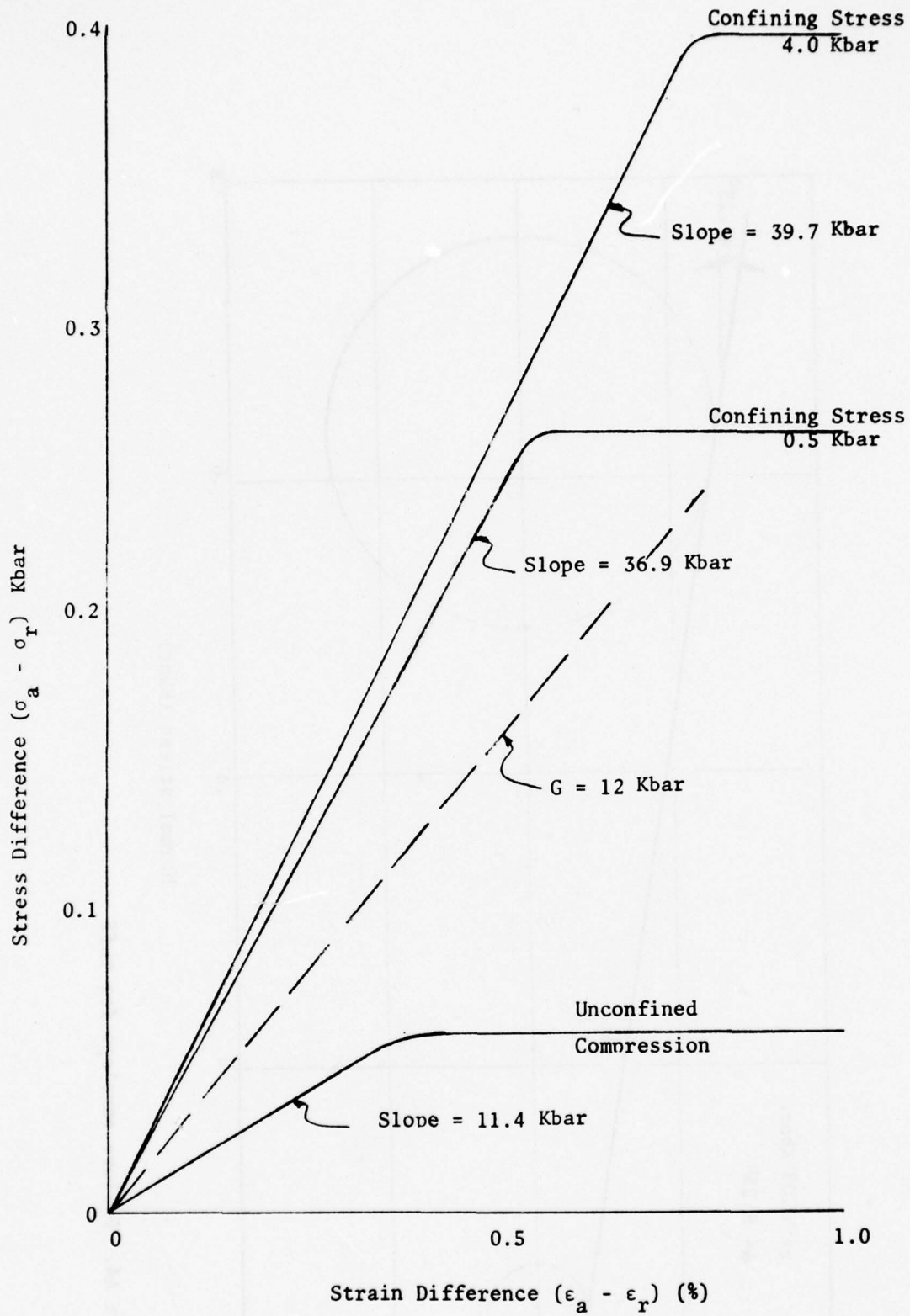


Figure A3. Results of Static Triaxial Tests on Tuff

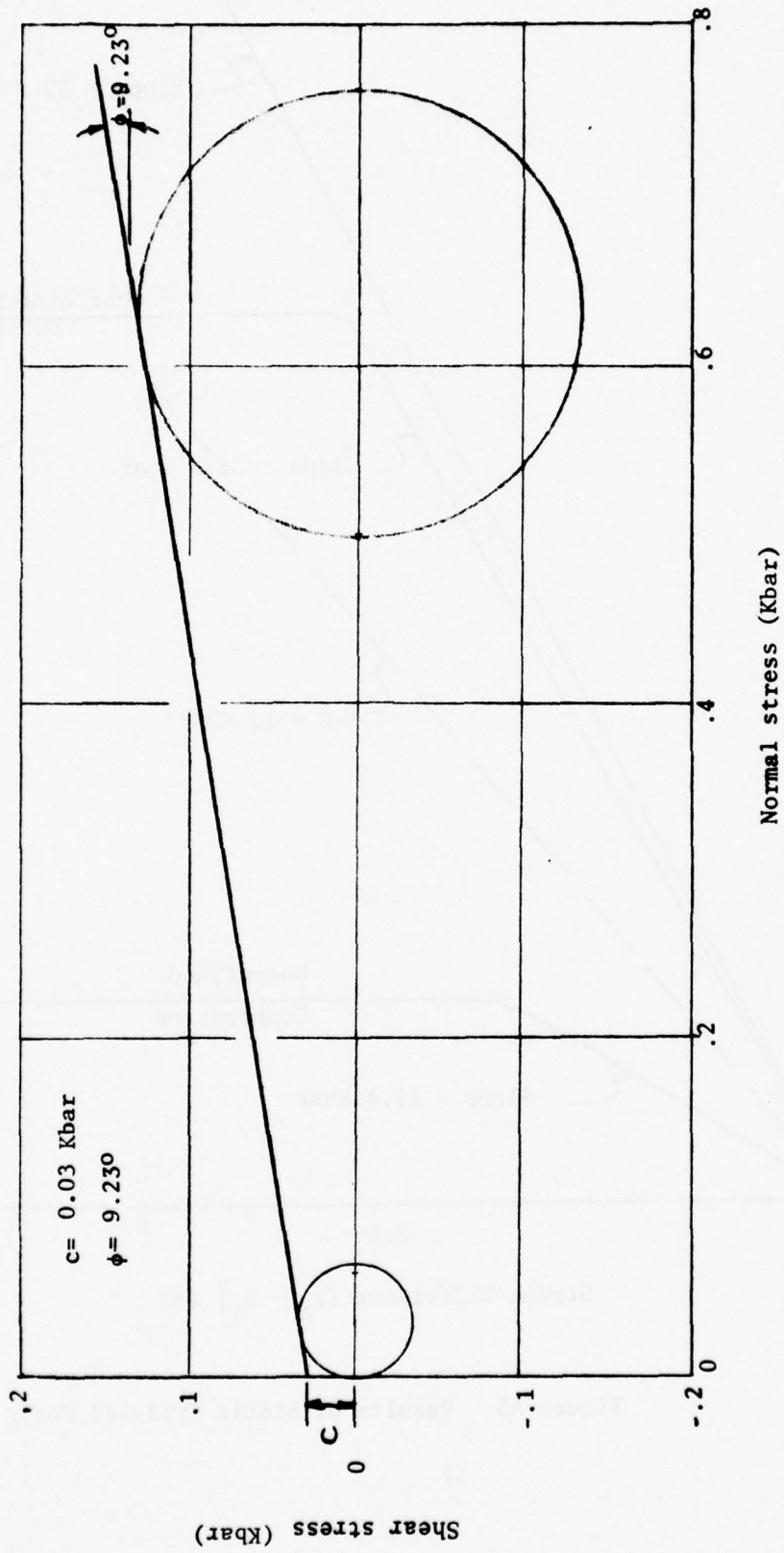


Figure A4. Failure envelope for tuff

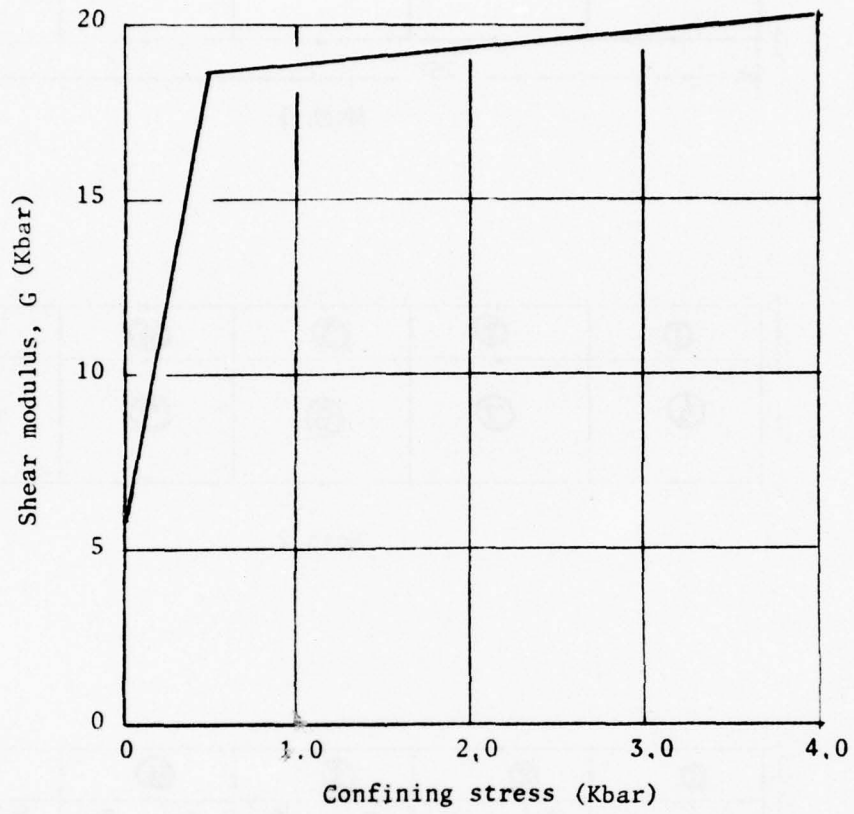
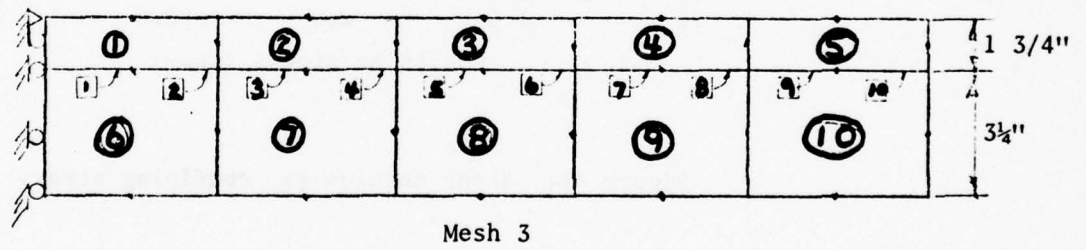
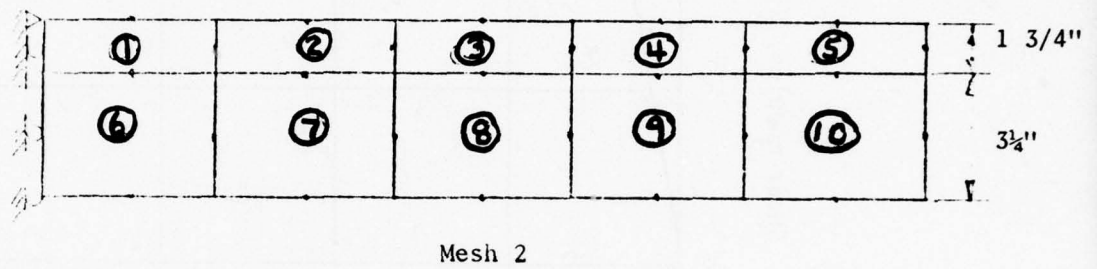
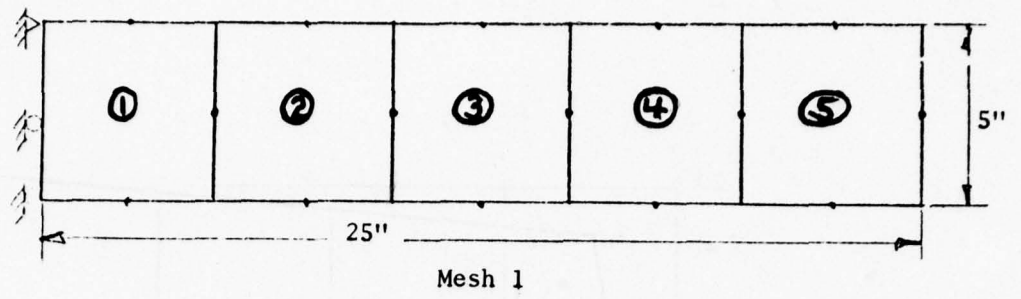


Figure A5. Shear modulus vs. confining stress



- Concrete Elements
- Steel Elements

Figure A6. Cantilever beam meshes.

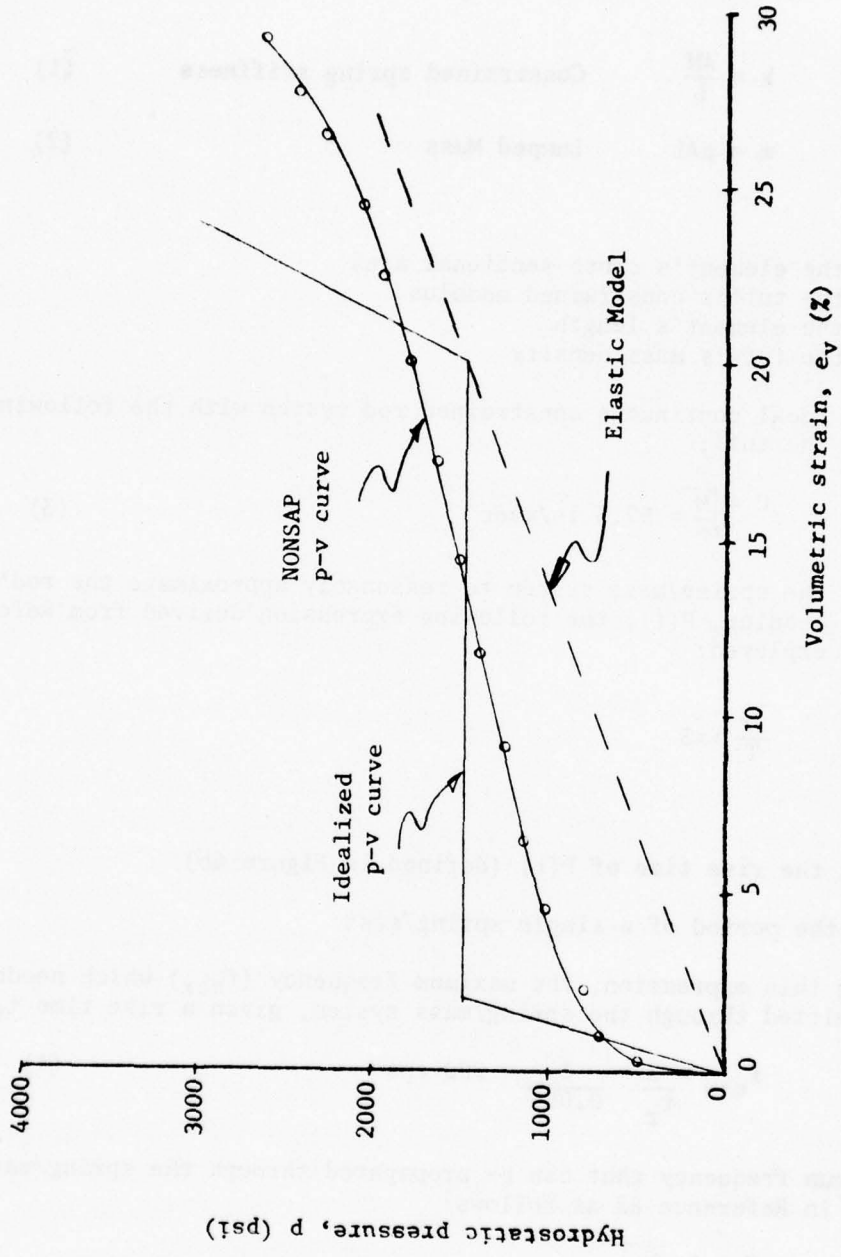


Figure A7. Hydrostatic test results

APPENDIX B
ELEMENT AND STEP SIZE SELECTION

In order to theoretically determine the element and step size of the columnar mesh (shown in Figure B1a), two analogous systems are employed (Figure B1b and B1c). B1b is a lumped mass and spring system defined as follows:

$$k = \frac{AM}{L} \quad \text{Constrained spring stiffness} \quad (1)$$

$$m = \rho AL \quad \text{Lumped Mass} \quad (2)$$

where:

A is the element's cross sectional area
M is the tuff's constrained modulus
L is the element's length
 ρ is the tuff's mass density

B1c is an ideal continuous constrained rod system with the following wave speed for the tuff:

$$C = \sqrt{\frac{M}{\rho}} = 57.5 \text{ in/msec} \quad (3)$$

To enable the spring/mass system to reasonably approximate the rod's response to a ramp loading, $P(t)$, the following expression derived from Reference B1 may be employed:

$$\frac{t_r}{T} \gg 3$$

where:

t_r is the rise time of $P(t)$ (defined in Figure 6b)

T is the period of a single spring/mass

Inverting this expression, the maximum frequency (f_{\max}) which needs to be transmitted through the spring/mass system, given a rise time t_r , is:

$$f_{\max} = \frac{3}{t_r} = \frac{3}{0.006} = 500 \text{ cps} \quad (4)$$

The maximum frequency that can be propagated through the spring/mass system is given in Reference B2 as follows:

$$f = \frac{1}{\pi} \sqrt{\frac{k}{m}}$$

Substituting from (1), (2), and (3):

$$f = \frac{1}{\pi} \sqrt{\frac{M}{\rho L^2}} = \frac{1}{L\pi} \sqrt{M} = \frac{C}{L\pi} \quad (5)$$

The maximum frequency (f_{\max}) that can be expected to propagate unattenuated through system (B1b) is given by (5). Combining (4) and (5) yields:

$$\frac{3}{t_r} = f_{\max} = \frac{C}{L\pi} \quad (6)$$

$$L = \frac{C t_r}{3\pi} = \frac{(57.5)(6)}{3\pi} = 36.6 \text{ inches}$$

An alternative mesh size selection procedure is given in Reference B3 for use in conjunction with calculations for the continuous rod system as follows:

$$L = \frac{t_r C}{3}$$

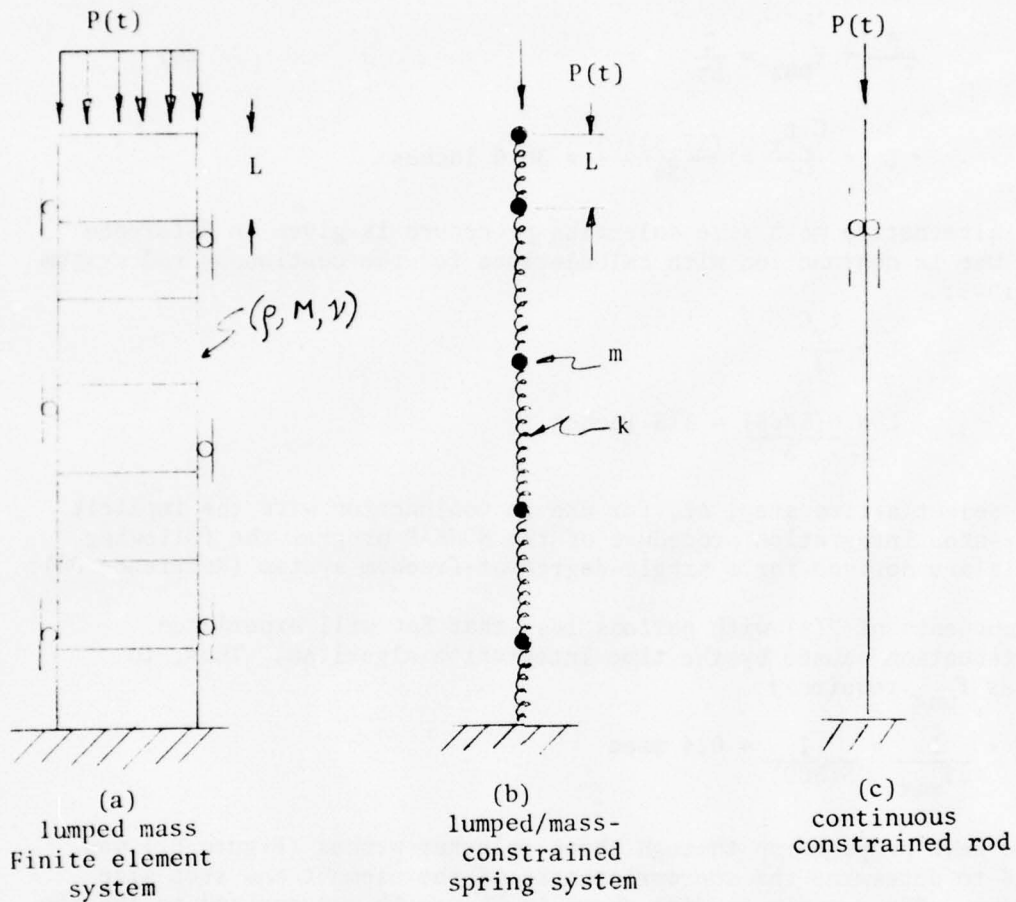
$$L = \frac{6(57.5)}{3} = 115 \text{ inches}$$

To select a time step, Δt , for use in conjunction with the implicit step-by-step integration procedure of the NONSAP program the following criteria are derived for a single-degree-of-freedom system (Reference B4):

Components of $P(t)$ with periods less than $5\Delta t$ will experience attenuation caused by the time integration algorithm. Thus, to pass f_{\max} requires:

$$\Delta t < \frac{1}{5f_{\max}} = \frac{1}{5(500)} = 0.4 \text{ msec}$$

The wave propagation through three columnar meshes (Figure B2) was studied to determine the appropriateness of the element and step size equations. The dynamic loading shown in Figure 6b was applied to the top surface of each mesh (linear Tuff No. 1). The vertical stress histories at the locations shown in Figure B2 are plotted in Figure B3. Figure B4 shows the shape of the stress wave as a function of L and Δt . The data shown indicates that for $L = 40$ inches and $\Delta t = 0.4$ msec satisfactory results are achieved.



where

$M = 581,380 \text{ psi}$ { constrained modulus for the tuff, see Table 1.

$\rho = .00017577 \frac{\text{lb} \cdot \text{sec}^2}{\text{in}^4}$ mass density of tuff.

$\nu = 0.286$ Poisson's ratio for tuff

Figure B1. Columnar Systems Used For Tuff Free Field Calculations

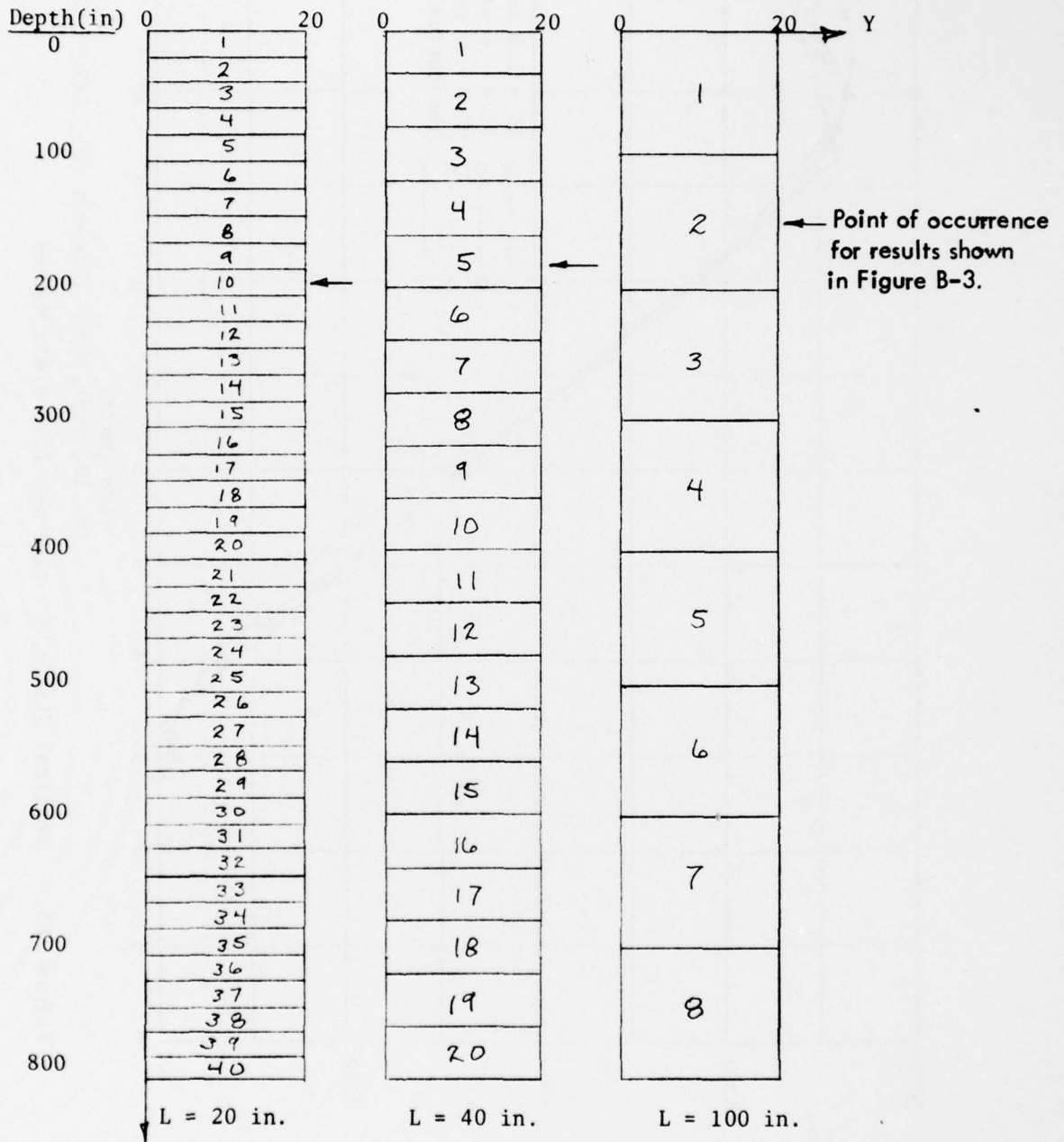


Figure B2. Free Field Meshes

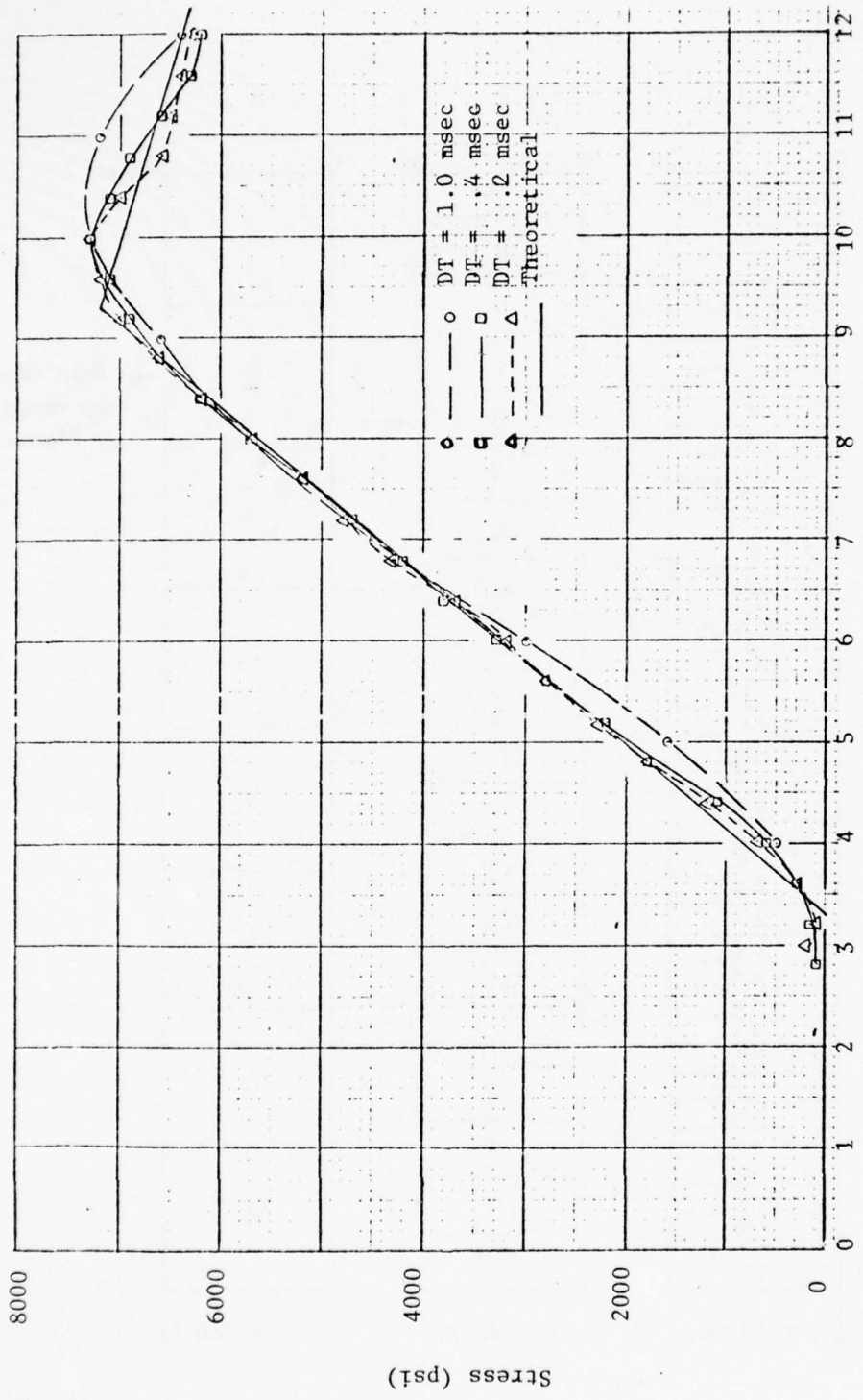
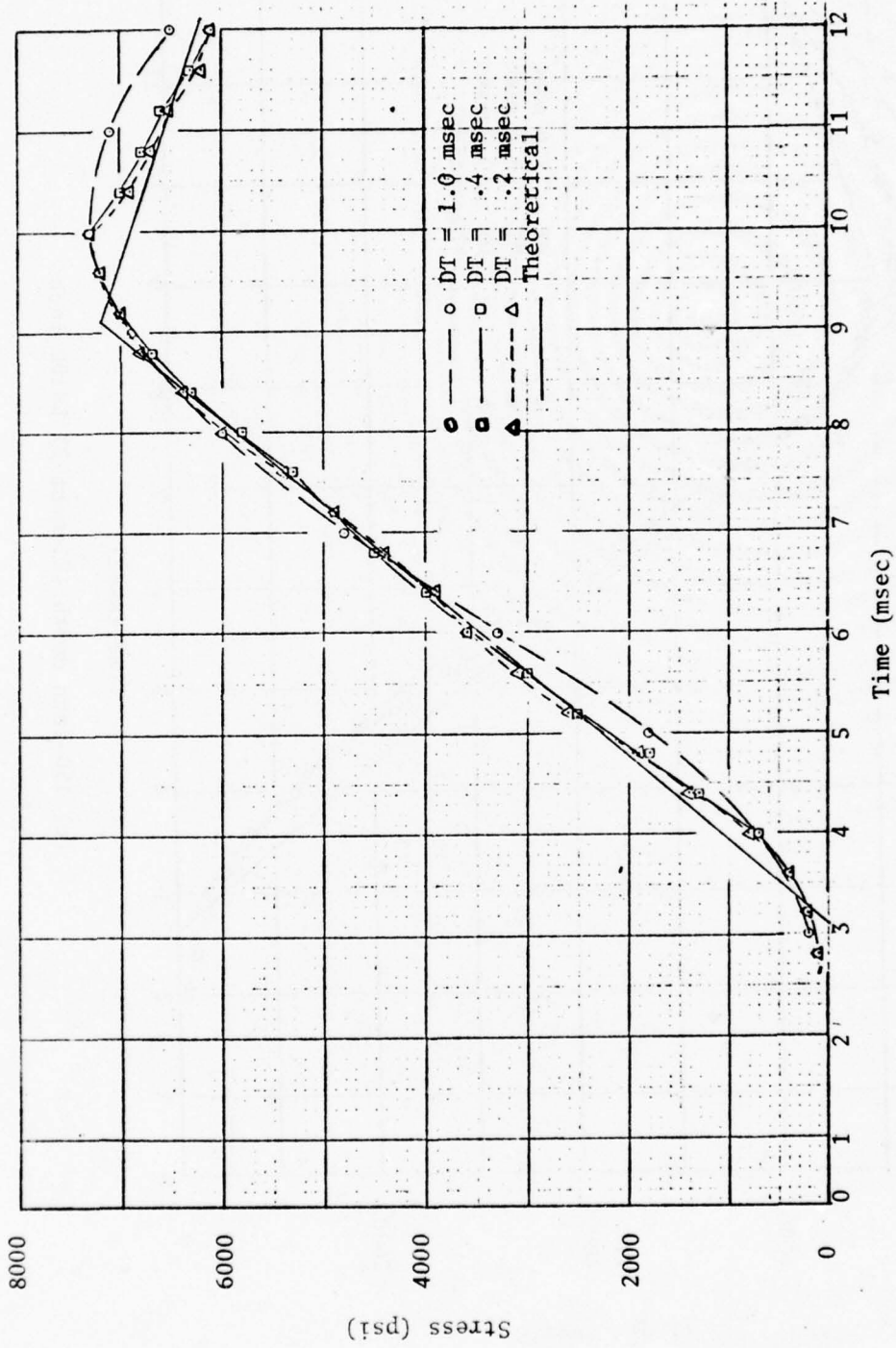
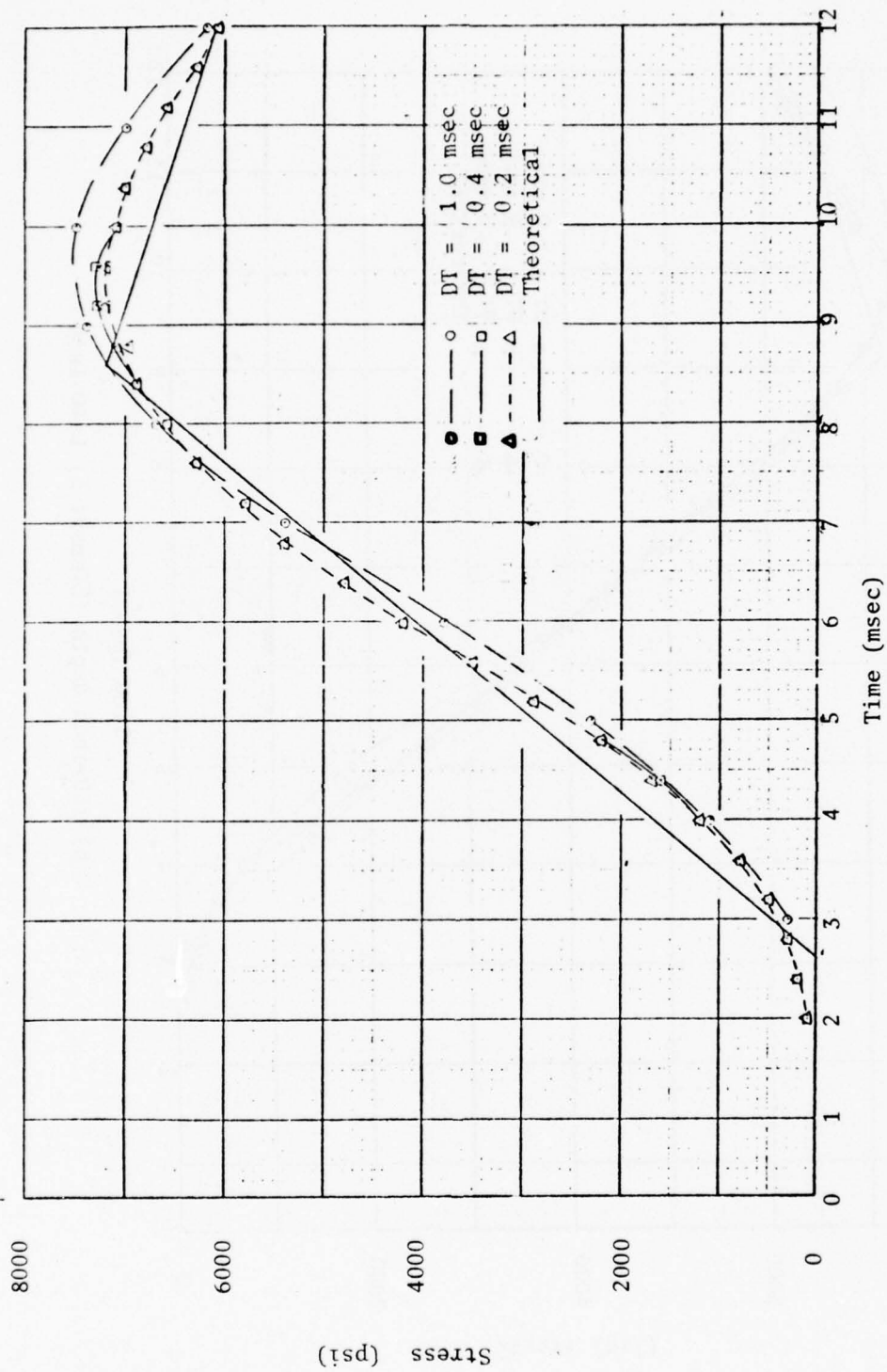


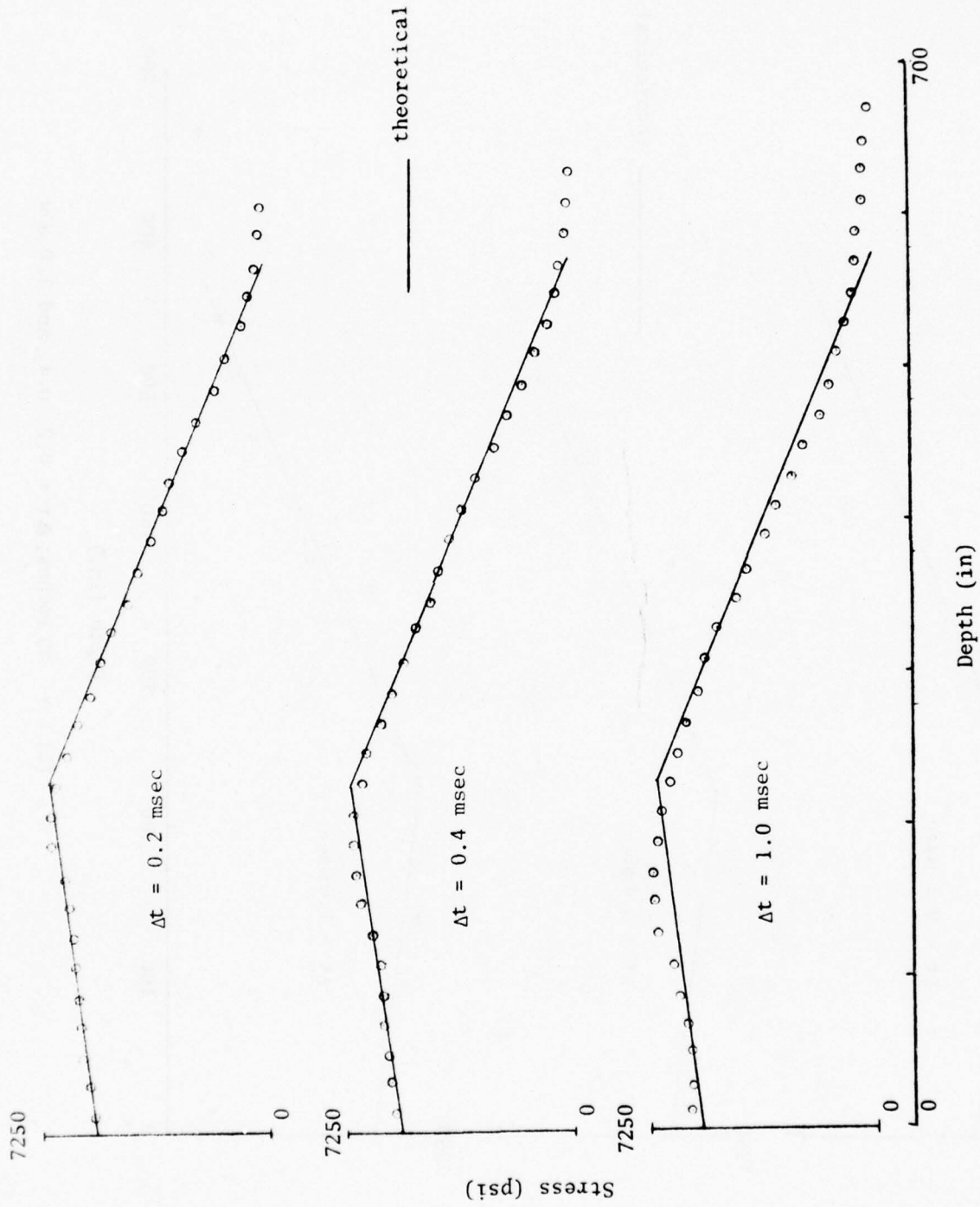
Figure B3. Vertical Stress vs. time for Free Field Meshes
 (a) 190-inch depth (Element 10), L=20 inch



(b) 180-inch depth (Element 5) L=40 inch

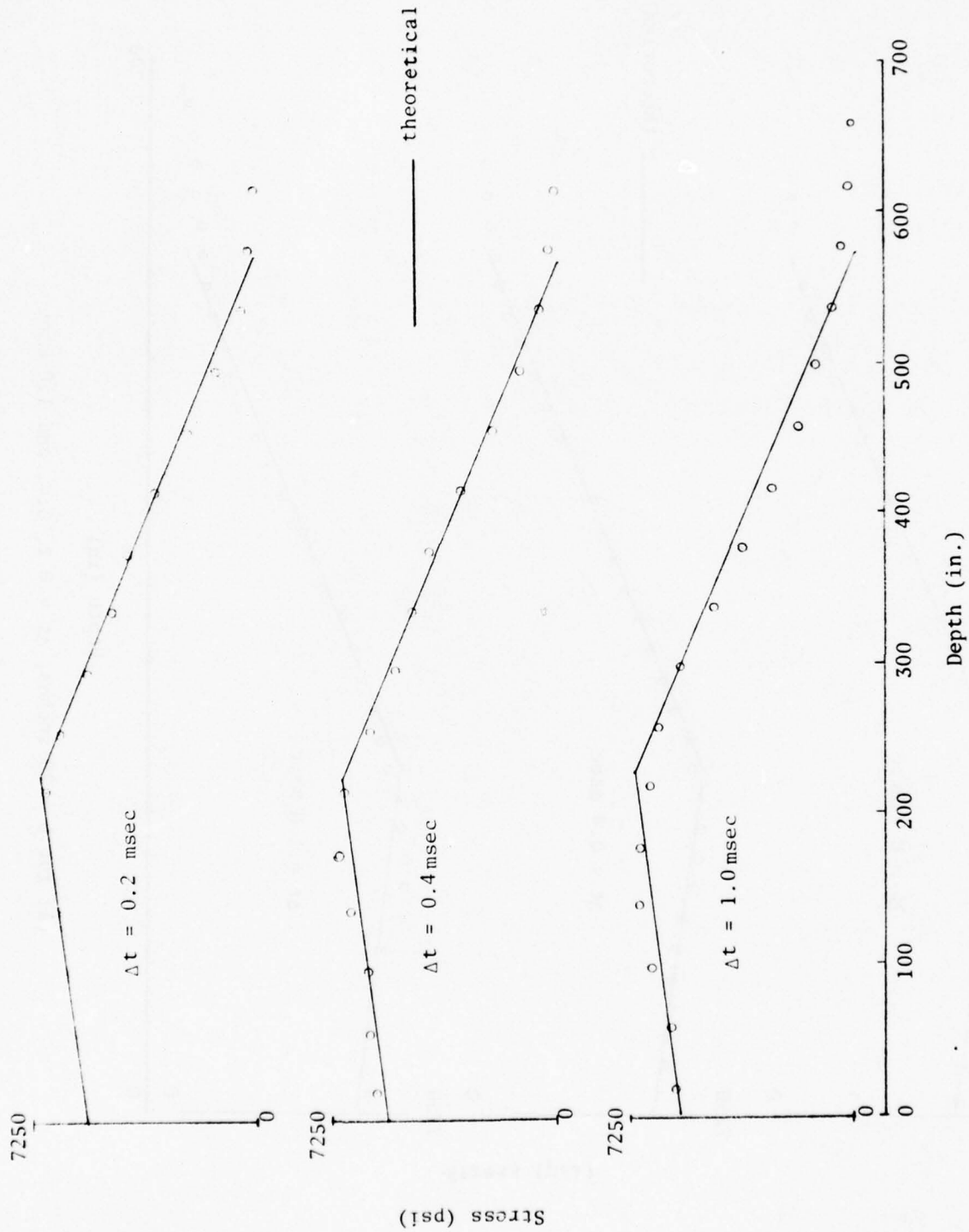


(c) 150-inch depth (Element 2) L=100 inch

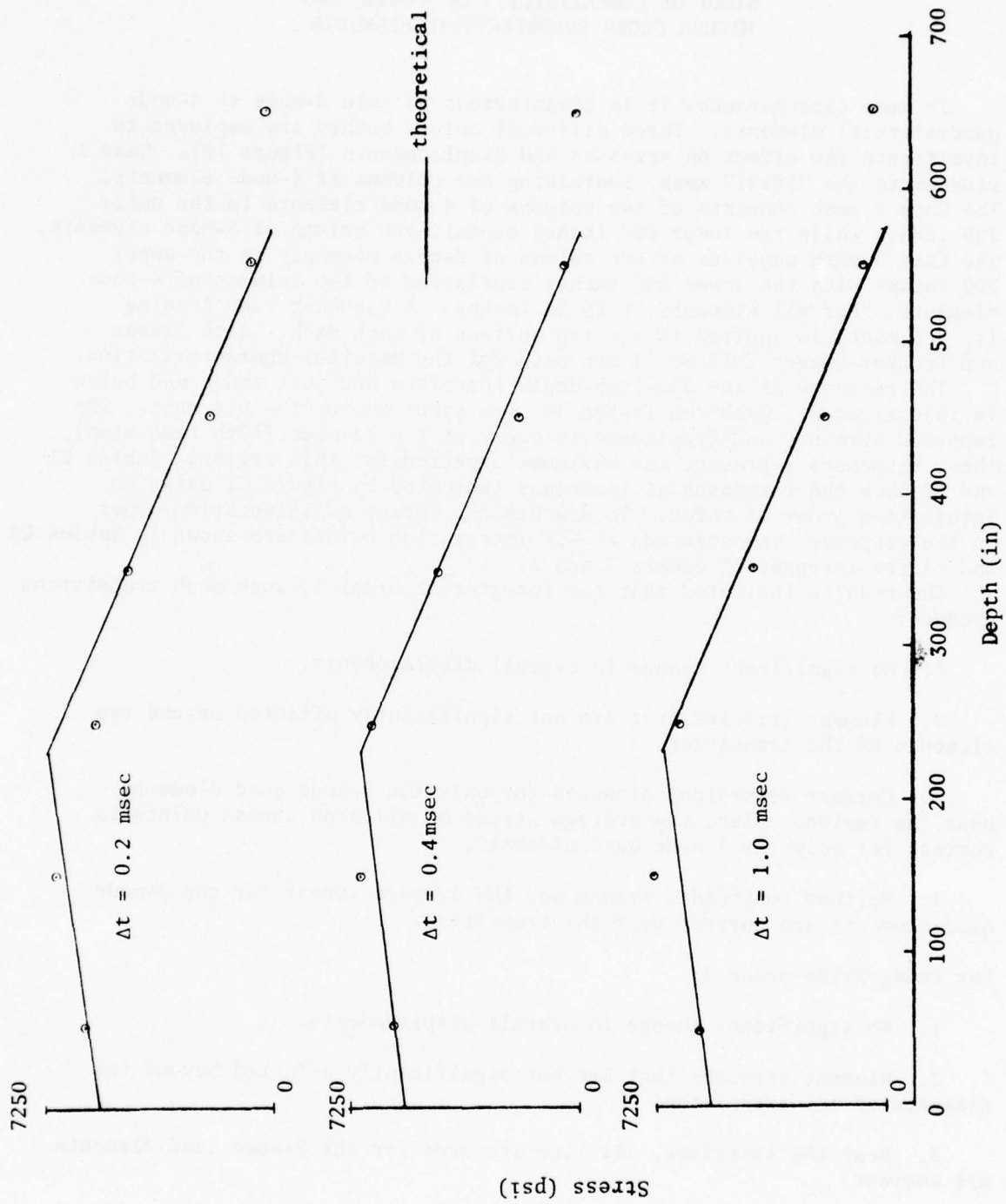


(a) for $L = 20$ inches, $\Delta t = 0.2, 0.4, \text{ and } 1.0 \text{ msec}$

Figure B4. Stress Wave Profile at 10 msec



(b) $L = 40$ inches, $\Delta t = 0.2, 0.4, \text{ and } 1.0 \text{ msec}$



(c) for $L = 100$ inches, $\Delta t = 0.2, 0.4$ and 1.0 msec

APPENDIX C
STUDY OF COMPATIBILITY OF 4-NODE AND
HIGHER ORDER QUADRILATERAL ELEMENTS

In some circumstances it is advantageous to join 8-node to 4-node quadrilateral elements. Three different column meshes are employed to investigate the effect on stresses and displacements (Figure 10). Case 1 represents the "ideal" mesh, containing two columns of 4-node elements. The Case 2 mesh consists of two columns of 4-node elements in the upper 200 inches while the lower 600 inches contain one column of 8-node elements. The Case 3 mesh consists of one column of 8-node elements in the upper 200 inches with the lower 600 inches consisting of two columns of 4-node elements. For all elements, L is 20 inches. A 0.50Kbar ramp loading ($t_r = 6$ msec) is applied to the top surface of each mesh. Both linear and Drucker-Prager Tuff No. 1 are used for the material characterization.

The response at the 200-inch depth interface and just above and below is investigated. Each run is for 30 time steps where $\Delta t = 0.4$ msec. The reported stresses and displacements occur at $t = 12$ msec (30th time step); these responses represent the maximums expected for this region. Tables C1 and C2 show the responses at locations indicated by Figure C1 using an integration order of three. To measure the impact of integration order on the response, the stresses at all integration points are shown in Tables C3 and C4 for integration orders 2 and 3.

The results indicated that for integration order 3, such mesh transitions produce:

1. No significant change in overall displacements.
2. Element stresses that are not significantly affected beyond two elements of the transition.
3. Correct centroidal stresses for only the 4-node quad elements near the region. Also, the average stress of all nine stress points is correct for only the 4-node quad elements.
4. Neither centroidal stress nor the average stress for the 8-node quad elements are correct near the transition.

For integration order 2:

1. No significant change in overall displacements.
2. Element stresses that are not significantly affected beyond two elements of the transition.
3. Near the interface, all four stresses for the 8-node quad elements are correct.
4. Near the interface, all four stresses for the 4-node quad elements are incorrect. However, the average stress is correct.

Table C1. Vertical Nodal Displacement at $t = 12\text{ms}$ (Inches)

Material Model	Case	Vertical Displacement At Top Surface			Vertical Displacement At 100 In. Depth			Vertical Displacement At 200 In. Depth		
		A	B	C	D	E	F	G	H	I
Drucker-Prager Tuff	1	-6.8281	-6.8281	-6.8281	-5.4091	-5.4091	-5.4091	-3.9925	-3.9925	-3.9925
	2	-6.8364	-6.8364	-6.8364	-5.4180	-5.4180	-5.4180	-4.0299	-3.9678	-4.0299
	3	-6.8324	-6.8367	-6.8324	-5.4155	-5.4196	-5.4155	-3.9560	-4.0235	-3.9560
Linear Tuff	1	-6.4547	-6.4547	-6.4547	-5.2076	-5.2076	-5.2076	-3.9618	-3.9618	-3.9618
	2	-6.4607	-6.4607	-6.4607	-5.2132	-5.2132	-5.2132	-3.9853	-3.9468	-3.9853
	3	-6.4598	-6.4595	-6.4598	-5.2129	-5.2128	-5.2129	-3.9407	-3.9792	-3.9407

Table C2. Vertical Stress at $t = 12ms$ (psi)

Material Model	Case	Stress Location (Taken at Element Centroid)					
		A, z=150 in.	B, z=170 in.	C, z=190 in.	D, z=210 in.	E, z=230 in.	F, z=250 in.
Drucker-Prager Tuff	1	-7296	-7237	-7152	-7159	-7301	-7446
		-7296 ^a	-7237	-7152	-7159	-7301	-7446
	2	-7313	-7256	-7167	-6603	-7379	-7439
		-7313	-7256	-7167			
	3	-7278	-7277	-6610	-7197	-7342	-7460
					-7197	-7342	-7460
Linear Tuff	1	-7280	-7247	-7191	-7180	-7248	-7367
		-7280	-7247	-7191	-7180	-7248	-7367
	2	-7291	-7256	-7197	-6767	-7326	-7368
		-7291	-7256	-7197			
	3	-7269	-7296	-6760	-7191	-7278	-7393
					-7191	-7278	-7393

^aSecond entries within the box occur for locations where a pair of side-by-side elements exist. The second entry is for the element on the left.

Table C3. Vertical Stress and its Deviation^a Caused by Transition for Linear Tuff (Integration Order 2) (psi)

Stress ^b Points	Location of Stress ^c for					
	Element No. (Case 2)					
	9	19	10	20	21	22
1	-7308 -61	-7207 40	-6784 407	-7611 -420	-7190 -10	-7273 -25
2	-7308 -61	-7207 40	-6784 407	-7611 -420	-7184 -4	-7249 -1
3	-7207 40	-7308 -61	-7611 -420	-6784 407	-7190 -10	-7273 -25
4	-7207 40	-7308 -61	-7611 -420	-6784 407	-7184 -4	-7249 -1
	Element No. (Case 3)					
	9	10	11	41	12	42
1	-7225 22	-7177 14	-6780 400	-7607 -427	-7332 -84	-7232 16
2	-7239 8	-7181 10	-6780 400	-7607 -427	-7332 -84	-7232 16
3	-7225 22	-7177 14	-7607 -427	-6780 400	-7232 16	-7332 -84
4	-7239 8	-7181 10	-7607 -427	-6780 400	-7232 16	-7332 -84

^aFirst entry in box is vertical stress while the second entry is the difference between first entry and corresponding stress for the "ideal" solution (Case 1, Figure 10b)

^bLocation of stress output, 4 per element, see Figure 10a.

^cElement numbers shown in Figure 10c and 10d.

Table C4. Vertical Stress and its Deviation^a Caused by Transition for Linear Tuff (Integration Order 3) (psi)

Stress ^b Point	Location of Stress ^c for					
	Element No. (Case 2)					
	9	19	10	20	21	22
1	-7315 -68	-7196 50	-6711 480	-7683 -492	-7529 -349	-7220 28
2	-7315 -68	-7196 50	-6711 480	-7683 -492	-7525 -345	-7205 43
3	-7315 -68	-7196 50	-6711 480	-7683 -492	-7521 -341	-7189 59
4	-7256 -9	-7256 -9	-7197 -6	-7197 -6	-6771 409	-7342 -94
5	-7256 -9	-7256 -9	-7197 -6	-7197 -6	-6767 413	-7327 -79
6	-7256 -9	-7256 -9	-7197 -6	-7197 -6	-6763 417	-7311 -63
7	-7197 50	-7315 -68	-7683 -492	-6711 480	-7528 -349	-7220 28
8	-7197 50	-7315 -68	-7683 -492	-6711 480	-7525 -345	-7205 43
9	-7197 50	-7315 -68	-7683 -492	-6711 480	-7521 -341	-7189 59
	Element No. (Case 3)					
	9	10	11	41	12	42
1	-7176 71	-7515 -324	-6704 476	-7677 -497	-7337 -89	-7218 30
2	-7185 62	-7519 -328	-6704 476	-7677 -497	-7337 -89	-7218 30
3	-7194 53	-7522 -331	-6704 476	-7677 -497	-7337 -89	-7218 30

continued

Table C4. Continued

Stress ^b Point	Location of Stress ^c for					
	Element No. (Case 3)					
	9	10	11	41	12	42
4	-7287 -40	-6756 435	-7190 -10	-7190 -10	-7277 -29	-7277 -29
5	-7296 -49	-6760 431	-7190 -10	-7190 -10	-7277 -29	-7277 -29
6	-7305 -58	-6763 428	-7190 -10	-7190 -10	-7277 -29	-7277 -29
7	-7176 71	-7515 -324	-7677 -497	-6704 476	-7218 30	-7337 -89
8	-7185 62	-7519 -328	-7677 -497	-6704 476	-7218 30	-7337 -89
9	-7194 53	-7522 -331	-7677 -497	-6704 476	-7218 30	-7337 -89

^aFirst entry in box is vertical stress while the second entry is the difference between first entry and corresponding stress for the "ideal" solution (Case 1, Figure 10b)

^bLocation of stress output, 9 per element, see Figure 10a.

^cElement numbers shown in Figure 10c and 10d.

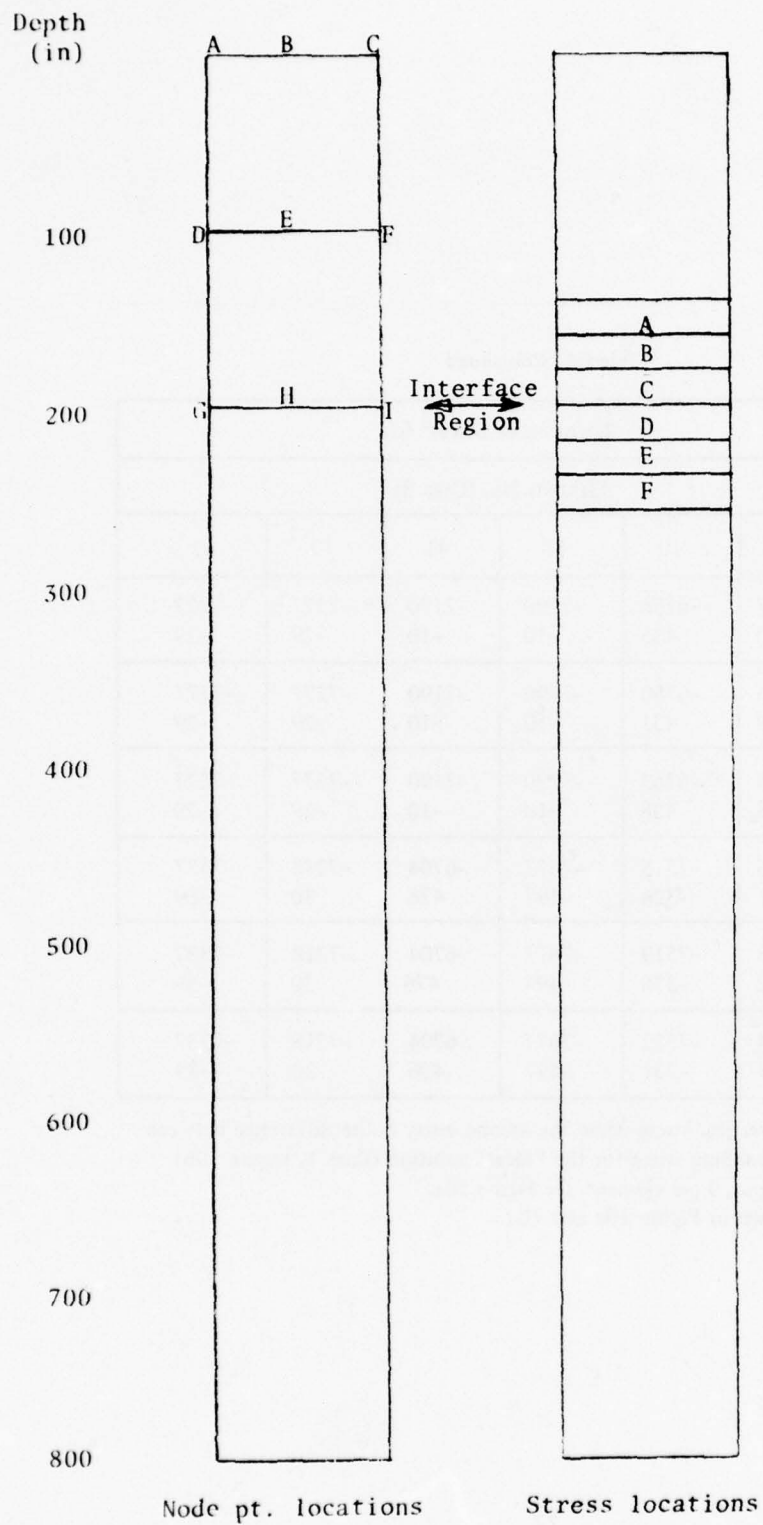


Figure C1. Location of Responses shown in Tables C1 and C2

APPENDIX D
RESTART USING PROGRESSIVELY LARGER Δt

The columnar mesh shown in Figure D1 is used to demonstrate that predictions at the structure site can be satisfactorily computed using a progressively increasing Δt . The Mighty Epic forcing function (Figure 6a) is applied to the top surface of the linear Tuff No. 1 column. For this run:

1. $\Delta t = 0.4$ msec for the first 50 steps (20 msec total)
2. $\Delta t = 1.0$ msec for next 50 steps (70 msec total)
3. $\Delta t = 5.0$ msec for next six steps (100 msec total)
4. $\Delta t = 50$ msec for the next 28 steps (1500 msec total)

The stress history at the 290-inch depth (Element 15) is shown in Figure D2. For this idealization the reflected wave arrives at Element 15 in 204 msec. As shown in Figure D2, the amplitude of the reflected stress wave is reduced by 95%.

This study suggests that a progressively increasing Δt is a viable means of reducing the run's cost and the system's degrees-of-freedom for "long-time" finite element runs. However, this conclusion must be checked on a "case-by-case" basis with verification runs being made for the particular idealization involved. Special attention must be applied in the region of interest to insure that secondary transient responses (i.e., those created by the structure's response to the forcing function) are neither prematurely attenuated nor wastefully computed.

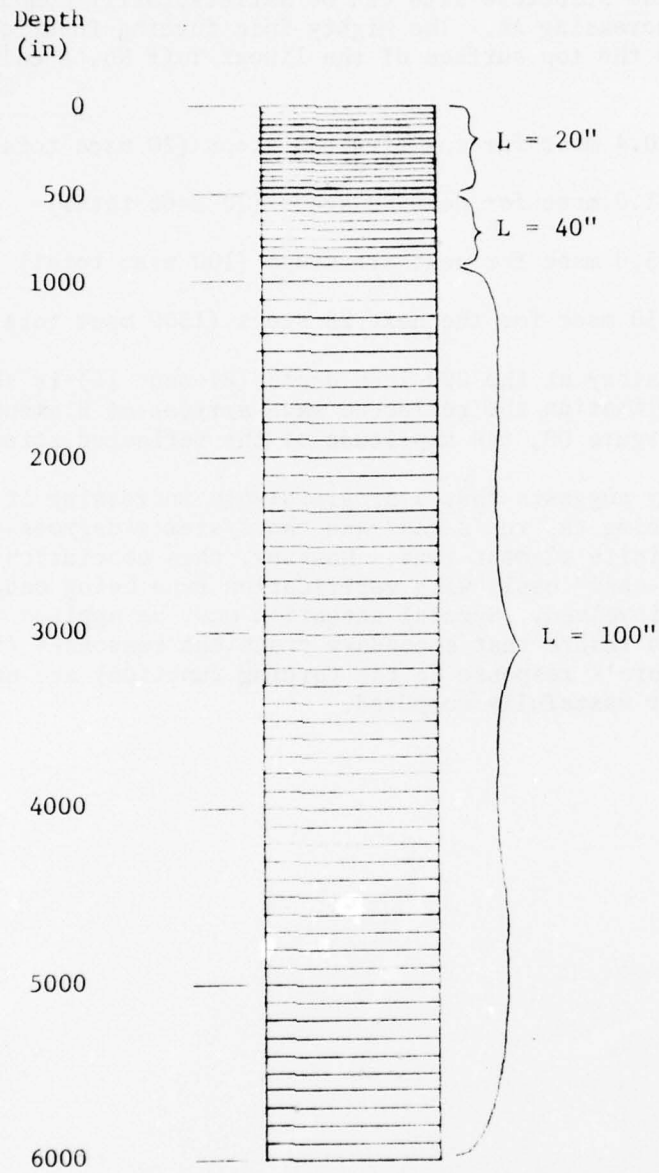


Figure D1. Columnar Mesh Used for Progressively Increasing Δt

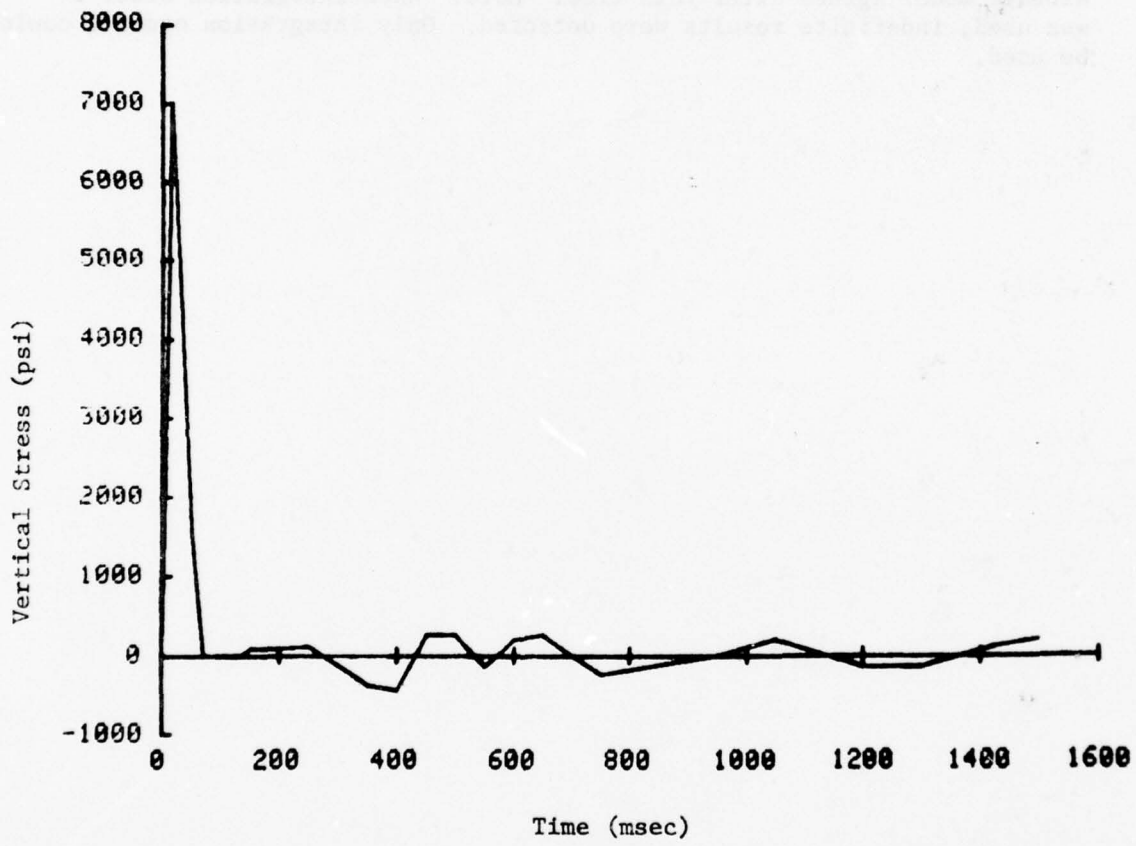


Figure D2. Vertical stress history at 290-inch depth

APPENDIX E
USE OF VELOCITY AS A FORCING FUNCTION

The velocity time history at the structure location ("0" on Figure 5) is integrated yielding a displacement time history. Stiff springs are inserted at the top nodes of a columnar mesh (Figure E1). Loads (Figure E2) which cause the desired displacement time history are applied to these nodes. Both linear and Drucker-Prager Models are used to describe the material. The vertical stress vs time is shown in Figures E3 and E4 and compared with the given radial stress time histories (i.e., "0" wave of Figure 4). Both models show good agreement up to the peak stress level. Neither model agrees after this time. Note: When integration order 3 was used, indefinite results were detected. Only integration order 2 could be used.

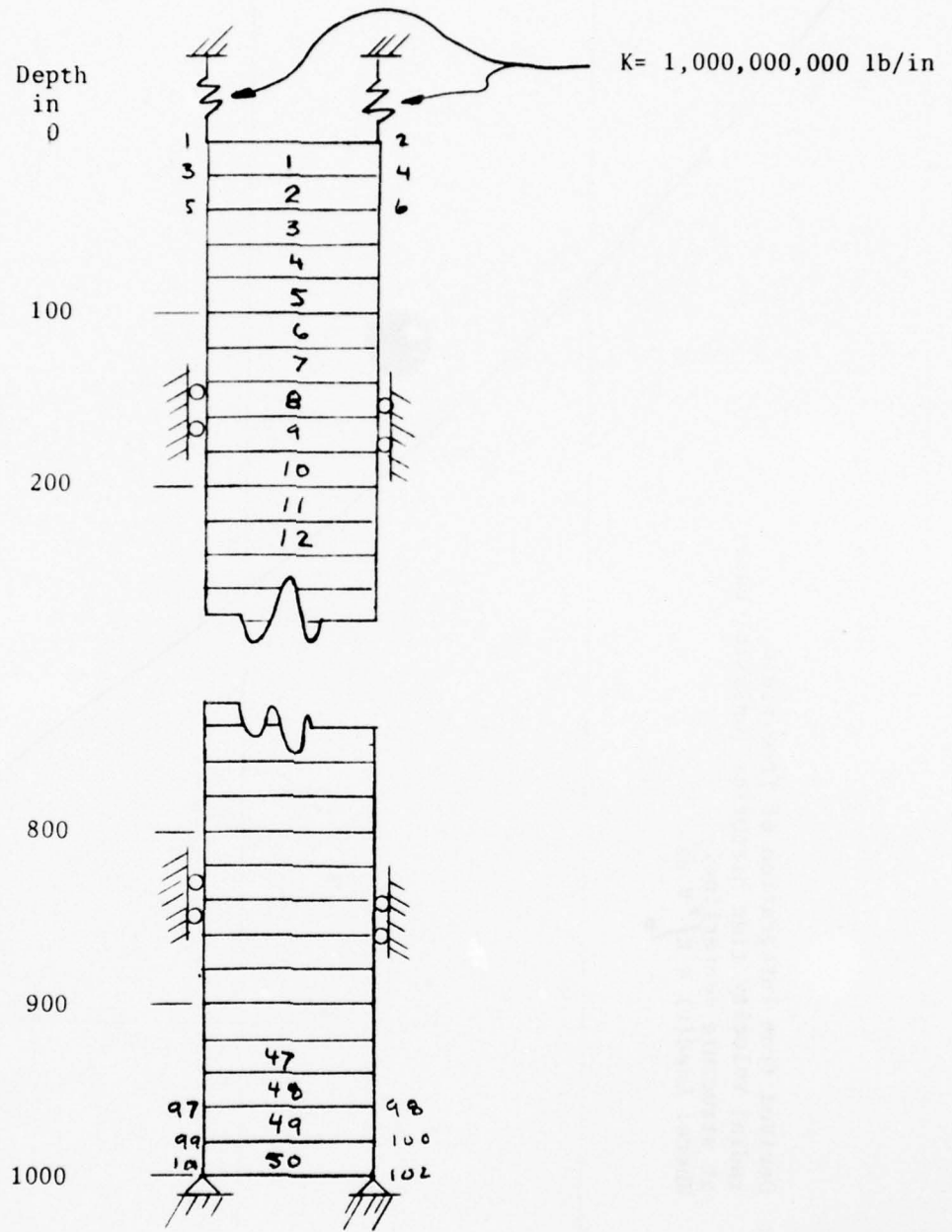
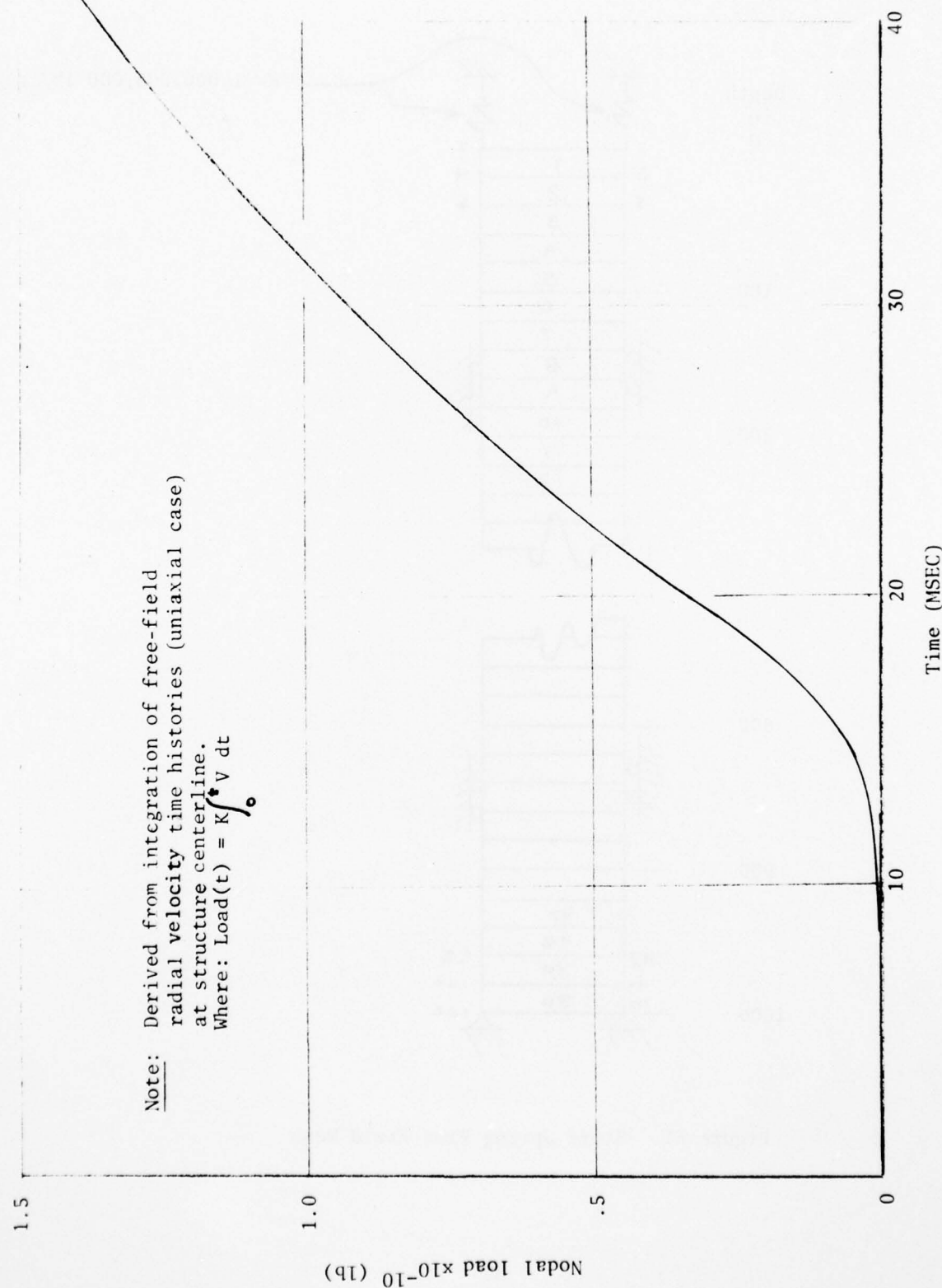


Figure E1. Stiff Spring Free Field Mesh



Note: Derived from integration of free-field radial velocity time histories (uniaxial case) at structure centerline.
 Where: $Load(t) = K \int_0^t V dt$

Figure E2. Nodal Load vs. time

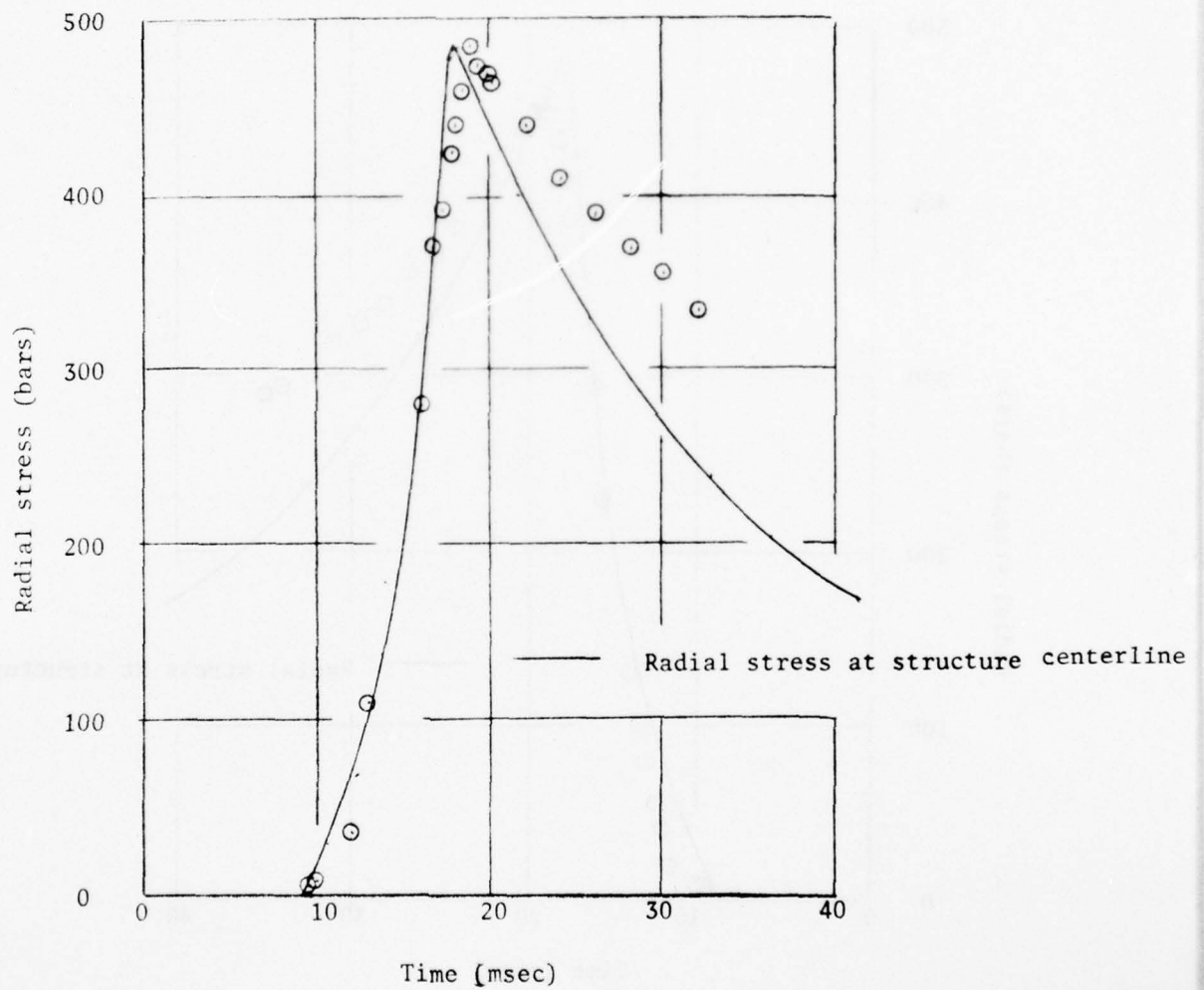


Figure E3. Radial (vertical) stress in Element 1; linear elastic Tuff

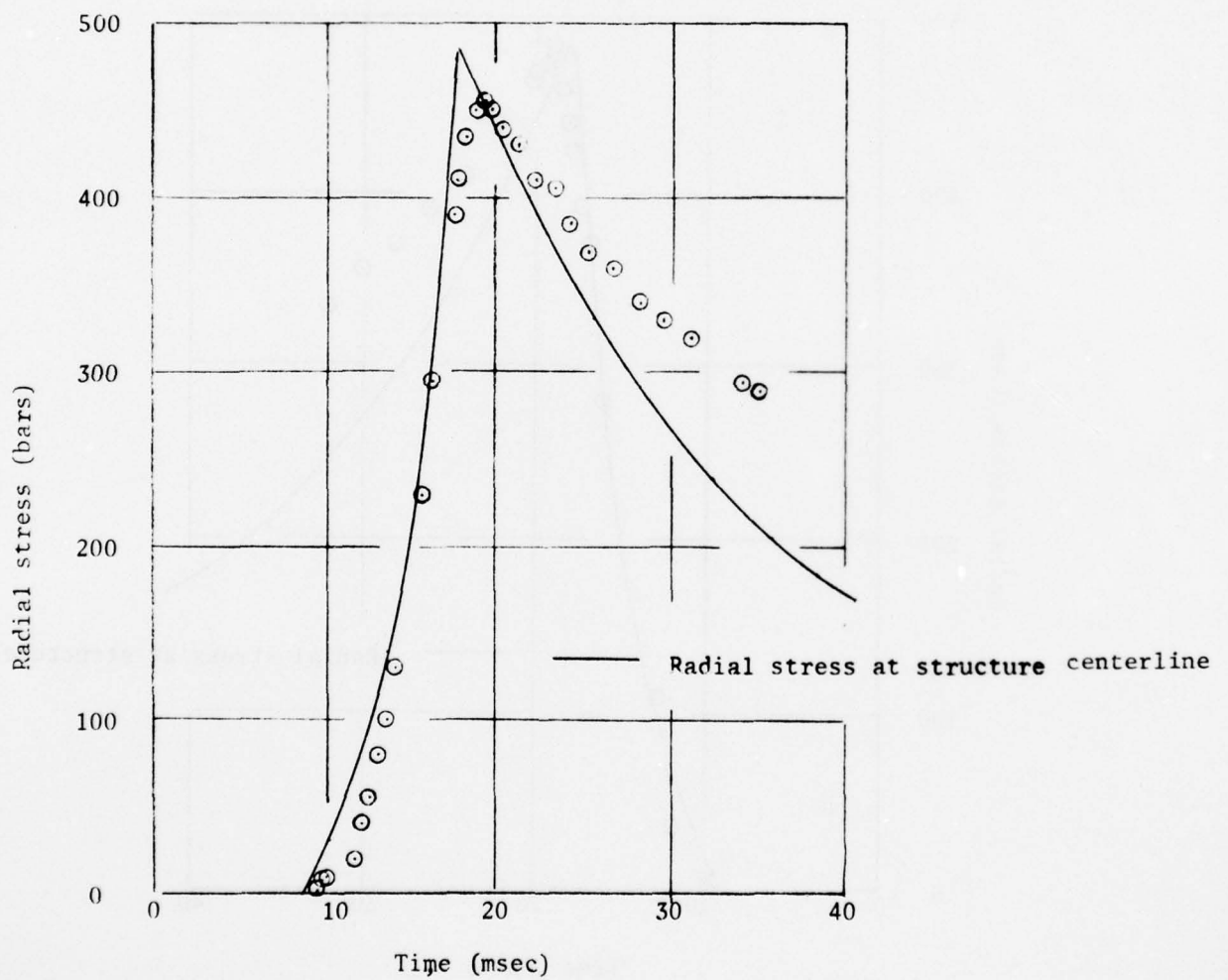


Figure E4. Radial (vertical) stress in Element 1; Drucker-Prager Tuff

REFERENCES

1. Bathe, K. J. and Peterson, F. E., User's Manual for CEL/NONSAP, a Nonlinear Structural Analysis Program, Contract Report, CR 75.004. Civil Engineering Laboratory, NCBC, Port Hueneme, CA 91043. October 1974.
2. Private communication from Ivan Sandler of Weidlinger Associates Consulting Engineers. November 14, 1975.
3. Private communication from Ivan Sandler of Weidlinger Associates Consulting Engineers. September 22, 1975.
4. Nelson, I., Baron, M. L., and Sandler, I., Mathematical Models for Geological Materials for Wave Propagation Studies, Shock Waves and the Mechanical Properties of Solids. Syracuse University Press, Syracuse, NY. 1971.
- A1. Private communication from Ivan Sandler of Weidlinger Associates, Consulting Engineers. August 8, 1975.
- A2. Butters, S. W., Stowe, R. L., LaComb, J. W., and Bendinelli, R. A., Characterization of Tuff and Development of Grouts for Mighty Epic Structures Program, TR76-21, Terra Tek, Salt Lake City, UT. April 1976.
- A3. Williamson, G. R., SP-44 ACI Publication Fiber Reinforced Concrete. The Effect of Steel Fibers on the Compressive Strength of Concrete.
- A4. Taylor, M. A., Tai, M. K., and Ramey, Melvin R., Proceedings of the ACI: Biaxial Compressive Behavior of Fiber Reinforced Mortar, No. 9, V. 72, September 1975.
- A5. Endebrock, E. G., and Traina, L. A., Static Concrete Constitutive Relations Based on Cubical Specimens. U. S. Air Force Weapons Lab Tech Report WL-TR-72-59, Vol 1, Vol 2. 1975.
- A6. Green, S. J. and Swanson, S. R., Static Constitutive Relations for Concrete. Air Force Weapons Lab Tech Report WL-TR-72-244. 1973.
- A7. Chinn, J. and Zimmerman, R., Behavior of Plain Concrete Under Various High Triaxial Compression Loading Conditions. U. S. Air Force Weapons Lab Tech Report WL-TR-64-163. 1965.
- B1. Biggs, J. M., Introduction to Structural Dynamics. New York. McGraw-Hill Book Company. 1964.
- B2. Hadala, P. F. and Taylor, H. M., Army Engineer Waterways Experiment Station, Technical Report S-72-2: Effect of grid size on cutoff frequency in the numerical solution of an elastic one-dimensional wave propagation problem. Vicksburg, Miss. February 1972.

B3. Agbabian-Jacobsen Associates. R-6820-1178: DEPS Code Modeling Techniques for Safeguard Structures. Los Angeles, CA. April 1970. (Contract DACA-69-C-0004).

B4. Bathe, K. J. and Peterson, F. E., Theoretical Basis for CEL/NONSAP. A Nonlinear Structural Analysis Program, Contract Report CR75.005. Civil Engineering Laboratory, NCBC, Port Hueneme, CA. October 1974.

LIST OF SYMBOLS

A	Cross-sectional area of finite element (in^2)
C	Wave speed (in/msec)
c	Cohesion (psi)
D	Depth of mesh (in)
D_B	Additional depth of mesh necessary to avoid reflection waves (in)
D_I	Depth of region of interest (in)
E	Young's modulus of Elasticity (psi)
E_T	Post-yield modulus of elasticity (psi)
e_{hL}	Volumetric hardening strain (%)
e_v	Volumetric strain (%)
f	Frequency (cps)
f'_C	Unconfined compressive strength (psi)
f_{\max}	Maximum frequency of mesh (cps)
G	Modulus of Elasticity in shear (psi)
G_L	Tangent shear modulus in loading (psi)
K	Bulk Modulus (psi)
K_L	Tangent Bulk Modulus in loading (psi)
K_O	At-rest coefficient of lateral earth pressure
K_U	Tangent Bulk Modulus in Unloading (psi)
k	Constrained spring constant (lb/in)
L	Length of finite element (in)
M	One-dimensional confined modulus (psi)
m	Lumped mass of finite element ($\text{lb-sec}^2/\text{in}$)

p	Hydrostatic pressure (psi)
p_H	Equivalent hydrostatic stress (psi)
p_O	External pressure (psi)
p_T	Equivalent confining stress (psi)
r	Radius to location in wall under consideration (in)
r_i	Internal radius (in)
r_o	External radius (in)
S_r	Wall stress in radial direction (psi)
S_t	Wall stress in tangential direction (psi)
T	Period (sec)
t_r	Rise time of stress wave (msec)
t^*	Time of peak stress (msec)
w	Weight density (pcf)
Δt	Time increment (msec)
δ_H	Horizontal nodal displacement (in)
δ_V	Vertical nodal displacement (in)
ϵ_a	Axial strain (%)
ϵ_r	Radial strain (%)
ϵ_y	Horizontal strain (μ in/in)
ϵ_z	Vertical strain (μ in/in)
ϵ_{zy}	Shear strain (μ in/in)
ν	Poisson's ratio
ρ	Mass density ($\text{lb-sec}^2/\text{in}^4$)
σ_Y	Horizontal stress (psi)
σ_Z	Vertical stress (psi)

σ_{ZY}	Shear stress (psi)
σ_a	Axial stress (Kbar)
σ_r	Radial stress (Kbar)
σ_v	Vertical one-dimensional stress (psi)
σ_y	Yield stress (psi)
σ_{yL}	Yield stress of cellular concrete (psi)
ϕ	Friction angle (degrees)

LIST OF TABLES

Table 1.	Material Properties
2.	Static Results for Mesh 3.0
3.	Static Results for Mesh 3.1
4.	Static Results for Mesh 3.2
5.	Static Results for Mesh 3.3
6.	Dynamic Results for Mesh 3.0
7.	Dynamic Results for Mesh 3.1
8.	Dynamic Results for Mesh 3.2
9.	Dynamic Results for Mesh 3.3
10.	Results for Homogeneous, Fiber Reinforced, Concrete Sphere (Mesh 4.0) - Static at Full Load; Dynamic at Peak
11.	Results for Composite Built-Up Liner (Mesh 5.0) - Static at Full Load; Dynamic at Peak
12.	Results for Composite Integral Liner (Mesh 6.0) - Static at Full Load; Dynamic at Peak
A1.	Curve Description Model for Cellular Concrete
C1.	Vertical Nodal Displacement at $t = 12$ ms
C2.	Vertical Stress at $t = 12$ ms
C3.	Vertical Stress and its Deviation Caused by Transition for Linear Tuff (Integration Order 2)
C4.	Vertical Stress and its Deviation Caused by Transition for Linear Tuff (Integration Order 3)

LIST OF FIGURES

- Figure 1. Homogeneous Sphere and Composite Built-Up Liner
- 2. Composite Integral Liner
- 3. General Character of Finite Element Meshes
- 4. Predicted Free Field Radial Stress Time Histories for Mighty Epic (uniaxial case, Ref. 3)
- 5. Predicted Free Field Velocity Time Histories for Mighty Epic (uniaxial case, Ref. 3)
- 6. Forcing functions used to generate the responses for the Mighty Epic Structures
- 7. Columnar mesh used to produce free field response
- 8. Free Field Response Stress vs Time (Element 24)
- 9. Free Field Response Velocity vs Time (at node 49)
- 10. Meshes used to check element compatibility
- 11. Meshes for Free Field with Cylindrical Cavity
- 12. Locations of Responses shown in Tables 2-12
- 13. Change in diameter history - Run DC5
- 14. Homogeneous Sphere Mesh (Mesh 4.0)
- 15. Composite Built-Up Liner (Mesh 5.0)
- 16. Composite Integral Liner (Mesh 6.0)
- 17. Change in diameter history; Mesh 4.0 - Run DHS2
- 18. Change in diameter history; Mesh 5.0 - Run DBL2
- 19. Change in diameter history; Mesh 6.0 - Run DIL2
- A1. Results of static one-dimensional compression test on Tuff
- A2. Results of static hydrostatic test on Tuff
- A3. Results of static triaxial tests on Tuff
- A4. Failure envelope for Tuff

AD-A047 427

CIVIL ENGINEERING LAB (NAVY) PORT HUENEME CALIF
MIGHTY EPIC PRE-TEST ANALYSIS.(U)
MAR 77 J CRAWFORD, R MURTHA, J ROLLINS
CEL-TM-51-77-5

F/G 18/3

UNCLASSIFIED

NL

2 OF 2
AD
A047427



END
DATE
FILMED
1 - 78
DDC

- Figure A5. Shear modulus vs confining stress
- A6. Cantilever beam meshes
 - A7. Hydrostatic test results
 - B1. Columnar Systems Used for Tuff Free Field Calculations
 - B2. Free Field Meshes
 - B3. Vertical stress vs time for Free Field Meshes
 - B4. Stress Wave Profile at 10 msec
 - C1. Location of Responses shown in Tables C1 and C2
 - D1. Columnar Mesh used for Progressively Increasing Δt
 - D2. Vertical stress history at 290-inch depth
 - E1. Stiff Spring Free Field Mesh
 - E2. Nodal Load vs Time
 - E3. Radial (vertical) stress in Element 1; linear elastic tuff
 - E4. Radial (vertical) stress in Element 1; Drucker-Prager Tuff